Experimental and Numerical Investigation Into the Impact of Aging, Flow, and Scaling on Discontinuous Fiber Composite and Hybrid Structures

Troy Nakagawa

A dissertation
submitted in partial fulfillment of the
requirements for the degree of

Doctor of Philosophy

University of Washington

2023

Reading Committee:

Marco Salviato, Chair

Jinkyu Yang

Eleftheria Roumeli

Program Authorized to Offer Degree:
William E. Boeing Department of Aeronautics and Astronautics

University of Washington

Abstract

Experimental and Numerical Investigation Into the Impact of Aging, Flow, and Scaling on Discontinuous Fiber Composite and Hybrid Structures

Troy Nakagawa

Chair of the Supervisory Committee:
Marco Salviato
Associate Professor

Discontinuous fiber composites (DFCs) have garnered the interest of many industries due to their manufacturing capabilities, and potential for recycling of thermoset prepregs. DFCs are manufactured by chopping conventional continuous fiber prepreg into platelets. This allows for ease of compression and injection molding, which is suitable for high volume production and cheaper manufacturing. Furthermore, these platelets do not need to be made using virgin material, and the trim from manufacturing, that would have ended up in a land fill, can be used to make DFCs. This further brings down cost of production when using this material. However, there are still some unanswered questions that need to be answered before there is widespread adoption of DFCs for recycling and other applications.

First of all, when using scrap thermoset prepreg, there will be ambient curing that may have effects on the performance of DFCs. Secondly, due to the random nature of the mesostructure, there is a need to find ways to control the variation between specimens. Thirdly, due to the complex geometries of DFC parts, there will always be regions of low and high flow that will cause a biased orientation of the platelets, thus there is a need to understand how this effects the mechanical behavior. Finally, there is a lack of computational tools that allow for the prediction of the behavior of DFCs. This leads to lengthy and costly physical testing to certify parts made with DFCs.

This study aims to address these aforementioned questions by experimentally and numerically investigating (1) mechanical and fracture properties of DFCs made using aged thermoset prepreg, (2) the effects platelet size, thickness, and adding continuous fiber plies to the outer surface of a DFC core has on flexure properties and its variation, (3) the effects that platelet flow conditions have on tensile properties, and (4) the behavior of a complex 3D part made using DFC. By building computational tools to predict experimental results, the design of DFC parts can be safer and more efficient.

TABLE OF CONTENTS

LIST OF FIGURES

LIST OF TABLES

ACKNOWLEDGMENTS

First, I would like to thank Professor Marco Salviato for his teaching and guidance towards my Ph.D. journey. Professor Salviato not only showed me how to study a field of mechanics but also how to think and tackle new problems in a scientific way. I deeply appreciate his kind dedication to my professional and personal growth to become a scientist and a researcher.

I also appreciate kind support from the doctoral committee members, Prof. Jinkyu Yang, Prof. Eli Livne, Prof. Dana Dabiri, and Prof. Eleftheria Roumeli. Also, many thanks to my colleagues and friends who shared the hardship of the graduate student life. Especially I thank all the MAMS members: Yao Qiao, Eunsik Phenisee, Toni Deleo, Genki Matsubara, Zhisong Chen, Jiacheng Chen, Collins Davis, Ryan Howe, Minh Nguyen, Kathryn Tidwell, James Davey, Shiva Kumar, Talal Abdullah, Yusuf Rasyid, Cory Slaughter, and many others. I thank all the DFC teams including the 55 undergraduates and 11 graduate students. Thank you for your hard work.

I would also like to thank many industry professionals. William Avery, Bill Kuykendall, Sean Yeung, Michelle Hickner, Dzung Tran, George Eliot, Sean Krewson, Ed Connery, Winnie Lin, Nancy-Lou Polk from the University of Washington, Chul Y Park, Ebonni Adams, Matthew Soja, Mike Larson, and Scott Gunther from the Boeing company, Dave Stanley, Ahmet Oztekin, Cindy Ashforth, and Larry Ilcewicz from the FAA, Scott James and Robb Medved from Sekisui Aerospace, Lisa Walton and Gary Bond from Solvay, Guy Houser, Mark O'Brien, and Erik Poulin from the Composite Recycling Technology Center.

Also, this study is financially supported by the FAA-funded Center of Excellence for Advanced Materials in Transport Aircraft Structures (AMTAS) and the Boeing Company. We

also wish to acknowledge the financial support provided by the Joint Center for Aerospace Technology Innovation (JCATI). I would also like to thank Sekisui Aerospace and the Composite Recycling Technology Center (CRTC) for their support with providing DFC specimen.

DEDICATION

to my family, Tracie Nakagawa, Jon Nakagawa, Jake Nakagawa, Dayle Pettus, James Pettus, and Allyson Pettus for their endless love and support.

Chapter 1

INTRODUCTION

The use of polymer composites in the aerospace, automotive, and energy sectors has seen a tremendous increase in the last few decades [1–3]. To give an idea, the U.S. composite end products market was valued at $26.7 billion in 2019 and is forecast to grow to $33.4 billion by 2025 [4,5]. Similar trends are reported worldwide. Traditional long fiber composites are suitable for large structures with simple contours such as wings, fuselages, and wind turbine blades [1,6]. However, it is difficult to manufacture complex shapes, such as brackets, due to the fibers folding and wrinkling [7, 8]. At the same time, sustainability becomes an increasing concern with the large growth of the composites industry, especially since the hard-to-recycle thermosetting composites represented 82% of the U.S. composite market in 2019 [4, 5]. Fostering sustainable practices and finding ways to reuse and recycle thermoset composite prepreg waste is imperative to mitigate the environmental impact of this industry and enable the expected growth of the market across the aerospace, automotive, and energy sectors. With these two issues in mind, Discontinuous Fiber Composites (DFCs) appears to be a promising material.

DFCs are made using platelets made from prepreg and can be randomly oriented or aligned. DFCs are also called as chopped fiber composites [9], randomly oriented strands (ROS) [10], stochastic prepreg platelet molded composite (PPMC) [11], ultra-thin chopped carbon fiber tape reinforced thermoplastic (UT-CTT) [12], and Sheet Molding Compound (SMC) [13]. A large advantage DFCs have over conventional composites is that complex parts can be manufactured to net shape or near net shape by utilizing compression or injection molding [14, 15]. This is due to the formability which comes from using platelets instead of long continuous fibers and leads to manufacturing of parts that need no addi-

tional machining and low material waste. In addition to this, parts made from DFCs have much faster manufacturing time, bringing down the time from hours to as little as 2 minutes [16–18]. Furthermore, DFCs can be used to repurpose scrap thermoset prepreg [19–22]. Thermosetting composites made up 82% of the U.S. market demand in 2019 with about 66% of waste generated from manufacturing being prepreg material [4, 5, 23]. These characters is why there has been an increased interest in researching this material and an increase use in the aerospace [14, 18, 24] and automotive industries [14–17, 25].

In addition to their manufacturability and potential for repurposing, DFCs have exhibited great mechanical performance when compared with other short fiber composites. This is due to the fact that unlike other short fiber composites, that have a fiber volume fraction of $25 - 40\%$ [26], DFCs have fiber volume fractions that are $50 - 60\%$ [12, 22]. This leads to DFCs having elastic properties that are similar to that of a continuous fiber quasi-isotropic laminate [22, 27, 28].

There has been many aspects of DFCs that have already been studied, e.g. platelet size and aspect ratio, matrix and fiber properties, manufacturing process, platelet and structure thicknesses, platelet orientation, out-time of the prepreg, and hybrid DFCs [10, 12, 19, 20, 28–38]. Feraboli et al. [28], and Selezneva and Lessard [10] investigated the mechanical properties of DFCs with varying platelet sizes and coupon thicknesses. They found that increasing the aspect ratio of platelets, increased mechanical properties but also increased variation. However, by increasing the coupon thickness, the variation decreased. The increase in coupon thickness also significantly reduced the plate warpage. Wan and Takahashi [12] investigated how tensile and compressive properties are effected by the platelet aspect ratio and molding pressures. They found that these two variable had little impact on the modulus, but the molding pressure had a significant effect on the strength. The strength of specimen made using a lower molding pressure, also resulted in a lower strength. Ko et al. [34,35] investigated the effects of platelet size with constant aspect ratio, and coupon thickness has on the fracture properties of DFCs. They found that, for a constant aspect ratio, larger platelets have a higher fracture energy. They also found that increasing thickness, increases the fracture

energy up to about 3 mm, and then the fracture energy plateaus. Li et al. [36] and Alves et al. [37] investigated the effects of platelet thickness on the tensile properties of DFCs. They found that thinner platelets had little impact on the tensile modulus, but higher strength. Kravchenko et al. [29, 30] and Sommer et al. [31] found that the mechanical properties of DFCs are highly dependent on the orientations of the platelets. They obtained the fiber orientation tensors through x-ray CT scans and used them to create finite element models. These models were able to capture the failure locations of the scanned coupons. Tang et al. [32] and Chen et al. [33] also found that fiber orientations and local material properties are highly correlated. They measured the fiber orientations using microscopy and found the local tensile modulus using digital image correlation. They saw that locations with poorly aligned fiber orientations and resin rich area also had lower modulus. Nilakantan et al. [19] investigated the effects prepreg aging had on DFCs, and hybrid laminates, with 50% platelets by weight sandwiched between continuous fibers. It was found that aging had no effect on the modulus, but there was an increase in strength. They also saw that the hybrid laminates exhibited a higher modulus and strength. Sultana et al. [20] focused on how the prepreg is aged (accelerated in an oven or naturally), and platelet size effect. They found that both types of aging had little effect on the modulus and the impact strength, but there was an increase in tensile strength. Corbridge et al. [38] investigated the flexure modulus and Interlaminar Shear Strength (ILSS) of DFCs and hybrid laminates, where three layers of unidirectional (UD) plies were added on top of two layers of DFC plies. They induced platelet flow by filling a third of the mold on two sides. This makes the platelets only flow to the center while keeping the applied pressure balanced. They found that the flexure modulus of DFCs was higher when the flow was aligned with the length of the specimen. This is also true for when the UD plies were along the direction of flow. When the UD plies were transverse to the flow direction, the modulus became similar of the 100% DFC laminate with flow along the length of the specimen. They also found that the ILSS was higher for the hybrid than the DFC laminates. Due to the flow of the platelets there was a lot of rotation and translations of the UD fibers. This was seen by placing a uniform grid on the UD ply before curing. They

saw that there were rotations as high as 30° and the original length of the grid was stretched and compressed by as much as $1.5 - 0.8$ times the original length. To mitigate this a precure routine was introduced, which kept the UD fibers straight, but decreased the ILSS.

There are still gaps in literature that needs to be answered for DFCs to become viable material for use for repurposing of thermoset prepreg and industrial applications. First of all, the work done on the aging of prepreg is limited to be mostly about tensile properties. In order to use DFCs for repurposing of prepreg a more thorough investigation into other mechanical properties and fracture properties is needed. Secondly, due to the random nature of the mesostructure, there is a need to find ways to control the variation between specimens. There has been work showing that platelet size and coupon thickness effects variation, however there is limited work on adding continuous fiber plies to control the variation. Thirdly, due to the complex geometries of DFC parts, there will always be regions of low and high flow that will cause a biased orientation of the platelets, thus there is a need to understand how this effects the mechanical behavior. Finally, there is a lack of computational tools that allow for the prediction of the behavior of DFCs. This leads to lengthy and costly physical testing to certify parts made with DFCs.

To address the aforementioned questions, this thesis presents experimental and numerical investigations to analyze and predict the mechanical fracture behaviors of discontinuous fiber composites. The following chapters explain the methods to accomplish the objective:

- Chapter 2 investigates the effect aging thermoset prepreg has on the mechanical and fracture properties of DFCs.

- Chapter 3 investigates the effects platelet size, specimen thickness, and adding continuous fiber plies to the outer surface of a DFC core has on the flexure properties.

- Chapter 4 investigates modeling of tensile behavior of DFC specimen with preferential orientation induced by high flow of platelets during cure.

- Chapter 5 investigates modeling of a real part made using DFC.

- Chapter 6 summarizes the findings and future works.

Chapter 2

EFFECTS OF AGING ON THE MECHANICAL AND FRACTURE PROPERTIES OF DISCONTINUOUS FIBER COMPOSITES MADE FROM REPURPOSED AEROSPACE PREPREG SCRAP AND WASTE

2.1 Introduction

The use of polymer composites in the aerospace, automotive, and energy sectors has seen a tremendous increase in the last few decades [1]. To give an idea, the U.S. composite end products market was valued at $26.7 billion in 2019 and is forecast to grow to $33.4 billion by 2025 [4, 5]. Similar trends are reported worldwide.

While these numbers give an idea of the key role that composites are playing in the global economic growth, they also show that sustainability is becoming an increasingly important issue considering that hard-to-recycle thermosetting composites represented 82% of the U.S. composite market in 2019 [4, 5]. Fostering sustainable practices and finding ways to reuse and recycle thermoset composite prepreg waste is imperative to mitigate the environmental impact of this industry and enable the expected growth of the market across the aerospace, automotive, and energy sectors.

Following [19], thermoset composite prepreg waste can be broadly classified into uncrosslinked waste produced during manufacturing and crosslinked waste from components reaching end of life. Efforts to handle the former material stream can be defined as "reuse" while efforts to handle the latter are commonly defined as "recycle". The overarching goal of recycling is to reclaim fibers from cured waste by getting rid of the matrix. Through the years, several interesting techniques for recycling have been developed including pyrolisis [39], matrix digestion [40], and depolymerization [41]. Typically, depending on the technique, re-

claimed fibers can have comparable mechanical properties to virgin fibers. However, this is often achieved at the expenses of fiber continuity. In fact, reclaimed fibers often take the form of tangled, discontinuous arrays which undermines the manufacturing of high-quality composite laminates requiring long, continuous fibers to achieve high mechanical performance [42–44]. Different from recycling, reusing aims at repurposing both the fibers and the uncured matrix in their original configuration to manufacture new composite parts [19]. In this case, the material sources include e.g. ply cutter waste, end-of-roll material, and out-of-spec material beyond out-life or storage life. For instance, the aerospace industry follows very strict requirements on material certification and the costs of re-certifying an out-of-spec material would be prohibitive, leading to significant amounts of prepreg waste. Except for few cases in which out-of-spec material is used internally for R&D or donated to research institutions, most prepreg scrap and waste ends in landfills, posing an environmental challenge. It is clear that this situation will not be sustainable with the future growth of the composite market unless prepreg waste reuse becomes common practice.

Figure 2.1: Typical products made by CRTC using repurposed aerospace carbon fiber composites: (a) carbon fiber bench, (b) portable pickle-ball net, (c) advanced laminated panels featuring natural wood and 85% in weight of recycled carbon fibers [9].

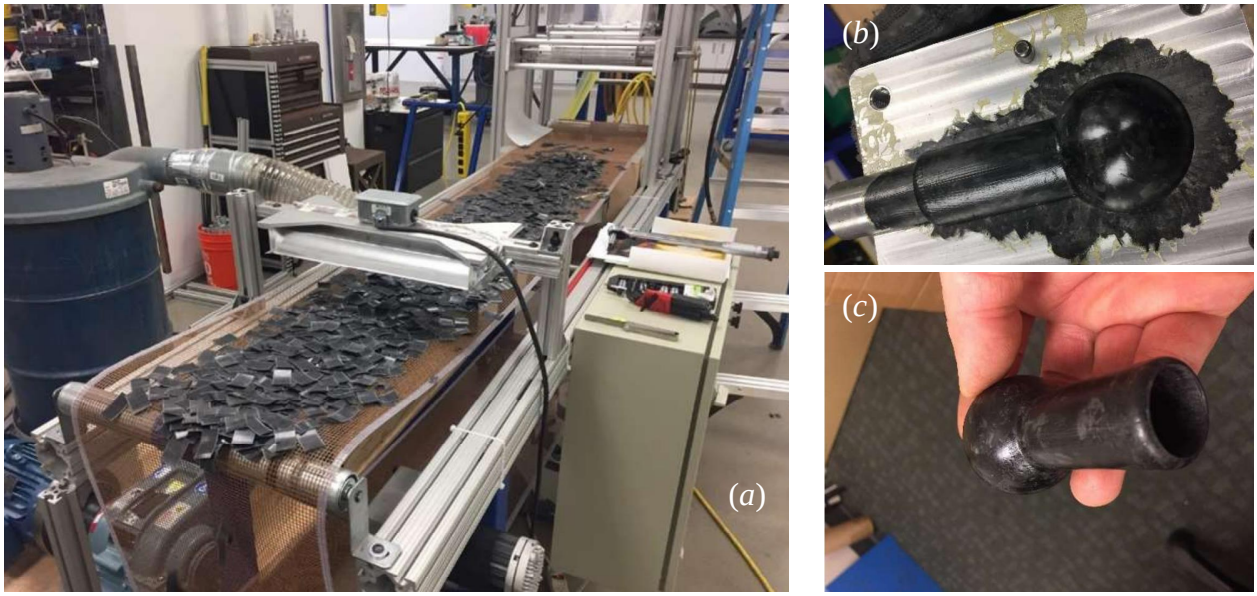

Figure 2.2: Discontinuous Fiber Composites made from repurposed aerospace carbon fiber prepregs: (a) platelets are cut from scrap prepregs to the desired shape and size, (b) compression molding is used to manufacture a ball joint, (c) the net-shape product is extracted. Thanks to this approach very complex shaped parts can be manufacturing without machining.

Developing technologies for the reuse of prepreg scrap and waste is one of the core missions of the Composite Recycling Technology Center (CRTC) [9] located in Port Angeles, WA, USA. Since its establishment the CRTC has developed unique products made from repurposed aerospace carbon fiber prepreg with applications ranging from the sport goods industry to construction and even defense. Figure 2.1a, for instance, shows a corrosion-resistant bench made using a combination of reused scrap roll form and Discontinuous Fiber Composites (DFCs). Figure 2.1b shows Swiftnet^{TM}, a lightweight, portable pickle-ball net while Figure 2.1c shows a novel Advanced Cross Laminated Timber Panel (ACLT) featuring natural wood and 85% in weight of repurposed aerospace carbon fibers.

Among the several technologies utilized by the CRTC, using prepreg scrap and waste to manufacture discontinuous fiber composites (also known as chopped fiber composites) is one that has shown great promise. As Figures 2.2a-c show, Discontinuous Fiber Composites

(DFCs) are made by cutting rectangular platelets from scrap prepregs. The platelets are used to fill a mold and can be compression molded to manufacture complex shaped parts. The platelet size and aspect ratio are the design parameters than can adapt to specific design requirements. Figures 2.2b,c show an example of a ball joint made by CRTC using repurposed prepreg. It is worth noting that, thanks to the unique characteristics of DFCs, even a complex part such as the one shown in the figure can be manufactured without additional machining. This characteristic alone might enable DFCs made from reused prepregs to reach markets that are not easily accessible by advanced unidirectional composites due to manufacturing costs. The use of DFCs to reuse prepreg also reduces the environmental impact of using carbon fiber composites. Bianchi et al. [45] performed a life cycle analysis of compression molded DFCs made from scrap prepreg and compared it to specimen made using virgin prepreg through compression molding and autoclave processes. They used Cumulative Energy Demand (CED), Global Warming Potential (GWP), and the ReCiPe method to evaluate the overall impact these three manufacturing processes have on energy consumption, greenhouse gas emissions, and the damage to human health, environmental diversity, and resource availability. They found that using scrap prepreg results in a lower environmental impact than the other processes. This showed that the use of DFCs to reuse scrap prepreg is a great sustainable practice, however more work needs to be done to verify that these parts made from scrap prepreg has good mechanical performance.

DFC parts made from virgin prepregs have already been shown to have outstanding mechanical properties, comparable to aluminum and quasi-isotropic carbon fiber laminates [34, 35]. However, it is possible that some of the properties of DFCs made from reused materials might be degraded by the aging of the prepregs. Hence, considering how difficult it would be to control the aging of this material stream, the question to answer is: how much does aging affect the mechanical performance of DFCs made from repurposed prepregs? There is very limited research that have been done on this topic [19–21, 46]. Nilakantan et al. [19] investigated the effects of aging on various manufacturing parameters (compaction pressure, temperature ramp rates, open/closed molds, etc.), platelets made of woven fibers

at $0°/90°$ and $\pm 45°$, and hybrid laminates with platelets and continuous fibers. They aged the prepreg until the out life of the prepreg (14 days) and investigated the aging effects in tension only. It was found that aging had no effect on the modulus, but there was an increase in strength. Sultana et al. [20,46] focused on how the prepreg is aged (accelerated in an oven or naturally), and platelet size effect. The aging done in this paper was naturally to $4\times$ the out life of the prepreg (out life 42 days, aged 6 months) or for 24 hours at 70°C in an oven, and then tensile properties and impact strength was found. They found that both types of aging had little effect on the modulus and the impact strength, but there was an increase in tensile strength. George et al. [21] aged their prepreg to $2-17\times$ the out life ($3-24$ months) naturally, or oven aged at 71°C for $24-72$ hours. Instead of comparing results of various out times, they compared the results by using glass transition temperatures of 25°C, 39°C, and 63°C. There was no unaged specimen so only the effects as aging progresses can be seen. In this paper, tension, flexure, and impact strength were investigated. Similarly to the other studies, there was no change in the modulus, however the increase in strength was much less significant than the ones found by Nilikantan et al. and Sultana et al.

The goal of the present study is to present one of the most comprehensive investigations into the effects of aging on mechanical and fracture properties. Tests were performed at three different out times and compared to unaged DFC and quasi-isotropic laminates. Tension, compression, and shear properties were obtained, and a size effect study is performed to obtain the global mode I fracture energy of DFCs made from reused material.

Understanding the link between aging and mechanical performance is quintessential to formulate design guidelines which can pave the way for the use of DFCs made from repurposed prepregs also in secondary structural applications.

2.2 Material preparation and test description

2.2.1 DFC manufacturing procedure

In this study, Toray T700G-12k/2510 prepreg was aged and used to manufacture DFC laminates. To follow the standard conditioning atmosphere stated in ASTM D4332 [47], an in-house environmental chamber was made to keep the temperature and humidity at $23 \pm 2°C$ and $50 \pm 5\%$RH respectively. An indoor grow tent was used to isolate the prepreg, and an off-the-shelf temperature and humidity controller was used to control a system composed of an Air Conditioner (AC), heater, humidifier, and dehumidifier. The prepreg was aged to $0\times$, $1\times$, $2\times$, and $3\times$ the out life of the prepreg (0, 28, 56, and 84 days). The manufacturing method detailed by Ko et al. [34, 48] was used to make the DFC laminates. Platelets were cut using a fabric cutter to the desired size of 50×8 mm. The weight was controlled to attain the desired thickness of 3.3 mm. In addition to the DFC specimens, a quasi-isotropic laminate using $[45/90/-45/0]_{3s}$ was made using unaged material to serve as an additional benchmark to evaluate the performance of the aged DFCs.

2.2.2 Analysis of crosslinking degree

To quantify the progression of cure while the prepreg ages, Differential Scanning Calorimetry (DSC) was used to obtain the enthalpy of the prepreg. These tests were done following ASTM D3418 [49] using a Mettler Toledo DSC 3+. For the first week of aging DSC tests were performed daily. After the first week, DSC was performed once a week for 28 days (which corresponds to one out life). Then, DSC was performed every other week until $3\times$ the out life was reached after which DSC testing was not performed until $7\times$ out life. After this, DSC was performed at $9\times$ the out life and at every $n\times$ out-lives until $16\times$ out-lives (448 days) was reached. This time is longer than any previous study found by the authors in the open literature.

For each DSC analysis, four samples of 10 mg were tested in aluminum pans. A ramp rate of 10°C/min was used to sweep from 23 to 280°C. Nitrogen was used as the purge gas and

had a flow rate of 10 mL/min. To calculate the enthalpy, a MATLAB code was developed to calculate the area under the specific heat flow vs time curve. During the later parts of the tests, glass transition temperature (T_g°) could also be calculated from these scans. To calculate the T_g° Mettler Toledo's STARe software was used which follows ASTM E1356 [50].

2.2.3 Mesostructure

An investigation into the mesostructure of aged DFCs was also performed. To this end, small sections of 25 mm were cut from the laminates. For out times 0× and 2×, 6 specimens were investigated, for out time 1×, 5 specimens were investigated, and for out time 3×, 4 specimens were investigated. The samples were encased into epoxy pucks made using Allied High Tech's QuickCure Acrylic to be used in a Struers RotoPol 21 and a RotoFoce 3 auto-polisher. Once polished, an Olympus BX50 microscope was used to inspect the mesostructure. A magnification of 5× was used to find the constituent content, thickness of platelets, and the number of platelets through the thickness. Stitching of the images was done using ImageJ which was also used to find the constituent content. To find the number of platelets though the thickness and the thickness of the platelets, 7 evenly spaced sections within the 25 mm length were investigated. The first and last sections were 1 mm away from the ends of the specimen. A MATLAB code was developed to find the thickness of platelets, and the number of platelets through the thickness [51].

2.2.4 Mechanical and fracture tests

2.2.4.1 Data acquisition

Tests were performed using an Instron 5585H 250 kN electro-mechanical load frame with an Interface 1210ACK-50kN-B load cell, and with the 250kN Instron load cell for the largest size tested for the size effect testing. The load cells recorded with a sampling frequency of 10 Hz while Digital Image Correlation (DIC) was used to obtain the strain values needed. Images were captured using a Nikon D5600 DSLR camera with Nikon AF micro 200 mm

and Sigma 135 mm DG HSM lenses with a sampling rate of 1 Hz. GOM Correlate [52] was used to process the photos and obtain the strain values. The number of specimens tested for each loading case can be found in Tables 2.3-2.6.

2.2.4.2 Tension

Tensile data for the quasi-isotropic and unaged DFCs made from the same material system tested in this work was taken from tests performed by Ko et al. [48]. For the aged samples, tensile tests were performed based on ASTM D3039 [53]. Specimens were made to have a width of 25.5 mm, which corresponds to about three times the width of a platelet, and a gauge length of 140 mm. The tabs were made with 3.175 mm (1/8 in.) thick garolite and JB-Weld Cold Weld Steel Reinforced Epoxy and had a length of 55 mm with a bevel of 8°. A displacement rate of 2 mm/min was maintained for all the tests.

2.2.4.3 Compression

Compression tests were performed following ASTM D3410 [54]. The samples were made to have a width of 12.5 mm, a gauge length of 25 mm and 50 mm tabs. All compression tests were performed using the Instron load frame and a Wyoming Modified IITRI Compression test fixture. A displacement rate of 1.5 mm/min was used.

2.2.4.4 Shear

Shear tests were performed according to ASTM D5379 [55]. An Omax 2652 water jet cutter was used to cut the specimens to the required geometry. Specimens were tabbed using 1/8 in thick garolite and Solvay FM 94k adhesive film. During the tests, the specimens were clamped in the tab area to prevent crushing and twisting and tested using the Instron load frame and a Wyoming Iosipescu test fixture. A displacement rate of 1 mm/min was used.

For the calculation of the shear strains during the tests, a thorough investigation was performed to identify the area of analysis providing the most consistent and accurate results.

Figures 2.3a,b show the effect of the size of the area used for the calculation of the shear modulus. It can be seen in fig. 2.3a that the shear modulus does not change much when the box width is less than 1 mm. But, after this point the modulus starts to increase rapidly. At 1 mm, the percent increase of the shear modulus calculated is only 0.68%. The increase after 1 mm is from the fact that only the center of the specimen is in pure shear. When looking at a DFC specimen, fig. 2.3b, a similar trend can be seen. At 1 mm the percent increase in modulus is only 0.87%. Even though the area of pure shear will be the same for the DFC and quasi-isotropic specimen, the modulus change within that width will look different for DFC specimens, since DFCs' mesostructure is inhomogeneous. This is confirmed by the fact that the shear modulus increase within the 1 mm box is different when compared to the quasi-isotropic layup. Another observation showing the inhomogeneous mesostructure of DFCs' is that, when the box width is between about $4 - 5$ mm, the modulus decreases which does not happen for the quasi-isotropic specimen. From the quasi-isotropic layup the shear strain does not change within the 1 mm area at the center, thus it can be assumed that this area is in pure shear and is a good area to average shear strain over for all the specimens. This size was used for the analysis of all the shear specimens investigated in this work.

2.2.4.5 Size effect tests

For the aged coupons, the experimental procedures used in this study followed [34]. This source also provided size effect test data for quasi-isotropic and unaged DFCs. The smallest size effect specimen had a base dimension of 20×44.5 mm ($D \times L_g$) and a target thickness of 3.3 mm. The gauge areas of the specimens were geometrically scaled following a 2D scaling of $1 : 2 : 4$. Tabs were made with 3.175 mm (1/8 in.) thick garolite and JB-Weld Cold Weld Steel Reinforced Epoxy with a length of 38 mm for all specimens. To create the notch, a diamond-coated razor blade saw was used. The blade thickness was 0.2 mm. The initial notch length, $a_\circ$, was kept at a constant ratio of $D/5$. A constant strain rate of 0.2%/min was used for all specimens.

Following e.g. [34, 35, 56], the nominal strengths of the specimens were defined as $\sigma_{Nc} =$

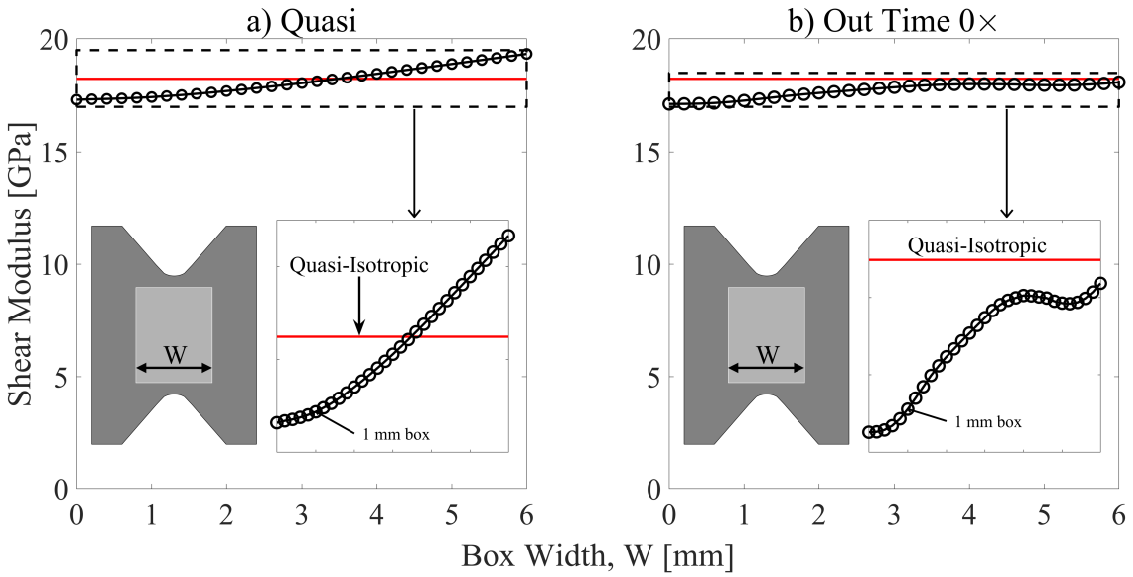

Figure 2.3: Change of calculated shear modulus when changing the the width of the box where the shear strain from DIC analysis is averaged. The box has a height such that it is 1 mm from the notch. The red line is the average shear modulus of the quasi-isotropic specimens.

P_c/tD, where P_c is the peak load found during tests, t is the specimen thickness, and D is the specimen width. The displacements used were found using Digital Image Correlation (DIC) in order to remove the effects of the compliance of the machine. The nominal displacement was calculated by averaging the relative displacement between two horizontal lines spanning the width of the specimen. The distance between the lines and the notch was taken to be $1.2D$.

2.3 Size effect analysis

In this study, Type 2 size effect of aged DFCs is investigated. Type 2 size effect deals with structures featuring a stress-free crack or notch [57, 58]. Due to the complex mesostructure of DFCs, significant stress redistribution occurs during the damage process [34, 35]. This redistribution is characterized by a non-linear Fracture Process Zone (FPZ) whose size is proportional to the size of the largest inhomogeneity of the material. For increasing structure

sizes, the percentage of the structure subject to the stress redistribution occurring in the FPZ gets smaller and smaller, leading to significant size effects. Typically, large quasibrittle structures experience limited stress redistribution prior to failure and they behave in a rather brittle manner. In contrast, small structures compared to the characteristic size of the FPZ incur significant non-linear stress redistribution which reduce the severity of the notch and generally lead to a more quasiductile behavior. These size effects have been confirmed for a number of quasibrittle materials including e.g. fiber and 2D/3D textile composites [56,59–61], polymers [62], nanocomposites [63,64], concrete [65,66], metals [67], and many other materials [57].

Equivalent fracture mechanics, which was pioneered by Irwin [68] and extended to quasibrittle materials [69], can be used to account for these effects provided that the FPZ is still not too large compared to the structure size. Towards this goal, an additional effective FPZ length, c_f, is added to the original crack length, a_0. The additional length is added such that the resultant stress of the effective crack equals the ones related to the cohesive stresses in the FPZ.

The effective FPZ size, c_f, depends on how the elastic energy in the FPZ is being dissipated. In DFCs, some mechanisms for energy dissipation are fiber fracture, platelet pullout, platelet delamination, and matrix microcracking [34,35]. These mechanisms are all influenced by the platelet geometry, orientation, and the number of platelets through the thickness. Thus, the mesostructure must be properly accounted for to capture the fracture behavior and the effects of the non-linear FPZ.

If the mesostructure and quasibrittle softening laws are calibrated properly, the progressive damage in a structure can be modeled explicitly and the c_f can be predicted. However, with equivalent fracture mechanics, c_f can be found experimentally through size effect analysis. Doing so means the progressive damage does not need to be modeled explicitly, but the effects of the mesostructure still needs to be captured. Through finite element modeling, the effects of the mesostructure on the elastic strain energy can be captured. By combining the size effect experiments and finite element modeling the fracture behavior of DFCs

can be characterized. The following sections provide an explanation of the analytical and computational framework used.

2.3.1 Size Effect Law (SEL)

As stated previously, to account for the non-linear Fracture Process Zone (FPZ), an equivalent crack length is used:

$$a = a_0 + c_f \tag{2.1}$$

where a_0 is the original crack length, and c_f is the effective FPZ length, which is treated as a material property.

From Linear Elastic Fracture Mechanics (LEFM), the energy release rate as a function of the dimensionless crack length is:

$$G(\alpha) = \frac{\sigma_N^2 D}{E^*} g(\alpha) \tag{2.2}$$

with $\alpha = a/D$ being the dimensionless crack length, $\sigma_N = P/(tD)$ being the nominal stress, E^* being the effective elastic tensile modulus, and $g(\alpha)$ being the dimensionless energy release rate. The dimensionless energy release rate accounts for the effects of geometry on the energy release rate. For structures that are homogeneous, g depends only on the geometry of the structure and is constant for geometrically-scaled specimens. However, DFC inhomogeneities, which depend on the platelet's geometry and are not geometrically scaled, can be comparable with the size of the structures. Thus different structure sizes may lead to significantly different energy release rates potentially making g dependent on the structure size, D, and the thickness, t. We can write eq. 2.2 to account for the inhomogeneity of DFCs as follows:

$$G(\alpha, D) = \frac{\sigma_N^2 D}{E^*} g(\alpha, D) \tag{2.3}$$

where g is now considered a function of both the dimensionless crack length and the characteristic length of the structure.

At the onset of fracture, the energy release rate, G, must be equal to the fracture energy, G_f, assumed to be a material property. By substituting eq. 2.1 into eq. 2.2, G_f can be

expressed in terms of the effective crack length:

$$G_f = G(\alpha_0 + c_f/D, D) = \frac{\sigma_N^2 D}{E^*} g(\alpha_0 + c_f/D, D) \tag{2.4}$$

Performing a Taylor expansion around α_0 for a constant D we get:

$$G_f = \frac{\sigma_N^2 D}{E^*} \left[g(\alpha_0, D) + \frac{c_f}{D} \frac{\partial g}{\partial \alpha}(\alpha_0, D) \right] \tag{2.5}$$

By rearranging eq. 2.5, Bažant's Size Effect Law (SEL) is obtained [70]:

$$\sigma_{Nc} = \sqrt{\frac{E^* G_f}{D g(\alpha_0, D) + c_f g'_D(\alpha_0, D)}} \tag{2.6}$$

where, $g'_D = [\partial g/\partial \alpha]_D$. Here, the subscript D denotes that the partial differentiation is taken for a constant structure size. It should be noted that, in contrast to the traditional SEL [70], the dimensionless energy release rate in eq. 2.6 is a function of the structure size and can be calculated via stochastic finite element analysis. Unlike LEFM, eq. 2.6 depends both on the structure size and the material characteristic length. This is needed to capture the transition of the fracture behavior from quasi-ductile to brittle. It is worth noting that Eq. 2.6 can also be written as follows:

$$\sigma_{Nc} = \frac{\sigma_0}{\sqrt{1 + D/D_0}} \tag{2.7}$$

where, $\sigma_0 = \sqrt{E^* G_f / c_f g'_D(\alpha_0, D)}$ and $D_0 = c_f g'_D(\alpha_0, D)/g(\alpha_0, D)$ are the size effect constants depending on the structure geometry and FPZ size.

2.3.2 Fitting of the experimental data using SEL

To obtain the size effect constants from experiments, linear regression analysis was performed as shown in fig. 2.8. In fact, Eq. 2.7 can be written in a linear form [57, 69]:

$$Y = C + AX \tag{2.8}$$

using the following transformation:

$$X = D, \quad Y = \sigma_{Nc}^{-2}, \quad \sigma_0 = C^{-1/2}, \quad D_0 = \frac{C}{A} \tag{2.9}$$

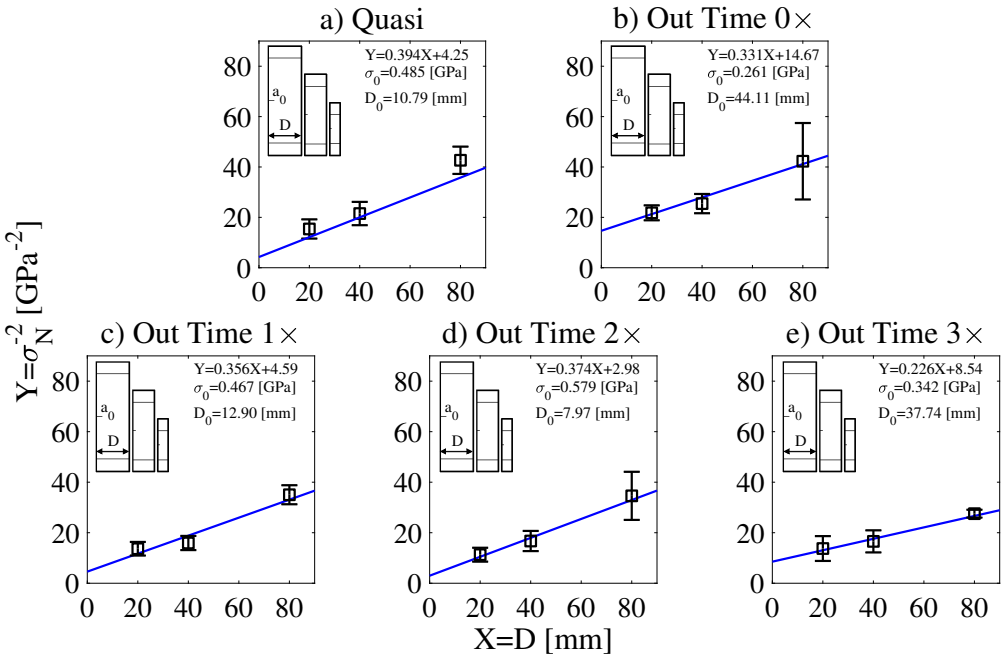

Figure 2.4: Linear regression analysis to find the size effect constants, σ_0 and $D_\circ$, for quasi-isotropic, unaged DFC, and aged DFC specimen. Quasi-isotropic and unaged DFC results are taken from Ko et al. [34]

As can be noted from fig. 2.4 and eq. 2.9, the size effect constants are obtained from the slope and the y-intercept providing the input for the construction of the size effect curves using eq. 2.7.

2.3.3 Stochastic finite element model

In order to obtain the fracture energy, G_f, and the FPZ length, c_f, the dimensionless energy release rate, $g(\alpha_0, D)$, and its derivative, $g'_D(\alpha_0, D)$, must be found. These values are highly dependent on the platelet constitutive properties and the random distribution of the platelets. To capture this, a stochastic finite element model is used.

2.3.3.1 Mesostructure generation

The mesostructure generation used in this work is an extension of the stochastic laminate analogy method proposed in [71–73]. A brief summary of the generation algorithm is provided

here, and more details on the algorithm and its implementation can be found in [34,35,74,75]. In this study platelets are partitioned into grids of 1×1 mm.

The platelet generation algorithm can be divided into two parts. The first is a platelet distribution algorithm and the second is a thickness adjustment algorithm. In this study, the platelets are assumed to be perfectly randomly distributed and planar. This means that a uniform probability distribution is used for both the spacial component and orientation of the platelet, and the out-of-plane orientation is assumed to be zero. From the mesostructure investigation we have the average number of platelets through the thickness and the CoV of the laminates for the different out times which are used as inputs to the platelet generation algorithm. To achieve these parameters, saturation points and platelet limits are used to guide generation. Saturation points are set to be every three layers. The average number of platelets through the thickness must equal the current saturation point before moving on to the next saturation point. The platelet limits are used to prevent a higher concentration of platelets in certain areas. A higher concentration would lead to the average number of platelets to equal the saturation point, but there would be large areas of little to no platelets. These limits are taken to be the saturation points times the CoV.

Once the average number of platelets generated meets the one found from the mesostructure study, a thickness adjustment is performed. This is done to simulate the effects of resin flow, without modeling it explicitly. If the number of platelets through the thickness is greater than or equal to the average number of platelets found experimentally, then the thickness of the platelet will be evenly distributed to all the platelets. If the number of platelets though the thickness is less than the one found experimentally, then resin will fill the additional thickness needed. This is done to mimic resin flow. For more information about the platelet generation algorithm the reader is referred to previous articles published by the authors [34, 35, 74, 75].

2.3.3.2 Computation of g(α) and g'(α)

The mesostructure that is generated from section 2.3.3.1 is imported into Abaqus/Standard [76]. Each partition in the mesostructure is homogenised into an 8-node, quadrilateral Belytschko-Tsay shell element (S8R). The platelets and resin are assumed to be linear elastic, with properties shown in table 2.1. At one end a uniform uni-axial displacement is applied and the other end is fixed in all directions. For homogeneous geometrically scaled specimens, $g(\alpha)$ and $g'(\alpha)$ do not change with the structure size [69]. However, this is not generally true for DFCs since they have an inhomogeneous mesostructure. For this reason, $5-8$ specimens for every size and out time are simulated to verify if any size effects on $g(\alpha)$ and $g'(\alpha)$ are present.

Table 2.1: Elastic properties of platelets and resin used in the stochastic finite element model.

Description	T700G	Resin
Platelet thickness, t [mm]	varies	varies
In-plane longitudinal modulus, E_1 [GPa]	135	3
In-plane transverse modulus, E_2 [GPa]	10	3
In-plane shear modulus, G_{12} [GPa]	5	1.1
In-plane Poisson ratio, ν_{12}, ν_{31}	0.3	0.35

Generally, a method to obtain the energy release rate is by using the J-integral [56, 77]. This can not be done with DFCs because of their inhomogeneous mesostructure. To calculate $G(\alpha)$, its definition is used [69]:

$$G(u,a) = -\frac{1}{b}\left[\frac{\partial \Pi(u,a)}{\partial a}\right]_u \tag{2.10}$$

with u being the applied displacement, a being the crack length, b the thickness, and Π being the potential energy of the whole specimen. The subscript u denotes that the potential energy is taken for a constant applied displacement. Figure 2.5a shows the potential energy of

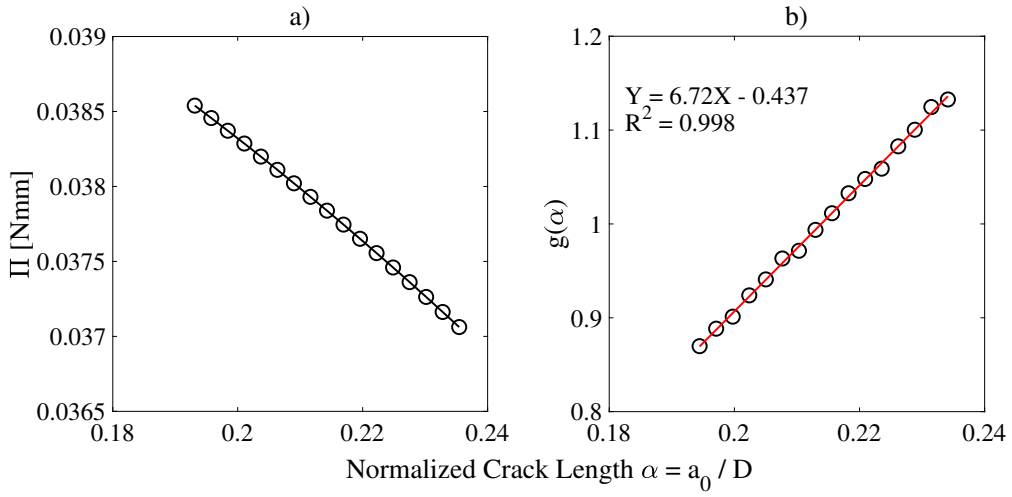

Figure 2.5: a) Strain energy as a function of the normalized crack length obtained from a typical SENT simulation. b) The calculated dimensionless energy release rate $g(\alpha_0)$ and its derivative $g'(\alpha_0)$.

a typical DFC SENT specimen. To approximate $G(u, a)$ the central finite difference method is used to get the partial derivative of the potential energy as a function of the normalized crack length $\alpha = a/D$. Then, the dimensionless energy release rate, $g(\alpha)$, is found using eq. 2.2 and $g'(\alpha)$ can be found through linear regression as can be seen in fig. 2.5.

Figure 2.6 show the dimensionless energy release rate and its derivative at various out times for various sizes. It can be seen that g and g' do not change significantly with age or with structure size. This result agrees with previous work done by Ko et al. [34,35,48] which showed that, when the average number of platelets through the thickness of the structure is sufficiently large, the mesostructure becomes statistically homogeneous and the energy release rate has no dependence on structure size. Therefore, the dimensionless energy release rates were considered to be size independent in this work and the average g and g' values of all specimen sizes for a given out time were used. However, it should be noted that for another platelet geometry or specimen thickness, g and g' may become dependent on the structure size and the dimensionless functions calculated for each size should be used instead of the averaged values.

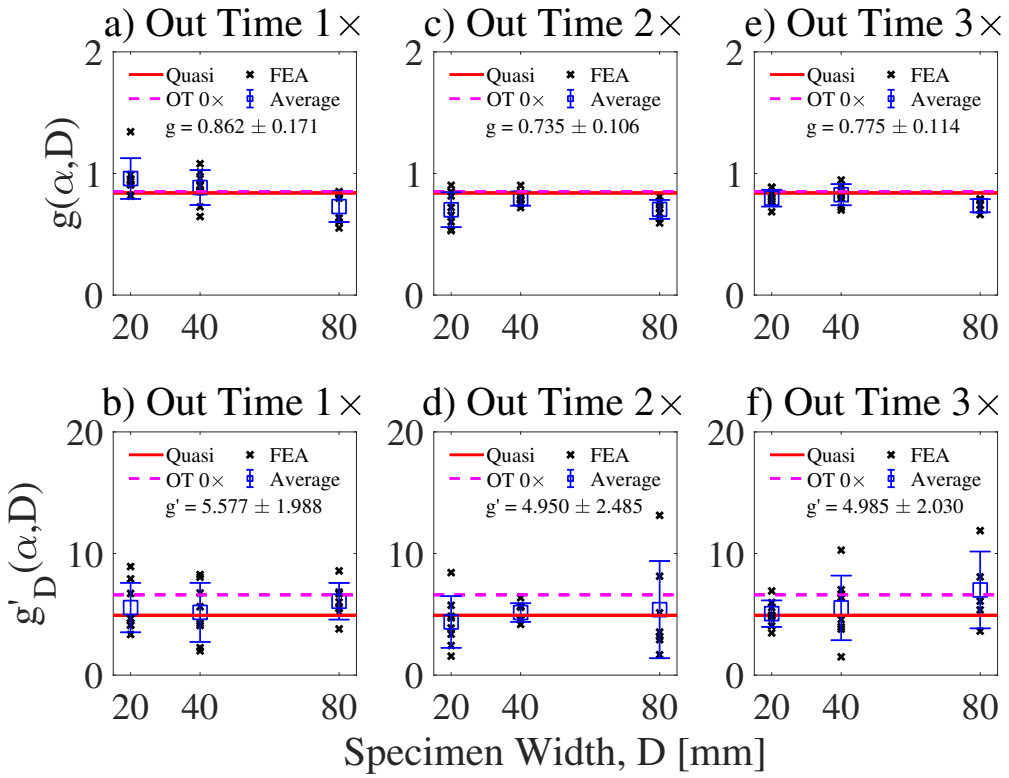

Figure 2.6: Comparison of dimensionless energy release rate and its derivative for the out times of a) and b) 1 × (28 days), c) and d) 2 × (56 days), and e) and f) 3 × (84 days). Quasi-isotropic and unaged DFC results are obtained from Ko et al. [34].

2.4 Results and discussion

2.4.1 Crosslinking evolution with aging

In fig. 2.7a and b, the results from the enthalpy calculations are shown. It can be seen in fig. 2.7b, that at the beginning there is an increase in enthalpy from day 0 to day 4. This is because the initial samples were taken from the edge of the prepreg roll and each day was a little closer to the center of the roll. Starting from day 4 the samples for DSC analysis were taken from the center of the roll. For this reason, when calculating the percent decrease of enthalpy in fig. 2.8 and when performing the linear fit, the initial enthalpy is taken to be the one calculated on day 4.

The data in fig. 2.7 and 2.8 were fit using the following exponential fitting equation:

$$\Psi = A\left[1 + B\exp\left(-\frac{t}{H}\right)\right] \tag{2.11}$$

where A is the horizontal asymptote, the initial slope is $-AB/H$, and the y-intercept is $A(1+B)$. At the early stages of aging the decrease in enthalpy is approximately linear. Then the enthalpy starts to asymptotically approach a value of 84 J/g, indicating a saturation of crosslinking. It can be seen in the figures, that more crosslinking can occur, but the time required to complete the curing would be extremely large. The final enthalpy measured has about a 7% difference from the asymptote, and to get to a difference of 1%, an additional 358 days of aging is needed. This would correspond to the percent enthalpy decrease to go from 49.4% to 52.6%. At this point the evolution of crosslinking is marginal. A similar saturation can also be seen in the glass transition temperature (T_g) in fig. 2.9. From 10× the out life (280 days) the T_g can be seen in the heat flow curves. The T_g appears to be saturating at about 63°C. This shows that if the prepreg is left out past this time there should be no further progression of ambient curing. It should be noted that the exact degree of cure cannot be obtained because of the unknown initial enthalpy or degree of cure of the epoxy. Thus the percent decrease stated here is related to a progression of cure since the "as purchased" state rather than the degree of cure of the prepreg.

The initial linear decrease of enthalpy with age reported in this work has been shown in many previous studies [78–83]. However, the horizontal asymptote for long age times as the one shown in fig. 2.7 has only been reported in the study done by Blass et al. [78]. One of the two prepregs tested by Blass et al. showed this plateau at 4× the out life, while the other did not reach this plateau even after 12× the out life. Both of these prepregs were aged to 120 days which is less than half the aging times investigated in the present work. The tests performed in this work clearly show a saturation of crosslinking occurring at ambient temperature for sufficient out times. In the context of repurposing the material to make chopped fiber composites, this observation is of utmost importance. In fact, tracking the out time of various material streams might not be practical or even possible. However, the results

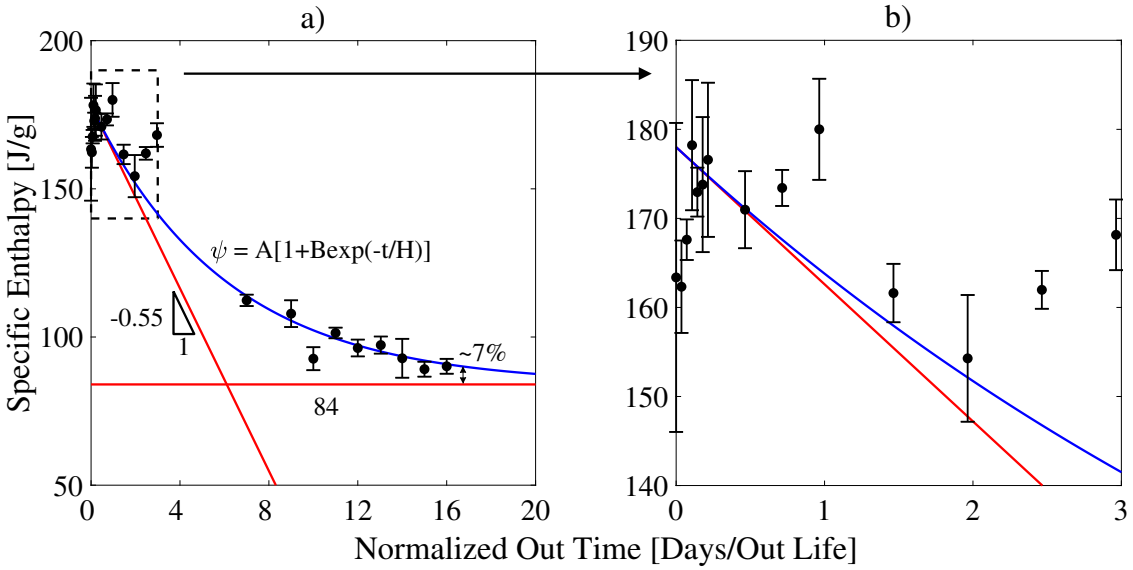

Figure 2.7: Results from DSC analysis. a) Enthalpy vs the normalized out time, and b) a zoomed in view of the enthalpy vs normalized out time plot showing the out time window the mechanical testing was performed.

clearly suggest that while crosslinking occurs continuously during the aging of the material, it would take a significant amount of time to reach a state in which further curing is not possible. Simple DSC sampling of the repurposed material every e.g. $4-5$ out times might be enough to make sure the material can still be used. Of course, the extensive usability over large aging times makes the use of scrap prepregs from other composite manufacturing processes very attractive and convenient provided that the mechanical properties are not significantly affected by aging.

2.4.2 Mesostructure

Figure 2.10 and table 2.2 show the laminate thickness measured from all the tested specimens, and the number of platelets through the thickness found through microscopy. It can be seen that there was an increase in the specimen thickness with out time. The increase from the unaged to the aged specimen was between 23% and 33% while there was much less change in thickness between the aged specimens. It can be noted that the number of platelets through

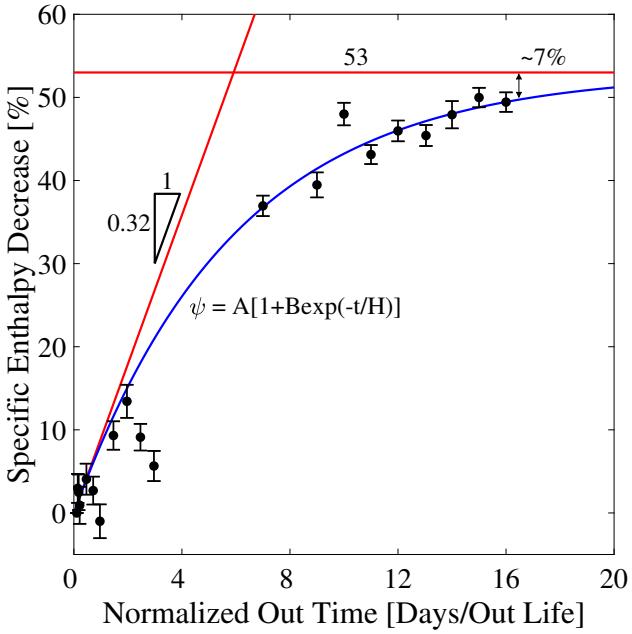

Figure 2.8: Percent decrease of enthalpy vs the normalized out time, detailing the progression of curing compared to the "as purchased" enthalpy.

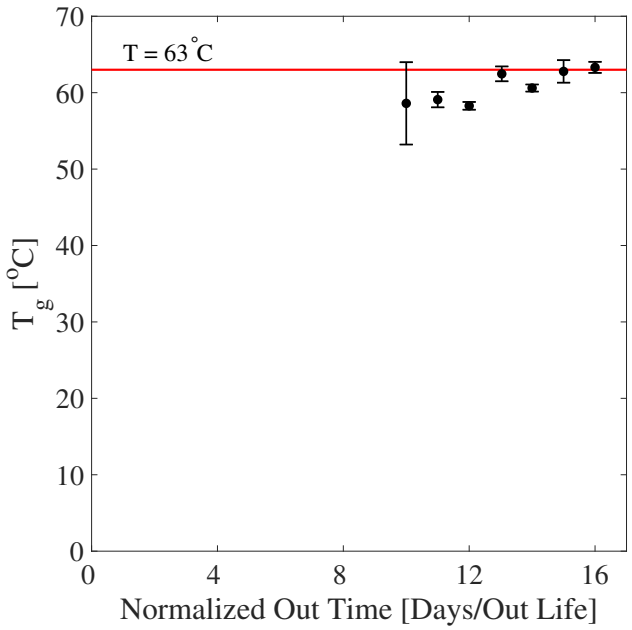

Figure 2.9: Glass transition temperature (T_g) for out times 10-16x (280-448 days).

Table 2.2: Summary of the mesostructure analysis performed

	Quasi	Out Time 0×	Out Time 1×	Out Time 2×	Out Time 3×
Laminate Thickness [mm]	3.53 ± 0.05	3.01 ± 0.04	3.70 ± 0.06	3.99 ± 0.14	3.87 ± 0.10
Platelet Thickness [mm]	0.145 ± 0.01	0.137 ± 0.05	0.133 ± 0.04	0.132 ± 0.04	0.131 ± 0.04
Number of Platelets	24 ± 0	20.74 ± 4.47	24.06 ± 7.26	27.67 ± 7.85	28.36 ± 4.88
Fiber Area Fraction [%]	58.19 ± 0.90	59.19 ± 7.73	60.21 ± 7.77	57.43 ± 10.10	61.48 ± 6.61
Void Area Fraction [%]	0.29 ± 0.23	0.24 ± 0.18	0.98 ± 1.24	0.90 ± 1.17	1.10 ± 1.34

the thickness increased with the out time. This can be explained by looking at the thickness of the platelets reported in Figure 2.11 and table 2.2. In fact, it can be noted that the platelets in the DFC specimens are slightly thinner than those of the plies in the quasi-isotropic laminate. However, the platelet thickness does not change with the increase in out time. Figure 2.11 shows the probability density of the platelet thicknesses constructed leveraging $800 - 1160$ platelet observations for each out time. As can be noted, there are only slight changes in the peaks of the probability distributions with a change in out time, confirming that the mesostructure does not change significantly with increasing out time.

Figure 2.12 shows areas where the platelet thickness is significantly different from the average value due to defects. Fig. 2.12a, for instance, shows fibers rearranging around a void causing an increase in thickness of the platelet. On the other hand, fig. 2.12b shows an area where there are fewer platelets compared to the average number of platelets and the remaining volume must be filled with resin or voids. Due to the resin filling the volume where there are no platelets, the thickness of the platelet that is in the volume increases.

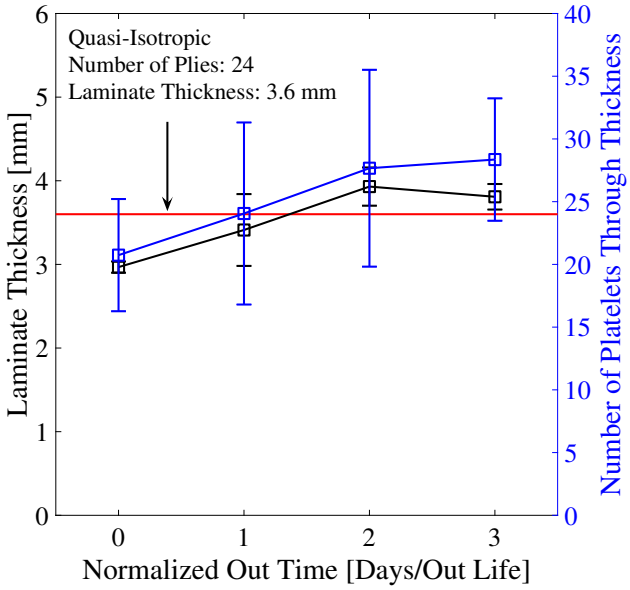

Figure 2.10: Number of platelets through the thickness and laminate thickness of unaged quasi-isotropic and DFC laminates at various out times.

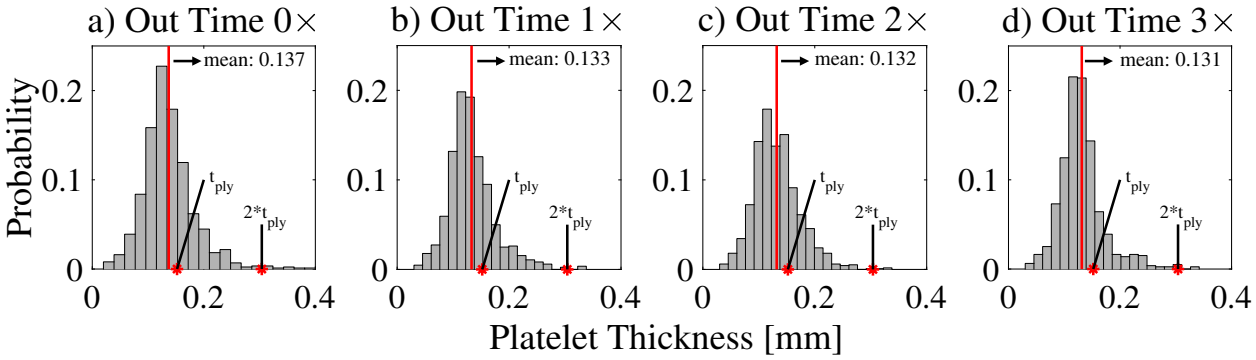

Figure 2.11: Histogram of the platelet thickness for all out times. The red stars in the histogram represents multiples of the cure ply thickness stated in the T700/2510 material data sheet, and the vertical red line represents the average platelet thickness.

Figure 2.13 and table 2.2 provide information on the fiber and void area fractions. It can be seen from fig. 2.13a, that the fiber area fraction does not change with age, and that the fiber area fractions of the DFC specimens are equal to those of the quasi-isotropic laminate. Moreover, fig. 2.13b, shows that the unaged DFCs have a void area fraction similar to that

a) Area with void

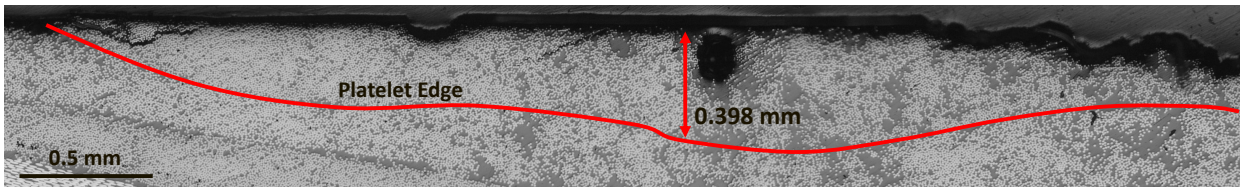

b) Resin rich area

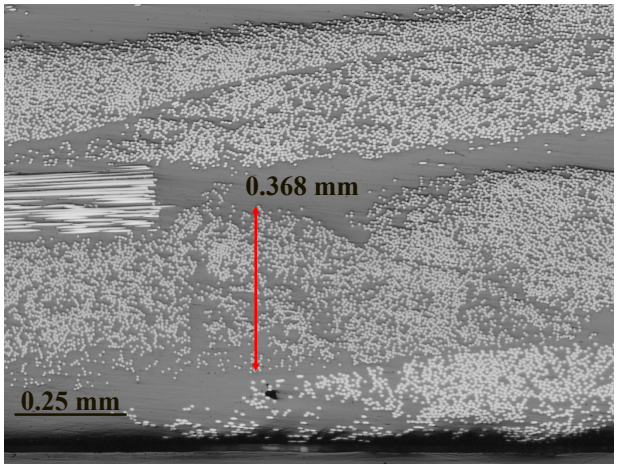

Figure 2.12: Microscope images of two DFC specimens. a) Shows the increase in platelet thickness caused by a void. b) Shows the increase in platelet thickness caused by lack of platelets when compared to the average number of platelets through the thickness.

of the quasi-isotropic layup, and that the void area fraction of DFCs increases with age. In fact, the quasi-isotropic and unaged DFCs have a void volume fraction of 0.29% and 0.24% respectively while all the aged DFCs have a void area fraction of about 1%.

The void volume fraction does not change between out times, and the maximum and minimum void content also do not change between the aged DFCs. The minimum void content observed was $0.13\%, 0.16\%$, and 0.11% for out times $1\times, 2\times$, and $3\times$ respectively while the maximum void content observed was $2.98\%, 3.12\%$, and 2.63%. The variation of the aged specimens is much higher than the quasi-isotropic and unaged specimens.

It is hypothesized that the increase in specimen thickness could be from an increase in viscosity of the prepreg caused by aging. It has been found in previous studies that with the increase in prepreg out time, there is an increase in the viscosity of epoxy [81, 83, 84].

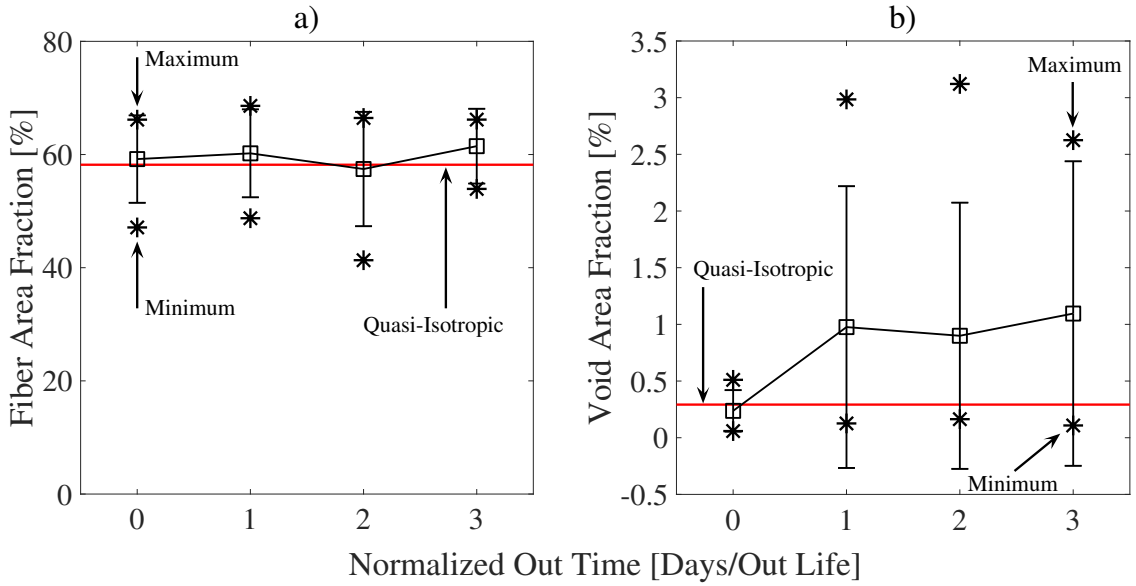

Figure 2.13: a) Fiber and b) void area fractions for a unaged quasi-isotropic laminate, and DFCs at various out times. The stars represent the maximum and minimum area fraction of the DFC laminate at various out times.

This increase in viscosity would decrease the platelet flow during the curing process leading to less platelet reorientation during curing and causing the number of platelets through the thickness to increase for the same hot press temperature and pressure. This decrease in flow is also supported by the fact that there is an increase in void area fraction with age as shown in fig. 2.13. If there was flow during curing, platelets and resin can fill the volume where there are less platelets, which would lead to a lower void area fraction. This can be seen in the lower void area fraction in the unaged DFCs compared to the aged ones.

Another important morphological observation obtained in this work is that the fiber area fraction of the DFC specimens is all the same as the quasi-isotropic specimens, about 60%. This is different from typical short fiber composites who has a fiber area fraction of about $25 - 40\%$ [26]. When looking at the application of recycling, this is a huge improvement. Typically when recycling prepreg, the resin is removed from the fiber and the fiber is milled into powder, chopped into short fiber, or made into mats. The option most comparable to DFCs would be short fibers, which would have a much lower fiber area fraction than DFCs. If

DFCs are used for recycling there would be no decrease in fiber area fraction. The void area fraction increases with age for DFCs. This is also seen in previous studies [84]. Even with the increase in void area fraction, the fiber volume fraction remains still very high. At the high end, void content was about 3% for most of the samples investigated in this work, and at the low end it was comparable to the void content in the unaged DFC and quasi-isotropic laminate. With changes in the curing process to account for the increase in viscosity with age and with extra care to evenly distribute platelets, it may be possible to decrease the void content to be comparable with the unaged specimens. However, decreasing void content may not be necessary. Voids have less impact on the structural behavior of DFCs than with continuous fiber laminates and, different from continuous fiber composites, void content of 3% may be acceptable for DFCs. Also, it was seen that even with the increase in void content, the modulus of aged specimen did not change and the strength increased. This shows the impact of voids on the mechanical properties of aged DFCs to be minimal.

2.4.3 Mechanical properties

2.4.3.1 Fracture surfaces

Figures 2.14-2.16 shows examples of fracture surfaces of tension, compression, and shear specimen at various out-times. Similar to unaged specimens seen in previous papers [10, 12, 28, 85, 86], the failure path can be seen to go around platelets or within a platelet. Fiber breakage still occurs, however its frequency is much lower in comparison to delamination and matrix damage since the failure attempts to take the path of least resistance thus avoiding fiber breakage. There was no perceivable difference in failure mechanisms between out times.

When compared to the quasi-isotropic specimen in fig. 2.15-2.16, the failure of the DFC specimen is much less brittle. For the compression specimen, the quasi-isotropic specimen exhibited a much more explosive failure and a lot of fiber breakage. Similarly, the shear specimen had more fiber breakage at the surface 45° ply. However, initiation of failure occurred at the notch and propagated along the fibers.

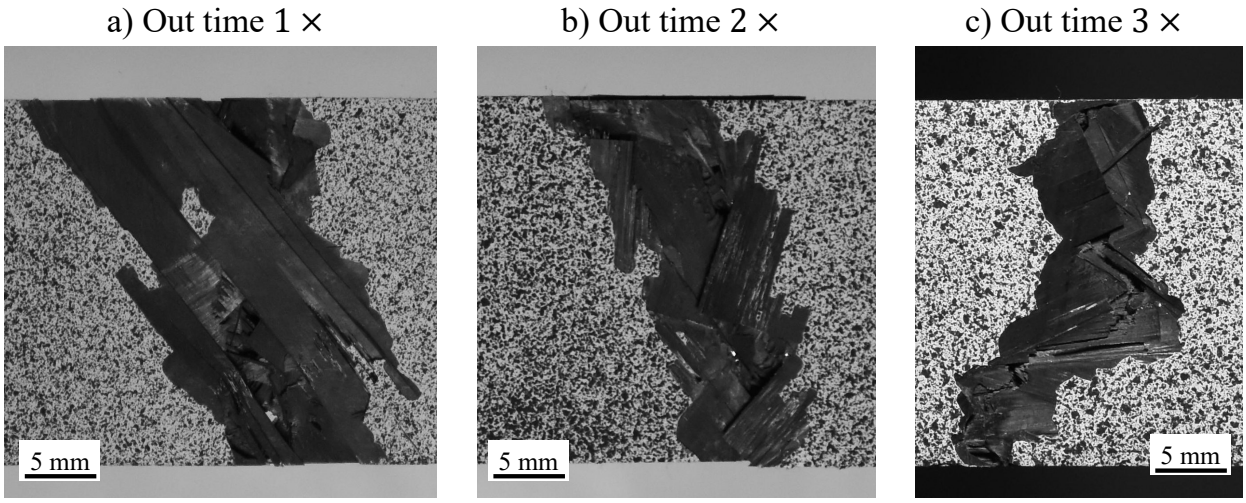

Figure 2.14: Fracture surfaces of out times 1×, 2×, and 3× tension specimen, which mainly exhibit matrix damage and debonding, with some fiber damage.

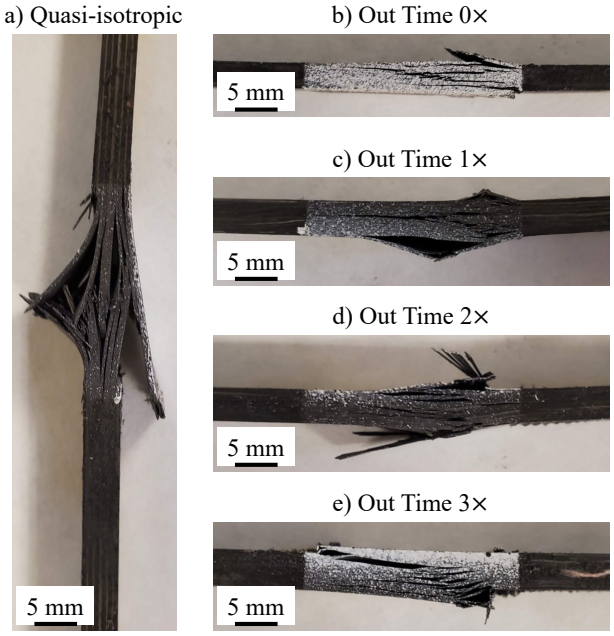

Figure 2.15: Fracture surfaces of quasi-isotropic, and DFC compression specimen out times 0×, 1×, 2×, and 3×. DFC specimens mainly exhibit matrix damage and debonding, with some fiber damage.

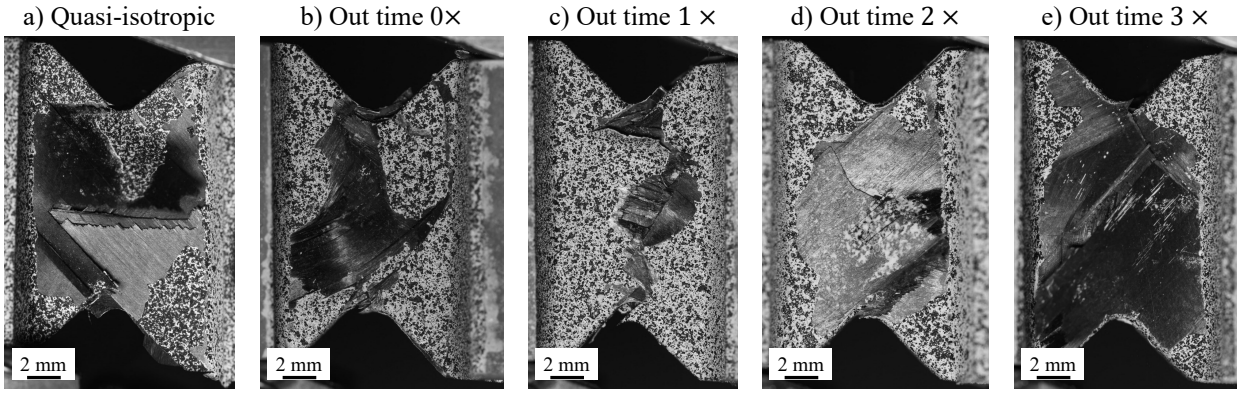

Figure 2.16: Fracture surfaces of quasi-isotropic, and DFC shear specimens out times 0×, 1×, 2×, and 3×. DFC specimens mainly exhibit matrix damage and debonding, with some fiber damage.

2.4.3.2 Stress vs strain

Figures 2.17-2.19 shows the stress vs strain curves obtained from tension, compression, and shear tests. It can be seen that all the tensile specimen was linear up to the peak, whereas the compression and shear specimen exhibit non-linear behavior before the peak. The shear specimen had a consistent amount of specimen that exhibited non-linearity, whereas the compression specimen had a decrease in non-linear behavior with an increase in out time. The non-linear behavior seen in both tests can be attributed to sub-critical damage dissipating energy before reaching the ultimate load.

For all the tests, there was progressive damage seen in all specimens. For of out time 3× specimen with the lowest tensile modulus shown in fig. 2.17, it can be seen that at about 50% the ultimate strength there was damage, however the specimen was still able to carry load. This is a property of DFCs: where there is an area with less favorable fiber orientation there will be damage, however the areas with favorable orientation can carry more load.

For compression tests, it can be seen in fig. 2.18 that when the nominal stress was at about 200 MPa, that there could be unloading, this is caused by the fact that the compression fixture grips are wedges [54] and must readjust at this point. However, this reorientation does not effect the modulus or the strength, and the effects of the reorientation can be taken out through DIC.

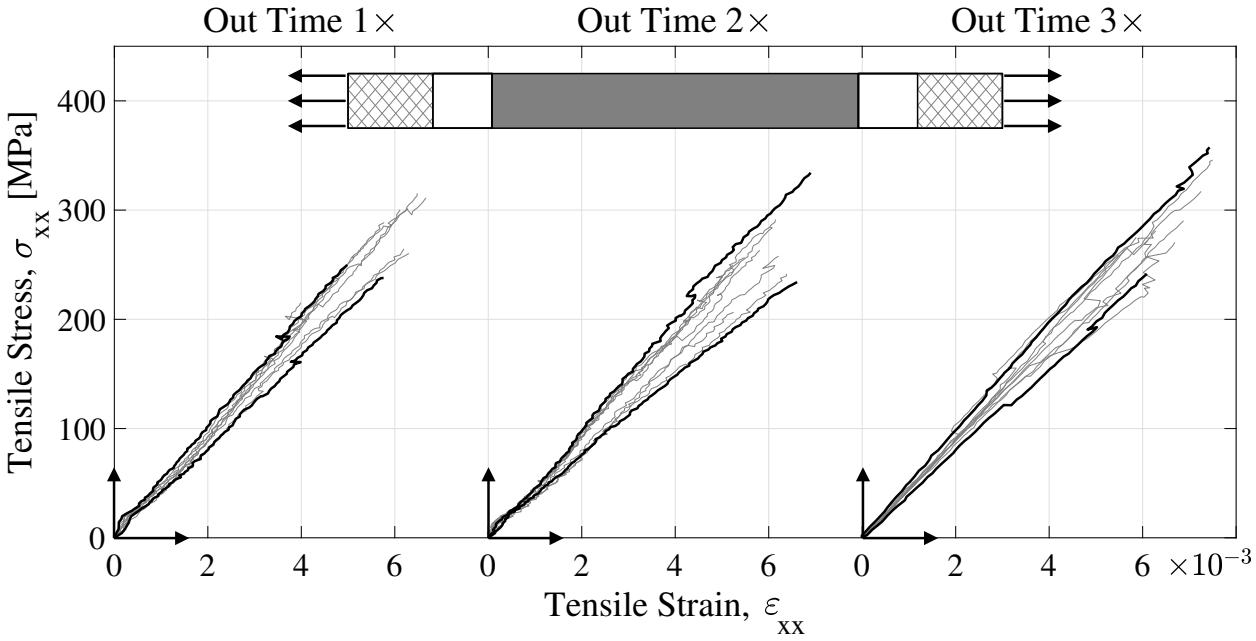

Figure 2.17: Stress vs strain curves for out times 1×, 2×, and 3× tension specimen.

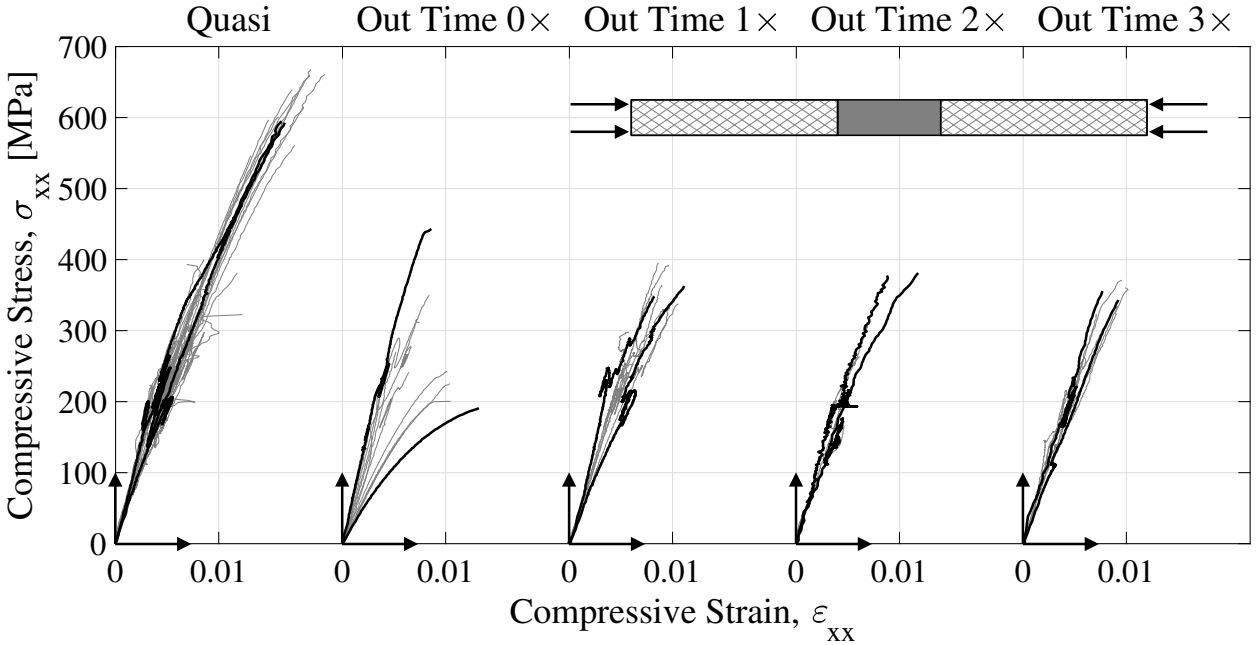

Figure 2.18: Stress vs strain curves for quasi-isotropic and out times 0×,1×, 2×, and 3× compression specimens.

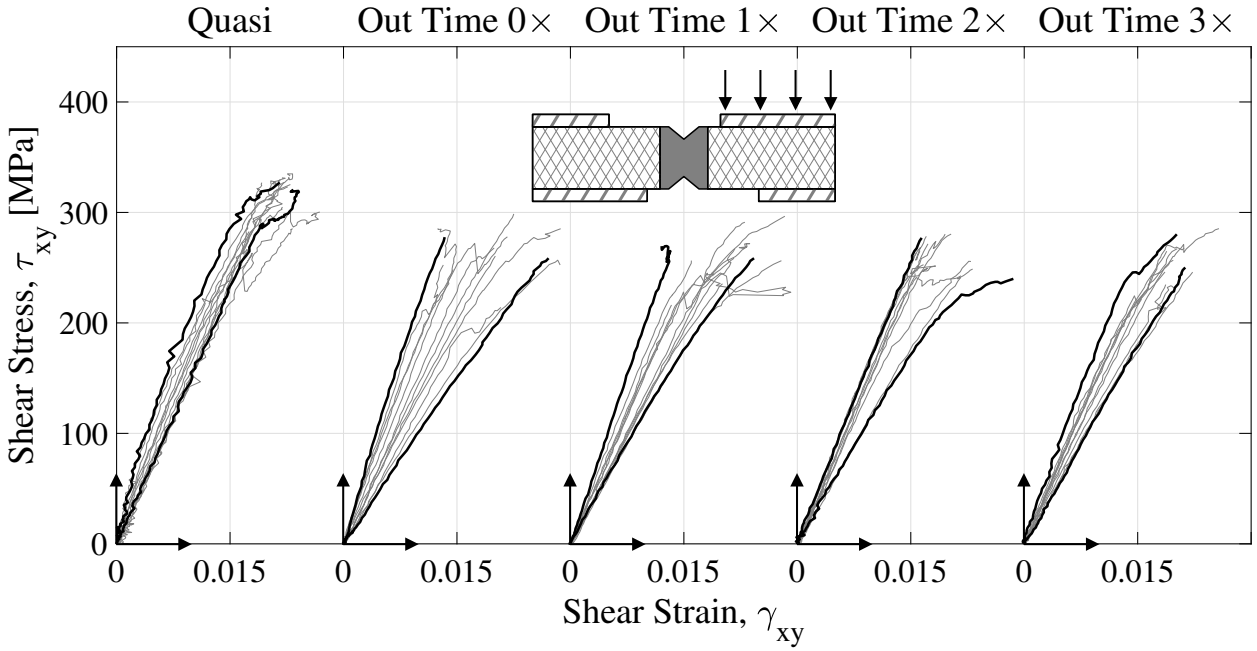

Figure 2.19: Stress vs strain curves for quasi-isotropic and out times 0×, 1×, 2×, and 3× shear specimens.

2.4.3.3 Modulus

Figure 2.20 and tables 2.3-2.5 provide information on the modulus of quasi-isotropic and DFC specimens. It can be seen in fig. 2.20, that for all tests, that the modulus does not change significantly with age and there is little difference when compared to the quasi-isotropic value. The modulus for the DFC specimens remains at $81 - 97\%$ that of the quasi-isotropic modulus. The tensile specimen retains its modulus the most, with the largest percent difference in modulus being 91.6% that of the quasi-isotropic modulus. The compression and shear specimen are comparable with the largest percent difference in modulus being 82.9% and 81.06% that of the quasi-isotropic modulus respectively. The largest percent difference in modulus occurred at out time 2× for tension and compression specimen, and at out time 3× for the shear specimen. These out times with the largest percent difference still fall within one standard deviation of the unaged DFC specimens confirming the minor effect aging has on the elastic behavior of DFCs. This consistent modulus with age has also been seen in continuous

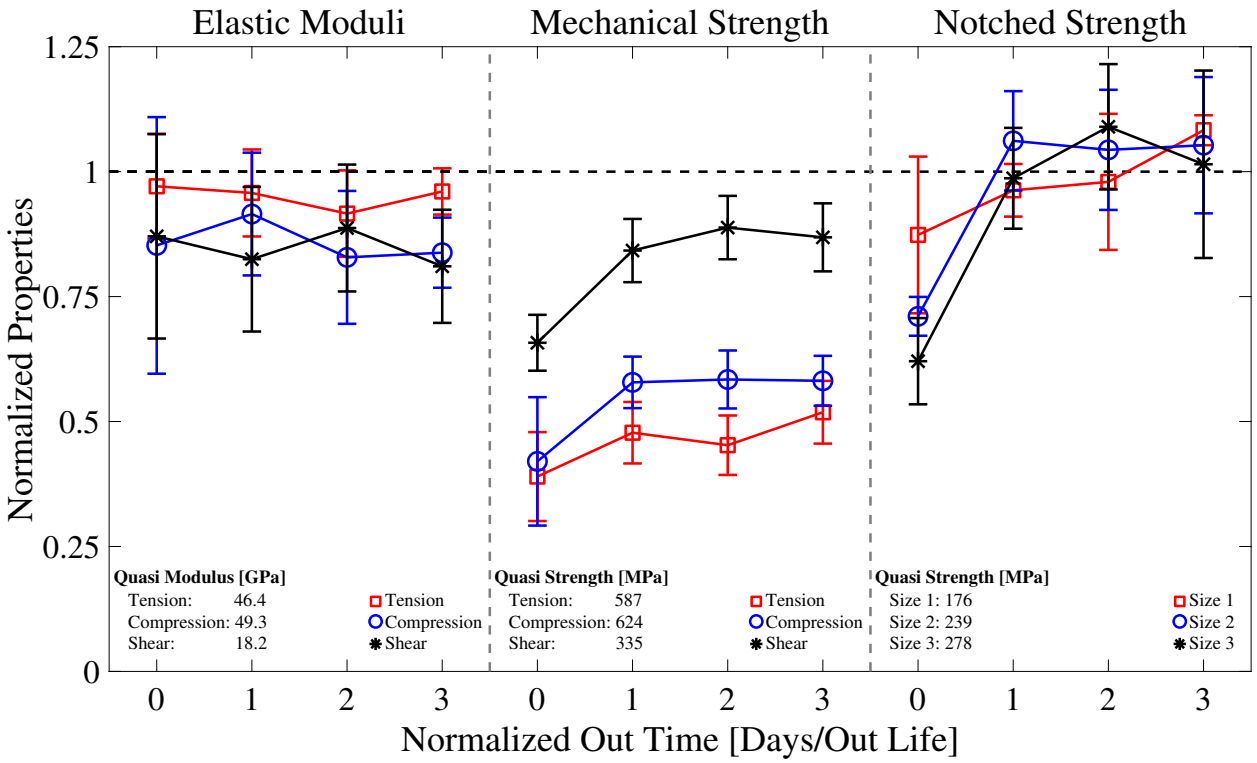

Figure 2.20: Normalized modulus and strength found from mechanical and size effect tests normalized to their respective quasi-isotropic values. Quasi-isotropic and unaged DFC results for tension and SENT specimen are obtained from Ko et al. [34].

fiber composites [78, 83, 87–90], and in DFC tension and flexure specimens [19–21, 46]. The coefficient of variation (CoV) of the modulus decreases with an increase in out time. However, this could also be attributed to the increase in the number of platelets through the thickness.

2.4.3.4 Strength

Figure 2.20 and tables 2.3-2.5 provide information on the strength of quasi-isotropic and DFC specimens. It can be seen that the strength of the unaged tension, compression, and shear DFC specimens are 39%, 42%, and 66% that of the quasi-isotropic laminate respectively. Once aged, the strength of all specimen increased by about 30% and after out time 1× there is little change in the strength. This is different to what has been seen in previous studies

Table 2.3: Tensile modulus and strength of unaged quasi-isotropic and aged DFC. Quasi-isotropic and unaged DFC results are taken from Ko et al. [48].

Type	Specimen Tested	Modulus [GPa] (%)	Strength [MPa] (%)
Quasi	11	46.40 ± 1.11 (2.39)	587.10 ± 27.86 (4.75)
OT 0×	11	45.04 ± 4.87 (10.81)	228.90 ± 52.20 (22.80)
OT 1×	10	44.42 ± 4.04 (9.09)	280.41 ± 36.10 (12.87)
OT 2×	10	42.50 ± 4.02 (9.45)	265.73 ± 34.92 (13.14)
OT 3×	10	44.56 ± 2.15 (4.82)	304.43 ± 36.82 (12.09)

Table 2.4: Compression modulus and strength of unaged quasi-isotropic and aged DFC.

Type	Specimen Tested	Modulus [GPa] (%)	Strength [MPa] (%)
Quasi	12	49.28 ± 6.55 (6.21)	623.81 ± 38.74 (13.29)
OT 0×	12	42.01 ± 12.65 (30.11)	262.16 ± 80.14 (30.57)
OT 1×	8	45.10 ± 6.05 (13.42)	360.79 ± 32.16 (8.91)
OT 2×	8	40.83 ± 6.55 (16.05)	364.39 ± 36.18 (9.93)
OT 3×	8	41.29 ± 3.46 (8.38)	362.73 ± 31.17 (8.59)

Table 2.5: Shear modulus and strength of unaged, quasi-isotropic, and aged DFC.

Type	Specimen Tested	Modulus [GPa] (%)	Strength [MPa] (%)
Quasi	12	18.19 ± 3.42 (18.82)	334.67 ± 29.18 (8.72)
OT 0×	12	15.83 ± 3.72 (23.49)	220.09 ± 18.71 (8.71)
OT 1×	12	15.00 ± 2.63 (17.54)	281.84 ± 21.17 (7.51)
OT 2×	12	16.14 ± 2.31 (14.31)	297.23 ± 21.22 (7.14)
OT 3×	12	14.74 ± 2.06 (13.96)	290.67 ± 22.78 (7.84)

done on continuous fiber composites [78,83,87–90]. In fact, in these studies it was shown that if the mechanical property had more dependence on the matrix, such as 90° tension, then there would be a decrease in strength, and if it had more dependence on the fibers, such as 0° tension, then the strength would not change with age. It is worth mentioning that an increase in tensile strength [19–21, 46] and flexure strength [21] with prepreg age for DFCs was seen in previous studies. Nilakantan et al. and Sultana et al. [19, 20, 46] both saw increases in tensile strength of about $30 - 40\%$. George et al. [21] saw little change in the tensile and flexure strengths of DFC specimen as the uncured prepregs' glass transition temperature increased, similar to what was seen here when comparing out times $1\times, 2\times$ and $3\times$. The present work also investigates the effect of aging also on the compression and shear strengths and to confirm that such strengths increase with age. This is a very important result since recycled DFC components can be subject to a large variety of loading conditions, not only uniaxial tension. Thanks to the results presented in this work, it is possible to conclude with confidence that the structural capacity of a recycled DFC component is not affected by age. On the contrary, the structural capacity might slightly increase.

By looking at work done on aging of cured epoxy and composites we can gain insight on what could be the reason for the strength increase. Work by Zhou et al. [91] has shown that there are two types of bonding that can occur when cured epoxy is aged in distilled water. The first type of bond corresponds to one hydrogen bond between the water molecule and the resin network. This breaks the initial interchain Van der Waals forces resulting in increased mobility of the chains and plasticization of the epoxy. The second type of bonding happens when the water molecules form multiple hydrogen bonds and act as a pseudo-crosslink. This plasticization effect can be seen in aging of a cured laminate and aging of prepregs. Asp [92] found that when composites were aged in high humidity and temperature, mode I fracture energy increased when testing at room temperature and at 100°C. Sharp [93] allowed the prepreg used for the center plies of the laminate to absorb 0.5% of its weight in water before curing. This resulted in an increase in mode I and mode II fracture energy, similar to what was found to happen when cured laminates absorbed water. Blass et al. [78] aged two

prepregs in a standard ambient temperature and humidity and performed Double Cantilever Beam (DCB) tests to find mode I fracture energy. Here one of the prepregs tested showed no changed in fracture energy after 120 days (12× out life), while the other prepreg tested had an increase in fracture energy. The increases in fracture energy seen in previous works can be linked to the plasticization of the epoxy. In DFCs, the failure is due to a combination of fiber and matrix damage mechanisms, so the plasticization allows the epoxy to absorb more energy before failure and the fibers can carry that extra load, resulting in a higher strength which is not seen in continuous fiber composites. With continuous fiber composites the plasticization reduces the strength, however since DFCs have a random network of fiber that are in various directions, the fibers can carry more load with the additional energy absorption of the plasticized matrix.

2.4.4 Fracture properties

2.4.4.1 Fracture surface

Figures 2.21a-c show the three types of fracture surfaces of SENT Discontinuous Fiber Composite specimens. Figure 2.21a shows a fracture that occurred at the notch. Similar to three mechanical tests, matrix damage and debonding were much more common than fiber breakage. Figure 2.21b shows a fracture that happened at the notch, but not at the tip. This type of failure occurred in two specimens, one in out time 1×, size 3, and one in out time 2×, size 2. There was initial damage at the notch tip, however due to the size of the fracture process zone (FPZ), damage happened to platelets not directly touching the notch tip. Thus when the platelet failed, the fracture path was not connected to the notch tip.

Figure 2.21c shows fracture that occurred away from the notch. It can be seen that there was damage at the notch before ultimate failure, however the ultimate failure occurred away from the notch. It was seen for out time 1×, 1 out of 8 specimen failed away from the notch, and for out time 2× and 3×, 2 out of 8 specimens failed away from the notch. For the two larger sizes all the specimen failed at the notch. The specimens that failed away from the

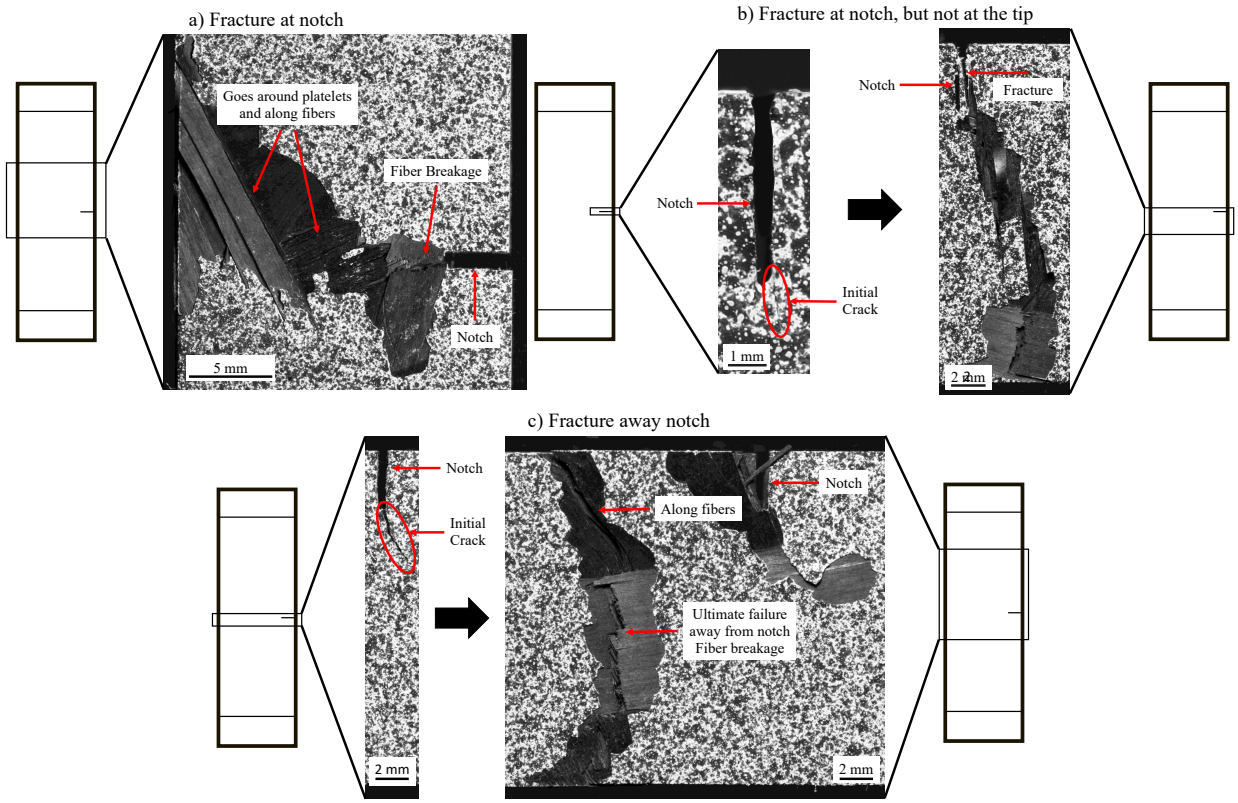

Figure 2.21: Three different types of fracture surfaces of SENT specimens, which mainly exhibit matrix damage and debonding, with some fiber damage.

notch or at the notch but not at the tip, showed no difference in nominal strength when compared to specimen that failed at the notch. Previous studies [34, 35, 48, 94, 95] have seen similar fracture behaviors presented here in unaged DFCs.

2.4.4.2 Load vs Displacement

Figure 2.22 shows the load vs displacement curves for out time 1×, 2×, and 3× DFC specimens. The stiffness of each specimen was seen to be relatively the same. Most of the specimens had a linear behavior up to the peak, however, some specimens in out time 3× size 3 exhibited minor non-linearity. This non-linear behavior comes from damage in the FPZ.

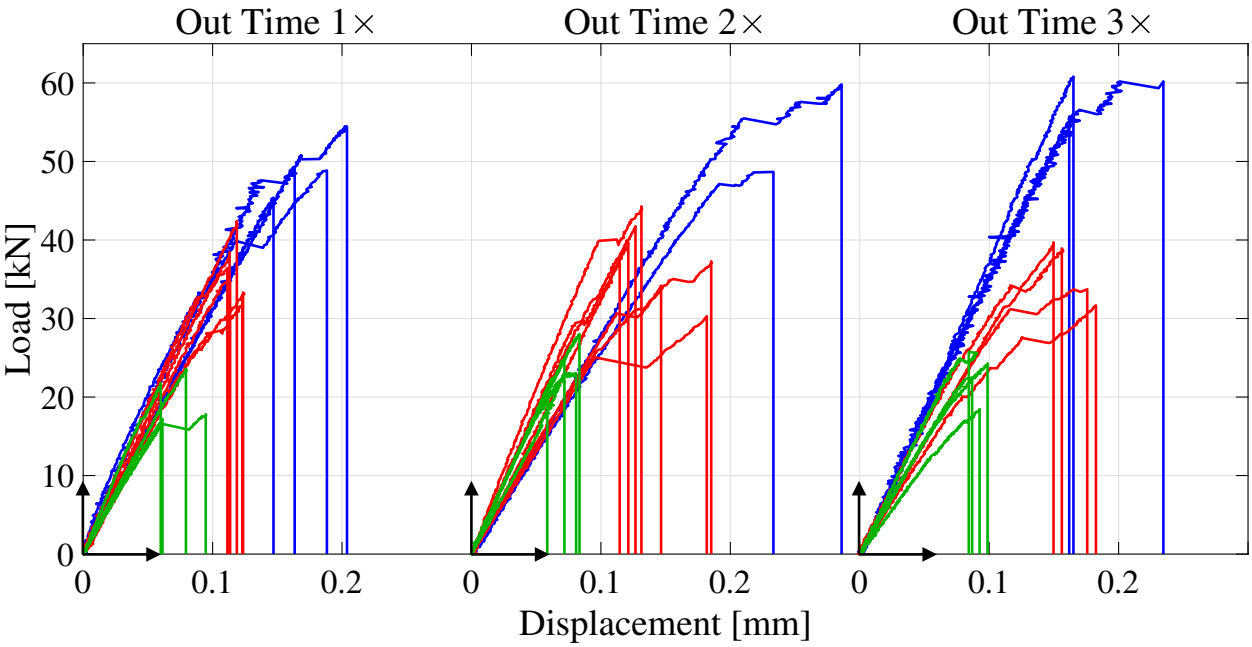

Figure 2.22: Load vs displacement curves for out times 1×, 2×, and 3× SENT specimens.

2.4.4.3 Strength

Figure 2.20 and table 2.6 report the nominal strength for the DFC and quasi-isotropic specimens. It can be seen that there was an increase in strength with aging, similar to the mechanical tests. In this case, the aged DFC specimens have a nominal strength similar to that of the quasi-isotropic specimens. The average percent increase in strength for size 1, 2, and 3 specimens were 15%, 48%, and 66% respectively. At the same time a size effect can be seen where the strength of the SENT specimen increases with a decrease in specimen width.

2.4.4.4 Size effect curve

Figure 2.23 shows the normalized size effect curves found using eq. 2.6. Here, the log of the nominal stress normalized to the size effect constant σ_0 is plotted against the log of the structural width D normalized to the size effect constant D_0. As can be noted, all out times exhibit a deviation from LEFM. It can be seen that the specimens tested are in the transition

Table 2.6: Failure strength of unaged quasi-isotropic, and aged DFC SENT specimen and the number of specimen tested. Quasi-isotropic and unaged DFC results are taken from Ko et al. [34].

	Average failure strength [MPa] (%), Number of specimens tested		
Type	Size 1	Size 2	Size 3
Quasi	176.1 ± 9.73 (5.53), 3	238.6 ± 23.20 (9.72), 8	277.9 ± 31.54 (11.35), 6
OT 0×	153.8 ± 27.61 (17.95), 3	198.2 ± 14.90 (5.49), 5	214.2 ± 14.58 (13.90), 4
OT 1×	169.5 ± 9.27 (5.47), 4	253.3 ± 23.73 (9.37), 8	274.2 ± 28.03 (10.22), 8
OT 2×	172.5 ± 23.97 (13.90), 2	249.0 ± 28.67 (11.52), 8	302.9 ± 34.85 (11.51), 8
OT 3×	190.7 ± 5.28 (2.77), 3	251.2 ± 32.54 (12.95), 8	282.0 ± 52.11 (18.48), 8

between the horizontal asymptote, which dictates stress driven failure, and the asymptote with a slope of $-1/2$, where failure is fully energy driven and LEFM is valid. This can be attributed to the size of the Fracture Process Zone (FPZ) compared to the structure size. In the FPZ, significant non-linear deformations due to sub-critical damage mechanisms, such as platelet delamination, matrix microcracking, and platelet splitting/fracture, promote strain redistribution and mitigate the intensity of the stress field induced by the notch. The size of a fully-developed FPZ is typically a material property and thus its influence on the structural behavior becomes increasingly significant as the structure size is reduced. For sufficiently large structures, the size of the FPZ becomes negligible compared to the structure's characteristic size in agreement with the inherent assumption of the LEFM that non-linear effects are negligible during the fracturing process. It is interesting to note that out time 1× and 2× are closer to the LEFM region and are comparable to the quasi-isotropic specimen. Then once out time 3× is reached, the specimen becomes comparable to out time 0× and becomes more quasi-ductile. This is most likely due to out times 0× and 3× having a FPZ size much larger than the other two out times and the quasi-isotropic specimen.

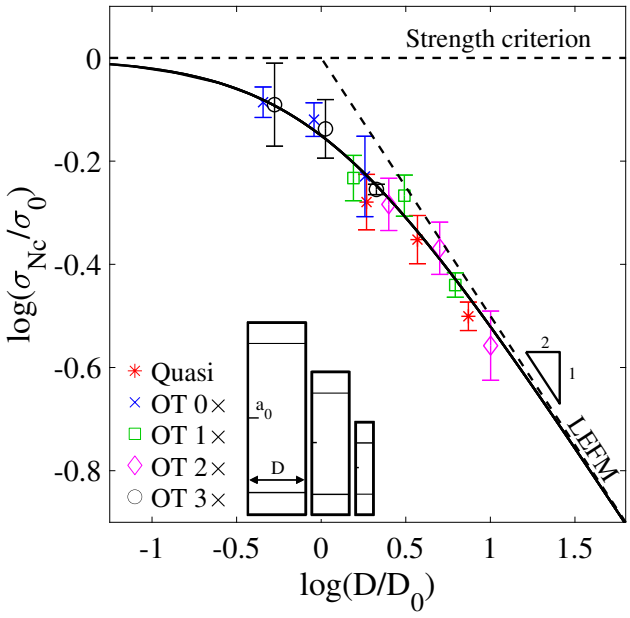

Figure 2.23: Normalized size effect curves for quasi-isotropic, unaged DFC, and aged DFC specimens. Y-values are normalized to the size effect constant σ_0, and the x-values are normalized to the size effect constant D_0. Quasi-isotropic and unaged DFC results are obtained from Ko et al. [34]

2.4.4.5 Fracture energy and characteristic length

Figure 2.24 and table 2.7 show the fracture properties. It can be seen that there is little change in the fracture energy when going from out time 0× to 1×. When increasing the out time to 2× there is a decrease in the fracture energy, and when increasing to 3× the out life, there is a large increase in the fracture energy. The fracture energy of out time 2× becomes close to the fracture energy of a quasi-isotropic layup, but then increases by 1.7× when going to out time 3×. A similar trend found in the fracture energy can be seen for the characteristic length in out times 2× and 3×. In addition to these trends, the characteristic length also decreases when going from out time 0× to out time 1×. The characteristic length of out time 1× and 2× becomes about the same as a quasi-isotropic laminate. It is worth noting that the characteristic length of out times 0× and 3× are comparable to the width of the platelets.

Table 2.7: Fracture properties obtained from size effect experiments and the stochastic finite element analysis. Quasi-isotropic and unaged DFC results are taken from Ko et al. [34].

Type	G_f [N/mm]	c_f [mm]
Quasi	41.01 ± 11.28	1.85 ± 0.31
OT 0×	55.05 ± 13.23	6.41 ± 0.49
OT 1×	52.19 ± 10.40	1.99 ± 0.56
OT 2×	42.29 ± 6.18	1.18 ± 0.24
OT 3×	75.53 ± 7.70	5.25 ± 0.76

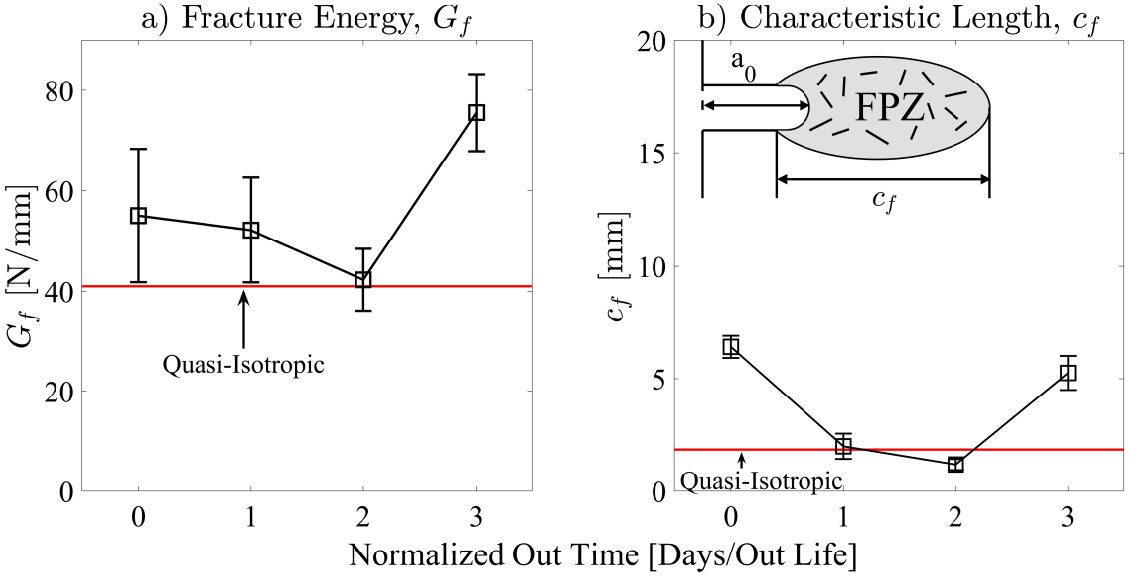

Figure 2.24: a) Fracture energy and b) characteristic length as a function of the prepreg out time compared to a pristine quasi-isotropic values. Quasi-isotropic and unaged DFC results are taken from Ko et al. [34].

There are two phenomena with contrasting effects at play that are causing the decrease and increase in these properties. The first phenomenon is the increase in thickness of the specimen with increasing age. Ko et al. [35] reported that the fracture energy and characteristic length are strongly effected by the thickness. It was seen that the fracture properties will increase up to a certain thickness and then hit a plateau. At the plateau it is possible

that the increase in thickness will cause a decrease in the fracture properties. Ko et al. saw that when the thickness increased from 2.2 mm to 3.3 mm the fracture energy increased, but when the thickness increased from 3.3 mm to 4.1 mm the fracture energy decreased. This phenomenon is exactly what is happening for out time 1× and 2×.

The second phenomenon affecting the fracture properties is the plasticization of the matrix with aging which leads to an increase of the fracture energy. The effect of plasticization can be seen in the fact that for even though there is a thickness increase from out time 0× to out time 1× there is no change in the fracture energy. It was seen by Blass et al. [78], that with increase in prepreg out time, the mode I fracture energy would increase or remain constant. It is believed that this retention or increase is caused by the plasticization of the matrix that happens with aging. The thickness change and plasticization are fighting each other to change the fracture properties. This can also been seen in the fact that the rate at which the fracture properties change when going from out time 0× to 1× and out time 1× to 2× changes. The rate of decrease in properties becomes lower which indicates the plasticization taking effect and then when out time 3× is reached, the plasticization is developed enough to increase the fracture properties.

2.5 Conclusions

This work investigated the effects of out time on the mechanical and fracture properties of Discontinuous Fiber Composites (DFCs) for the use in recycling of thermoset prepreg material. Prepreg was aged to 1×, 2×, and 3× the out life of the prepreg (28, 56, and 84 days) and compared with unaged DFC and quasi-isotropic specimens. Based on this study the following conclusions can be drawn:

1. As the prepreg ages, the viscosity of the resin increases which leads to an increase in the number of platelet through the thickness and void content in compression molded DFC plates. However, voids do not impact the mechanical properties of DFCs the same way they would for continuous fiber composites. This is why a degradation in mechanical

properties is not seen. In any case, some steps could be taken to mitigate the increase in voids, such as increasing the compaction pressure while curing, but this would need to be investigated in future work.

2. The experimental results on tensile, compression, and shear specimens showed that prepreg out time has no effect on the moduli of DFCs, even when the out time reached 3× the out life of the prepreg. Additionally, these tests and the geometrically-scaled Single Edge Notch Tension (SENT) tests showed there is a strengthening effect of aging on DFCs. This is due to the plasticization of the matrix leading to higher energy absorption and allowing the fibers to carry more load.

3. The experimental results on the geometrically-scaled SENT specimen for the various out times showed a significant size effect on the nominal strength. As the size of the specimen increases, the nominal strength approached Linear Elastic Fracture Mechanics (LEFM). For smaller specimen, the fracture can exhibit a more pseudo-ductile behavior and deviate from LEFM. This can be attributed to the development of the Fracture Process Zone (FPZ).

4. At a given out time the fracture behavior of geometrically-scaled SENT specimens changes to be quasi-ductile to brittle and back to quasi-ductile. Out time 0× specimens exhibit a much more quasi-ductile or quasi-brittle behavior, depending on the specimen size. For out time 1× and 2×, the behavior was much closer to the LEFM regime, similar to the quasi-isotropic specimen, being much more brittle at the structure sizes tested when compared to out time 0×. However for out times 3× the behavior became similar to that of out time 0×, exhibiting much more quasi-ductile behavior. This is caused by two factors, the first being a thickness effect, and the second being the plasticization caused by aging.

5. It should be noted that if the aging conditions change, the rate of the effects seen in

this study will change. For a lower temperature, the ambient curing would be slower, whereas a higher temperature would lead faster ambient curing. This would lead to a change in the state of the epoxy, and when the strengthening effect occurs could change to before or after 1× the out life. Thus, instead of out time it may be advantageous to use degree of cure or glass transition temperature when deciding the optimal time to make a DFC laminate out of repurposed prepreg. Also, if the humidity while ambiently curing changes, the degree of plasticization of the matrix increasing or decreasing depending on if aging occurs in low or high humidity. From the results presented in this work, for prepreg aged at 23°C and 50%RH, the optimum out time appears to be 3× the out life of the prepreg. At this out time the elastic moduli are the same as the unaged DFC, and the strength and fracture energy are both higher than the unaged DFC.

6. An important takeaway from the results presented in this work is that utilizing repurposed prepregs to manufacture DFCs is a great way to mitigate the impact of scrap thermoset materials on the environment. In fact, in contrast to other recycling technologies which might damage the fibers, the mechanical properties of DFCs made from old prepregs compared to DFCs made from virgin materials are retained or improved. The recycling process is also safe, easy, and environmentally friendly. More work can be done to investigate ways to prevent the change in the void content and laminate thickness with aging, however with the current study it can already be seen that DFCs represent a great form of recycling thermoset composite materials largely produced by the aerospace and automotive industries.

Chapter 3

RECYCLED DISCONTINUOUS FIBER COMPOSITES FOR INDUSTRIAL APPLICATIONS: EFFECTS OF PLATELET SIZE, THICKNESS, AND CONTINUOUS FIBER PLIES ON FLEXURE PROPERTIES

3.1 Introduction

Some application for R-DFCs and DFCs, are springs used in food processing conveyor systems, fig. 3.1a, and brackets, fig. 3.1b. However, one big challenge when using this material is that the variation in performance is much higher when compared with other composites, due to the random nature of the mesostructure. This high variation is a problem for the applications presented in fig. 3.1. In the case of a vibratory conveyor system, the arms vibrate at their resonance frequency, which is found by using the flexure modulus. If the variation in the flexure modulus is high, the arms will not be able to vibrate using the same frequency. The flexural properties are especially sensitive to the random mesostructure, since both through thickness and in-plane variation of orientation will play a large role in the overall variation of flexure properties. At the same time, when designing parts such as the bracket in fig. 3.1b, the design allowable is typically found using the B-basis. The B-basis is defined as the 95% lower confidence bound on the tenth percentile of a specified population of measurements [96]. Thus if the variation is high, the design allowable will be lower. With these two factors in mind, the work done in this study aims to find ways to reduce variation in R-DFCs.

Previous works on DFCs in flexure are limited [28, 38, 99–101]. Larson et al. [100] looked at DFCs with a platelet size of 25×25 mm and 25×12.7 mm in a short beam configuration (span to thickness ratio of $6:1$) made with woven glass fiber prepreg. They also investigated

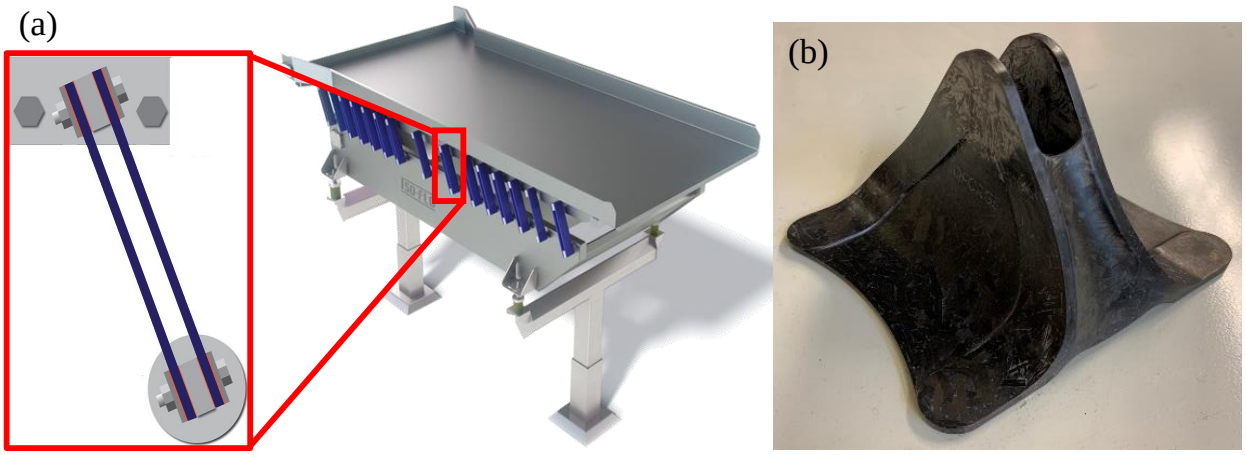

Figure 3.1: Examples of possible R-DFC applications: (a) vibratory conveyor system manufactured by Key Technology [97], (b) bracket manufactured by Sekisui Aerospace [98].

a hybrid setup with the woven fiber mat at the surface of a DFC core. It was found that the narrow platelet had a higher strength, but lower modulus than the square platelet. The variation in strength of the narrow platelet specimen was almost twice that of the square platelet specimen, but the modulus had comparable variations. When adding the woven mat, the average properties became much closer, and the variation was lowered by as much as 1/5 the variation seen in pure DFCs. Corbridge et al. [38] looked at the effects of flow and hybridization of DFCs on the flexure modulus and interlaminar shear strength. These DFC specimen were made up of 2 DFC plies, and the hybrid specimen consisted of 2 DFC plies and 3 unidirectional (UD) plies. It was found that by inducing flow, the flexure modulus could increase or decrease by about 35%, depending on if the flow is parallel or perpendicular to the span. They also found that, even with 50% of the volume being made up of UD plies, the variation could be higher than that of the pure DFC specimen due to platelet flow causing the UD plies to become wavy. This waviness could be mitigated though a precure routine or by using a cross ply layup instead of a pure UD one. However, the precure routine resulted in a decrease in the interlaminar shear strength. Nakashima et al. [101] looked at the effects of thickness on the flexure modulus of DFCs and proposed an analytical approach to find

the flexure modulus. They found that the span-to-thickness ratio has a large impact on the flexure modulus due to shear effects. It was also found that increasing the thickness of the specimen also decreased the variation of the flexure modulus. Their analytical model could match the experiments well, however the model used the assumption that platelets can be transformed into equivalent square platelets, so if the aspect ration of the platelets are high, this method should not be used. The analytical approach also ignored resin pockets. Both Feraboli et al. and Sattar et al. [28, 99] investigated platelet size effects by increasing the length of the platelets while keeping the width constant. They found that increasing the length of the platelets increased both flexure modulus and strength, with the increase in strength being much more prominent. There was no clear trend on the effects of platelet length on the variation of the flexure properties. In addition to the experiments, Sattar et al. also simulated the tests by generating digital DFC coupons with a uniform random orientation distribution. This was able to capture the average properties well, but in some cases the variation was about half that of what was seen in experiments.

The goal of this study is to investigate the impact platelet size, specimen thickness, and the addition of continuous fiber plies on the flexure properties and their variation of R-DFCs. To do this two platelet sizes, three thicknesses, and three hybrid configurations are tested. All specimen in this study was manufactured by CRTC using repurposed prepreg. In addition to the experiments, a mesostructure generator that can have spatial variation in the orientations was implemented. By controlling the orientation variation, a more realistic mesostructure can be generated for finite element simulations.

3.2 Materials and testing methods

3.2.1 Material preparation

The material used for the platelets and unidirectional (UD) plies was T800S/3900, and the woven (PW) fiber was Cytec Cycom $5320-1$ T650 3K PW. For the investigation of platelet and thickness size effect, two platelet sizes and three thicknesses were investigated. A platelet

size of 12×9.5 mm, henceforth called platelet A, and 30×9.5 mm, henceforth called platelet B, were used. Thicknesses of 3, and 6 mm (roughly 16 and 32 platelets through thickness respectively) were investigated for platelet A and B, and an additional thickness 9 mm (roughly 47 platelets through thickness) was also investigated for platelet B.

For 9 mm platelet B specimen, the effects of adding continuous fiber plies to the outer surfaces of a R-DFC core was also investigated. If only UD plies were added, platelet motion during curing caused significant waviness of the plies. To investigate the effects of this waviness, two methods to keep the UD plies straight were implemented. The first was a precure process to limit platelet motion during the final cure, thus keeping the UD plies straight. Figure 3.2 shows the temperature and pressure of the heat plates for the precure routine. The plates are set to be 177°C and 0 MPa for 7 minutes to allow for the DFC core to reach up to temperature. Then a pressure of 1.03 MPa is applied over 1 minute. Finally, the plates are cooled to 38°C and the pressure is ramped to 3.10 MPa over 25 minutes. The pressure is increased while cooling so that the platelets can have motion while keeping resin bleeding to a minimum. The second method to prevent waviness was adding a PW ply between the DFC core and UD ply. The precure process was also implemented for the PW hybrid laminate.

In this paper, the specimen with continuous fiber plies will be referred to as hybrid specimen. If the specimen had one continuous fiber ply on the outer surfaces it is referred to as hybrid 1, and if there were two, it is referred to as hybrid 2. If not specified, it is assumed that the continuous fiber plies are UD plies and have not undergone the precure routine.

3.2.2 Mechanical tests

3.2.2.1 Data acquisition

Tests were performed using an Instron 5585H 250 kN electro-mechanical load frame with an Interface load cell with a 2.5 kN capacity. The load was recorded at a sampling frequency of 10 Hz. Digital Image Correlation (DIC) is used to obtain the displacement values needed to verify that the compliance of the machine has no effect of the displacement reading.

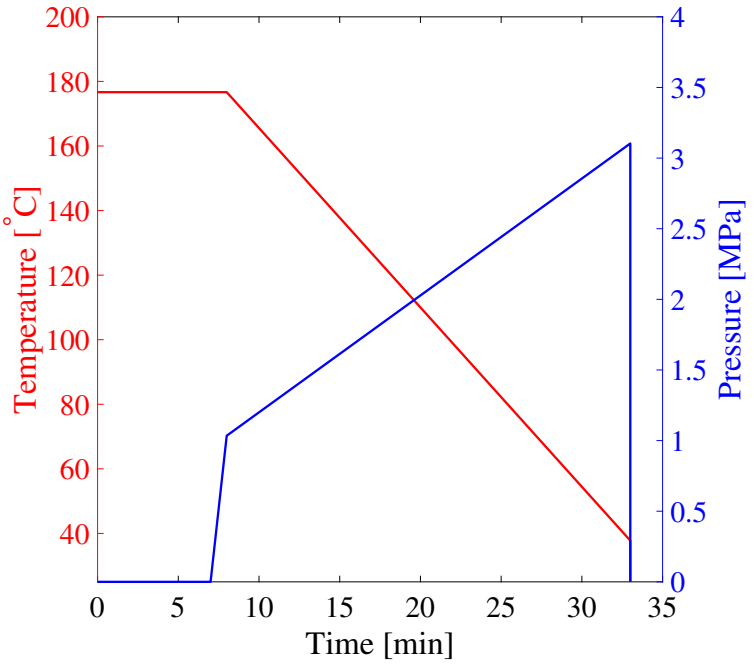

Figure 3.2: The precure routine used to limit platelet motion.

Images were captured using a Nikon D5600 DSLR camera with Nikon AF micro 200 mm and Sigma 135 mm DG HSM lenses. The images were taken with a sampling rate of 1 Hz. GOM Correlate [52] was used to process the photos and obtain the displacement values.

Figure 3.3 shows the stress vs strain curve obtained through DIC to one obtained using the displacement from the load frame. It was found that the maximum percent difference in the flexure modulus obtained by DIC and by using the load frame's displacement was 2.5%. This is a negligible difference, thus showing that the compliance of the machine has no effect on the displacement results in this study and that the displacement readings from the machine can be used in strain calculations.

3.2.2.2 Three point bending

Three point bending tests followed ASTM D790 and D7264 [102, 103]. Specimen had a constant span to thickness ration of $32:1$ with the total length being $1.2\times$ the span length. A with of 13 mm was used, and in order to see the effects of waviness, an addition width

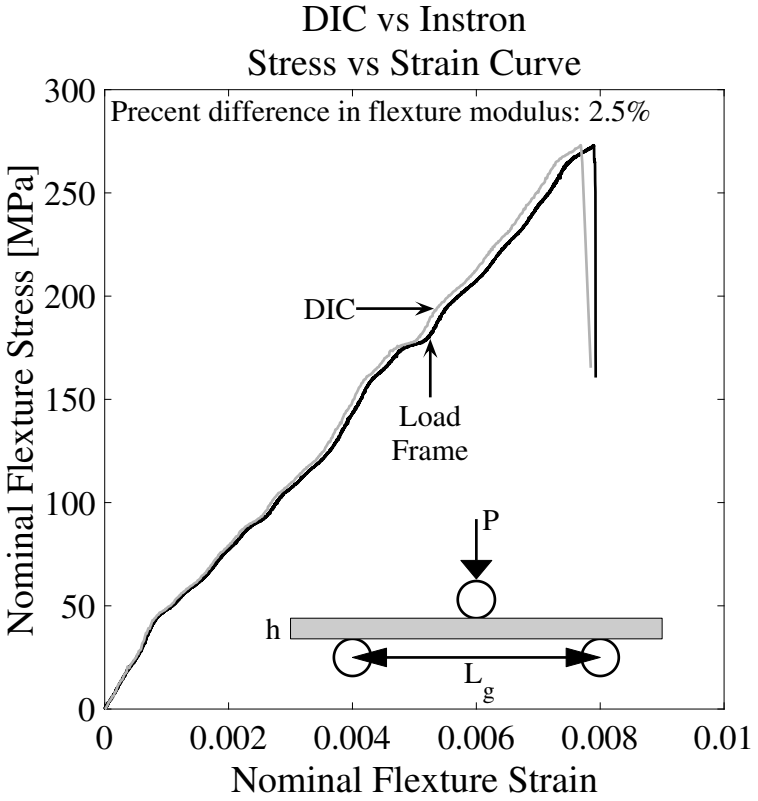

Figure 3.3: Comparison between the stress vs strain curve of a 6 mm platelet B speicmen obtained from using the displacement from the load frame to ones obtained from DIC.

of 26 mm were tested for the 9 mm DFC and hybrid specimen. The displacement rate used followed the equation stated in ASTM D790 [102]:

$$R = \frac{ZL^2}{6h} \tag{3.1}$$

Here, R is the displacement rate in mm/min, Z is the rate of straining of the outer fibers, taken to be 0.01 mm/mm/min, L is the span length, and h is the specimen thickness. Support and load pins of radius 3.2 mm was used for all specimen except the precured and woven hybrid specimen, which used 5 mm radius pins.

To calculate the nominal flexure stress and strain, the following equations are used:

$$\sigma_f = \frac{3PL}{4bh^2} \tag{3.2}$$

$$\varepsilon_f = \frac{6uh}{L^2} \tag{3.3}$$

Here, σ_f is the nominal flexure stress, ϵ_f is the nominal flexure strain, P is the reaction force, L is the span length, b is the width of the specimen, h is the thickness of the specimen, and u is the displacement. To verify that the displacement readings from the load frame could be used, displacements were found using Digital Image Correlation (DIC) and compared with the ones from the load frame. From this, it was seen that the maximum difference in displacements was 5%, thus showing that the compliance of the load frame does not impact the displacement reading and load frame displacements can be used.The number of specimen tested for each laminate type can be found in table 3.1, which also summarizes the flexure modulus and strength found.

3.2.3 X-Ray micro-computed tomography

X-Ray micro-computed tomography (μCT) was done to examine if the addition of continuous fiber plies effects the mesostructure of the R-DFCs, and to ensure there was proper bonding between the R-DFC core and the continuous fiber plies. These scans were performed on 2 specimens of type wide 9 mm, and wide hybrid 2. A NSI X5000 was used to obtain scans with a voxel size of about 25 μm [104].

3.3 Experimental results

3.3.1 Stress vs strain curves and fracture

Figure 3.4 shows the three typical stress-strain curves seen in experiments. The first type was ones where specimen fail at the first onset of fracture. The second and third are ones where there was progressive damage, where they can progress linearly or nonlinearly. Each type of stress-strain curve had no correlation to how the specimen failed. Figure 3.5 shows fracture surfaces for chip B with 6 mm thickness and their stress-strain curves. The images in the left column exhibited progressive damage, while the images in the right column failed at the first onset. The fracture surfaces between the two columns are identical, but the stress-strain

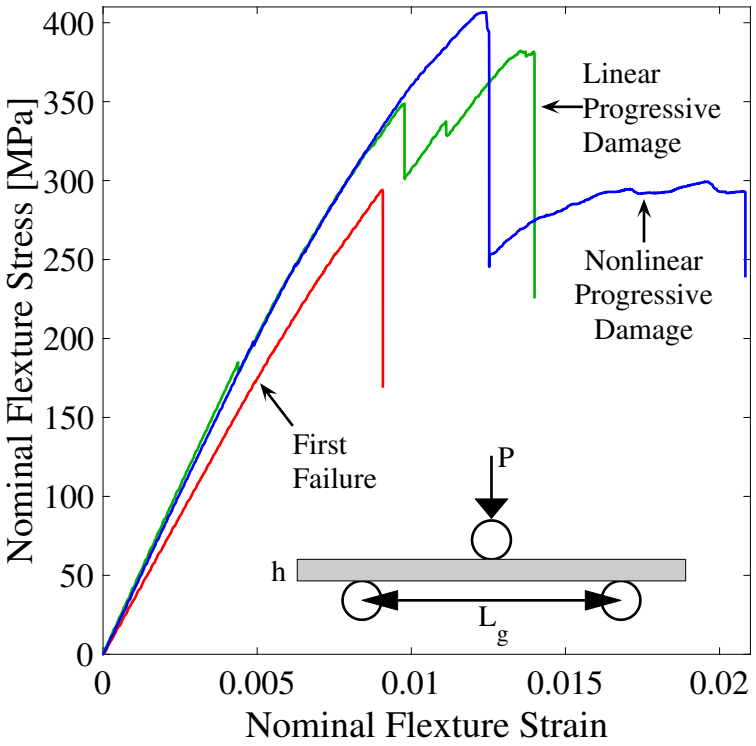

Figure 3.4: Three types of stress vs strain curves that were seen from flexure tests. First there was failure at first onset of fracture (red), linear progressive damage (green), and nonlinear progressive damage (blue).

curves are very different. This shows how the underlying mesostructure of DFCs are very important to understand the failure mechanisms and that this information is needed to fully understand how a specimen is failing. It should also be noted that from the fracture surfaces in fig. 3.5a and b that the fracture path avoids fiber breakage.

When looking at the hybrid specimen's stress-strain curves and fracture surfaces, we can gain insight on the effects that fiber waviness has on the flexure modulus and strength. Figure 3.6 shows the stress-strain curve and the fracture surfaces for the wide and normal hybrid 2 specimen. Here, there are two distinct groups of stress-strain curves. From the fracture surfaces, it can be seen that the higher stiffness group had specimen whose UD fibers were straight, while the lower modulus group had fibers that were wavy. In addition to the stiffness, it can also be seen that the strength of the flexure specimen with straighter fibers was also

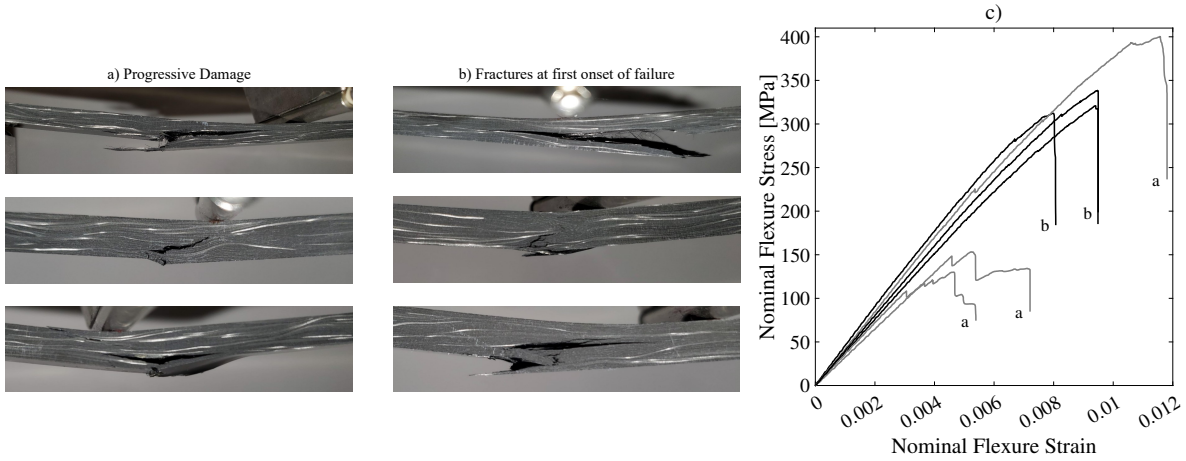

Figure 3.5: Fracture surface and their associated stress vs strain curves show that the two can not be correlated. The fracture surfaces of specimen that exhibited progressive damage and the ones that failed at first onset of failure look similar.

higher than those with wavy ones. This showcases the impact that the waviness of the fiber have on the flexure modulus and strength. On the other hand, the Hybrid 1 specimen has only one group of stress-strain curves, which can be seen in 3.7. This indicates that the period at which the fibers goes from wavy to straight is about 26 mm and that this width is enough to capture the full range of fiber waviness in a Hybrid 1 specimen.

Unlike continuous fiber composites, that always fail at the center of the specimen where the stress is the maximum, some of the DFC and hybrid specimen failed off center. There are weak spots at different locations along the specimen caused by the random nature of the mesostructure of DFCs, which lead to failure occurring off center. Figure 3.8 summarizes the percent of specimen that failed at the center. It can be seen that chip A had a higher chance of failing at the center than chip B. When increasing the thickness of the specimen the amount of center fractures decreases. A similar effect can be seen when increasing the width, however the sample size for the wider specimen is small and the results may change if the same number of specimen were tested as the base geometry. The hybrid specimen have a higher chance of failing at the center, however when the precure routine is introduced, off center fracture becomes more common.

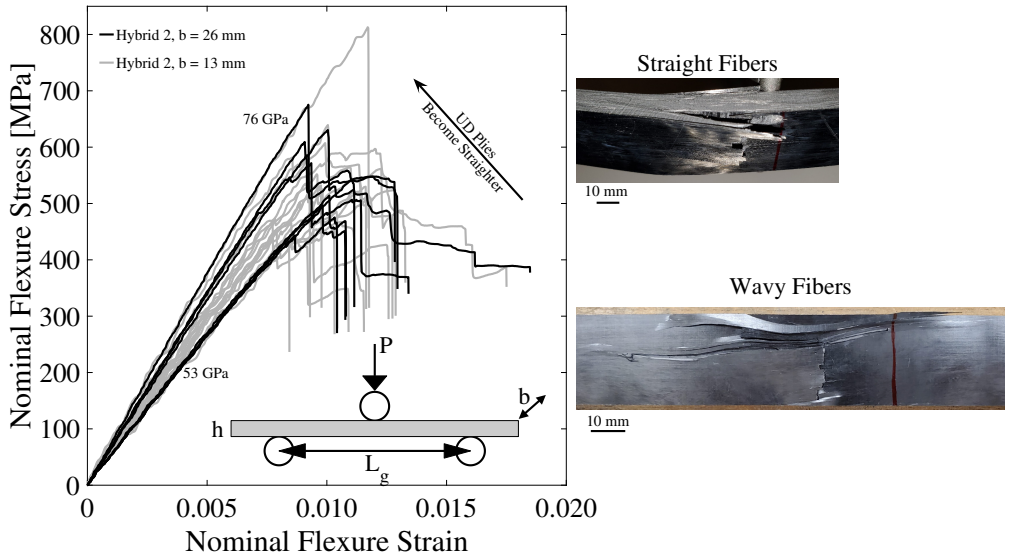

Figure 3.6: Stress vs stain curves of Hybrid 2 and Wide Hybrid 2 specimen. Two distinct groups can be seen and the fracture surface of the Wide specimen with the largest and lowest modulus can be seen on the right. These surfaces show straight fibers for the largest modulus, and wavy fibers for the lowest modulus.

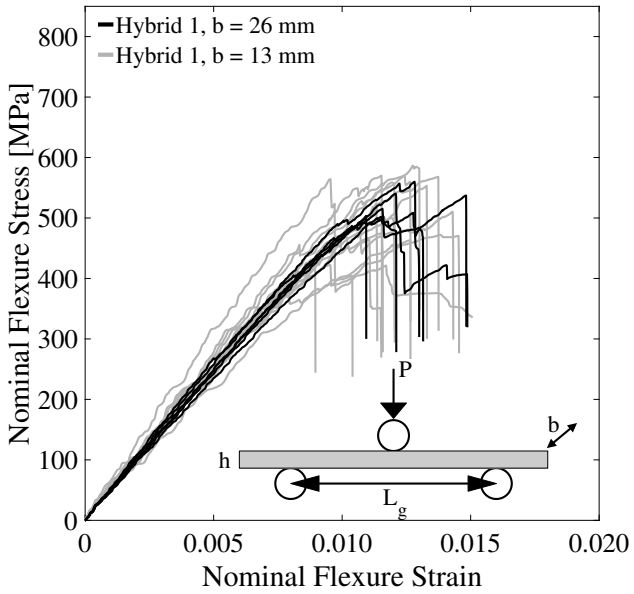

Figure 3.7: Stress vs stain curves of Hybrid 1 and Wide Hybrid 1 specimen.

Figure 3.9 shows some unique notable fractures that occurred. In figure 3.9a, delamination of the continuous fiber plies can be seen. Delamination was most common in the hybrid

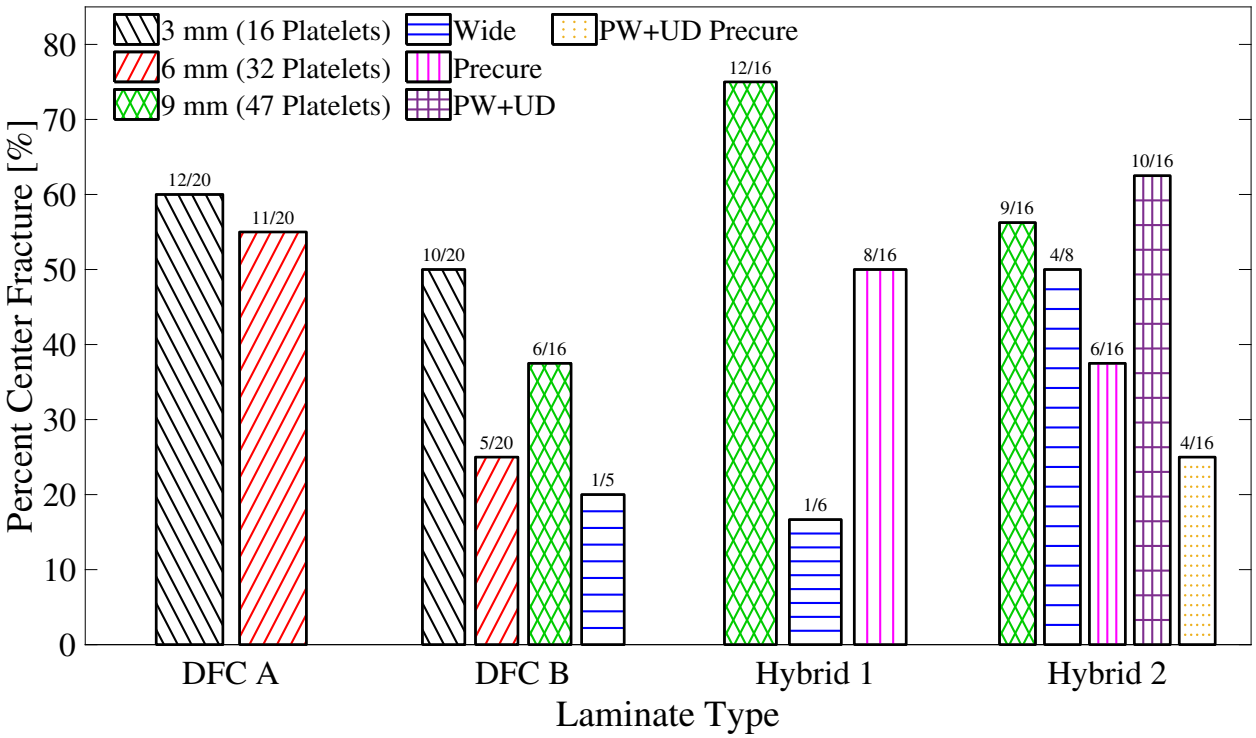

Figure 3.8: Percentage of specimen that failed at the center of the specimen.

2 specimen, occurring 3 times. It also occurred once for the wide hybrid 1, the precured hybrid 2, and the precured woven hybrid specimens. Buckling of the top continuous fiber ply happened in $1-2$ specimens of every hybrid type and once for the 9 mm DFC specimen and can be seen in fig. 3.9b. There were also cases where the bottom ply did not fracture, like in the case seen in fig. 3.9c. When this happened there was significant through thickness damage, delamination, or buckling of the top ply occurred. For the largest thickness, platelet flow becomes much more evident and the out of plane orientation starts to effect the failure. Figure 3.9d shows how the fracture path goes along the platelet bonding and the cracks become vertical. Large out of plane orientations, like the one seen in the figure, were not common, however when they did occur, failure typically happened at these locations.

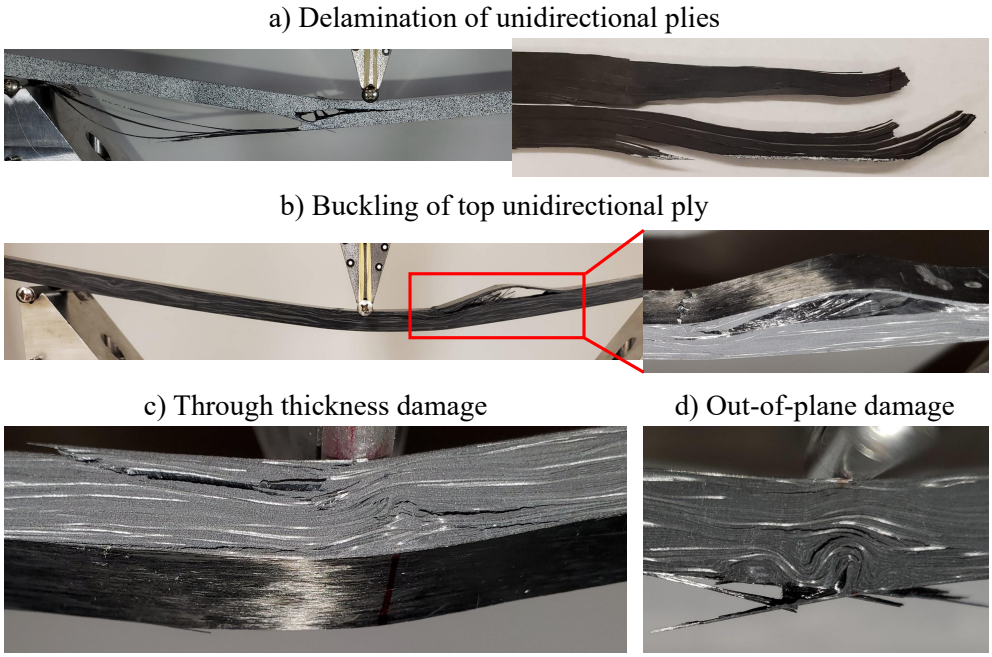

Figure 3.9: Fracture surfaces that show a) delamination of continuous fiber ply, b) buckling of top continuous fiber ply, c) damage through the thickness of the specimen, and d) platelets with high out-of-plane orientation and the damage of such specimen.

Table 3.1: Flexure modulus and strength for DFC and hybrid specimen. The Coefficient of Variation (CoV) is presented in order to compare the variation between laminate types. The three thicknesses correspond to about 16, 32, and 47 platelets through the thickness

Laminate Type	Thickness [mm]	Specimen Tested	Modulus [GPa ± %]	Strength [MPa ± %]
DFC A	3	20	31.86 ± 11.57	233 ± 25.44
DFC A	6	20	34.74 ± 7.63	260 ± 19.15
DFC B	3	20	40.50 ± 23.48	456 ± 25.37
DFC B	6	20	38.00 ± 9.80	296 ± 29.83
DFC B	9	16	39.11 ± 6.11	374 ± 26.13
DFC B Wide	9	5	42.39 ± 7.00	380 ± 25.75
Hybrid 1 UD	9	16	51.12 ± 7.06	524 ± 10.84
Hybrid 1 UD Wide	9	6	50.40 ± 4.20	523 ± 10.87
Hybrid 1 UD Precure	9	16	52.71 ± 5.82	549 ± 10.86
Hybrid 2 UD	9	16	59.96 ± 11.46	552 ± 16.71
Hybrid 2 UD Wide	9	7	61.71 ± 14.63	563 ± 16.38
Hybrid 2 UD Precure	9	16	63.51 ± 5.42	627 ± 9.00
Hybrid 2 PW+UD	9	16	54.25 ± 6.11	559 ± 8.61
Hybrid 2 PW+UD Precure	9	16	54.01 ± 6.00	559 ± 9.10

3.3.2 Flexure modulus

Figure 3.10 and table 3.1 show the flexure modulus of the DFC and hybrid specimen. It can be seen that an increase in platelet length, increases the flexure modulus, but at the same time, increases the Coefficient of Variation (CoV) of the modulus. For the 3 mm specimen, there is a 23.88% difference in the modulus and the CoV is doubled between the two chip sizes. For the 6 mm specimen, there is a 8.96% difference in the modulus and a 24.90%

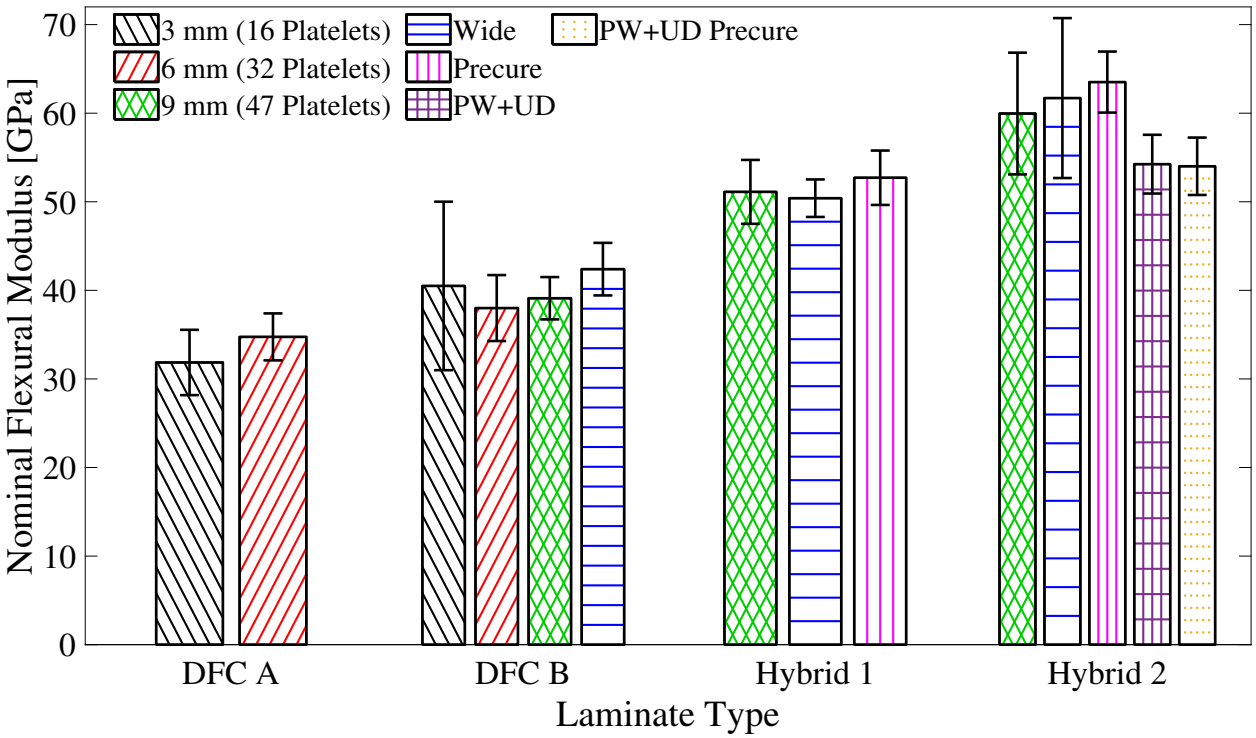

Figure 3.10: Flexure modulus of DFC and hybrid specimen tested.

percent difference in the CoV between the chip sizes. The CoV of the modulus decreased with increasing thickness, and the average modulus had minor changes. For chip A, the CoV decreased from 11.57% to 7.63% when going from 3 mm to 6 mm, and the modulus increased by about 9.06%. For chip B, the CoV decreased from 23.48% to 9.80% when going from 3 mm to 6 mm, and the modulus decreased by about 6.17%. The decrease in CoV for chip B when going from 6 mm to 9 mm is 9.80% to 6.11%, and there was an increase in modulus by about 2.91%. The change in CoV with an increase in thickness was much more pronounced for chip B, and after 6 mm the change in the CoV was much lower. When comparing the wide specimen and the normal specimen, the change in modulus and CoV is small. It should be noted that this may not be the case for other platelet sizes and thicknesses.

It can be seen in fig. 3.10 and table 3.1, that with the addition of the continuous fiber plies, the flexure modulus increases. However, when looking at the UD hybrid specimen,

the effect of the continuous fiber plies had on the CoV was counter to what was expected. It can be seen that the CoV remained the same for the Hybrid 1 specimen, and increased for the Hybrid 2 specimen. When looking at the wide specimen, this increase in CoV was seen in the Hybrid 2 specimen. It is suspected that this change in CoV is caused by the waviness of the UD plies from platelet motion during cure. To inhibit platelet motion during cure, a precure process is done on the DFC core. This process decreased the waviness of the UD plies. It can be seen that this decrease in waviness resulted in a minor increase in the modulus and a significant decrease in the CoV. Another method to decrease the waviness was to have a woven layer between the DFC core and the UD ply. It can be seen that this method also resulted in the decrease in CoV, but the modulus decrease when compared to the UD Hybrid 2 specimen. This is expected since the woven plies have fiber both in the 0° and 90° directions. The precure process was also performed on the woven hybrid specimen and there was no effect on the modulus or the CoV.

When looking at center vs off-center failure, there was no significant difference in the flexure modulus found between laminate types, except for the 3 mm chip B specimen. For this thickness and chip size, the percent difference in the modulus of the specimen that failed in the center to the ones failed off-center was 15.22%. Here the modulus of the center breaks were about 3 GPa lower than the overall average and the off-center was about 3 GPa higher.

3.3.3 Flexure strength

Figure 3.11 and table 3.1 shows the flexure strength of DFC and hybrid specimen. The longer platelets exhibit a higher strength, but at the same time, they also have a higher CoV and as the thickness increases the CoV decreases. This is similar to the trends seen in the modulus. For the 3 mm specimen, the strength is almost doubled when the chip length increases, however the CoV remains the same. For the 6 mm specimen, the difference in strength decreases to be a 12.95% difference when increasing the length of the chip, however the CoV decreased for chip A and increased for chip B. For chip A, the CoV decreased from 25.44% to 19.15% when going from 3 mm to 6 mm, and the strength increased by about

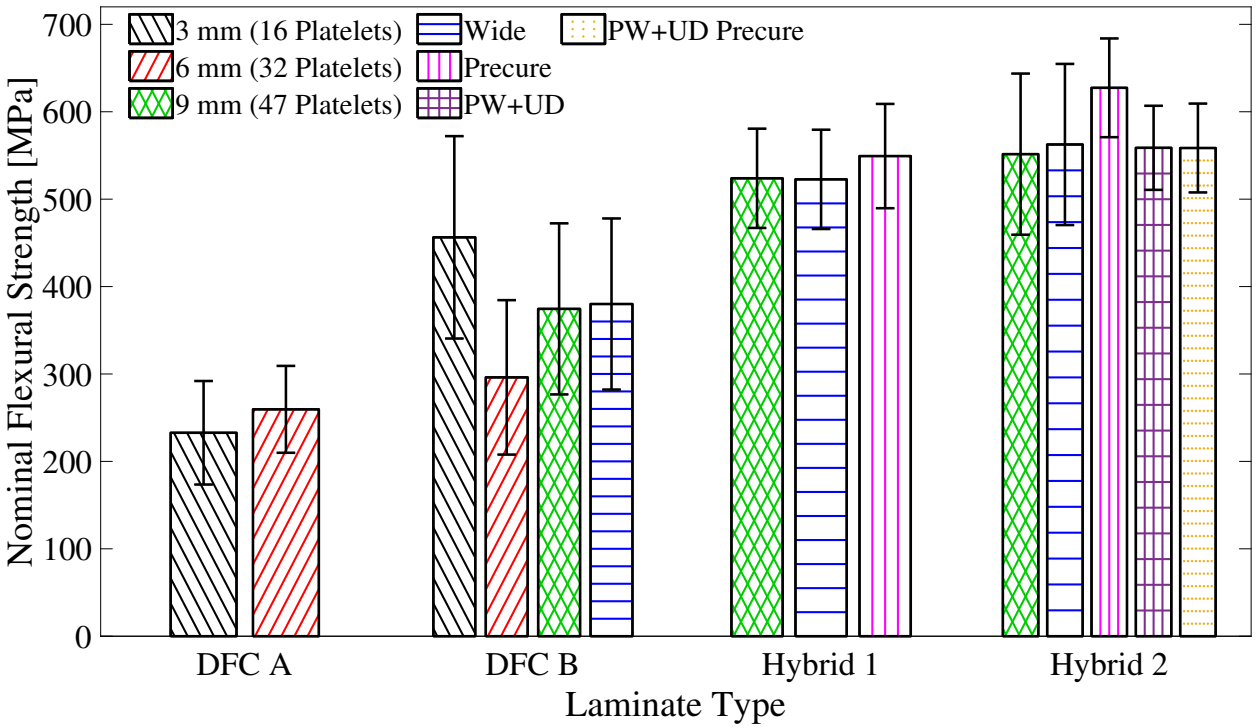

Figure 3.11: Flexural strength of DFC and hybrid specimen tested.

23.18%. For chip B, the CoV had a slight increase from 25.37% to 29.83% when going from 3 mm to 6 mm, and the strength decreased by about 70.18%. The decrease in CoV for chip B when going from 6 mm to 9 mm is 29.83% to 26.13%, and there was an increase in strength by about 52.70%. There was less change in CoV with an increase in thickness in the strength than with the modulus, and chip B had no change. When comparing the wide specimen and the normal specimen, the change in strength and CoV is small. It should be noted that this may not be the case for other platelet sizes and thicknesses. The high CoV of the strength is unacceptable for many applications, especially if we look at at fatigue and the service life, thus hybrid composites should be investigated for use in applications where the strength is of importance.

It can be seen in fig. 3.11 and table 3.1, that with the addition of the continuous fiber plies, the flexure strength increases and the CoV decreases. However, when looking at the

UD hybrid specimen, the effect of the continuous fiber plies had on the CoV was counter to what was expected. It can be seen that the hybrid 1 and hybrid 1 wide have a lower CoV than the hybrid 2 and hybrid 2 wide. It is suspected that this difference in CoV is caused by the waviness of the UD plies from platelet motion during cure. When performing the precure, there was no reduction in the CoV for the hybrid 1 specimen, however the hybrid 2 specimen's CoV decreased significantly from 16% to 9%. For both hybrid types the precure increased the strength by about 9.94% for hybrid 1 and by 22.74% for hybrid 2. When adding a woven fiber plies, the CoV of decreases to be about the same as the precured hybrid 2 specimen, but the strength is about the same as the normal hybrid 2.

When looking at center vs off-center failure, there was no significant difference in the flexure strength found between laminate types, except for the 3 and 9 mm chip B specimen, and the hybrid 2 specimen. The percent difference in the strength of the specimen that failed in the center to the ones failed off-center was 10.14%, 21.24%, and 16.69% for the 3 mm chip B, the 9 mm chip B, and the hybrid 2 specimen respectively.

3.3.4 X-Ray CT scans

Figure 3.12 shows a slice from X-Ray μCT scans of the wide hybrid 2 and the wide 9 mm platelet B specimen. The scans show that the mesostructure of the 9 mm platelet B specimen is impacted by the addition of the UD plies. The Hybrid 2 specimen has significant out-of-plane orientations that make up about 50% the total thickness of the specimen. Whereas the R-DFC specimen has minimal out-of-plane orientations, where at a maximum the out-of-plane angle is through about $4-5$ platelet thicknesses. This shows that adding the continuous fiber plies changes how the platelets flow during the curing process.

3.4 Finite element model

In this study, finite element modeling is used to predict the linear elastic behavior. Due to the inhomogeneous mesostructure of DFCs, the platelet constitutive properties and orientation distribution is very important in order to capture the performance of structures made with

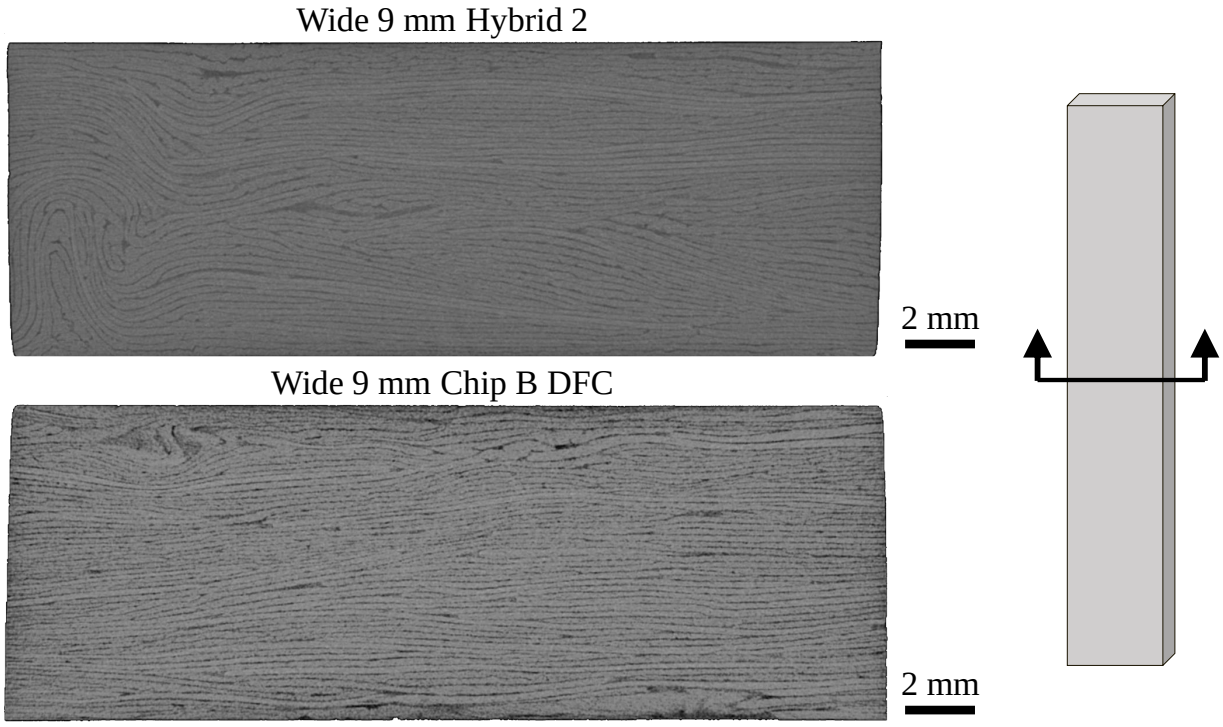

Figure 3.12: X-Ray CT Scan of a wide hybrid 2 and a wide 9 mm platelet B specimen, showing the through thickness (y-z plane) view of the specimens.

this material. Also, the partition size must be sufficiently small in order capture the platelets, but not too small to make the simulations to computationally expensive. In this study, platelets are partitioned into grids of 0.5×0.5 mm.

3.4.1 Orientation distribution

In order to model DFCs, the underlying orientation needs to be captured. It was found in [29–33,105] that to capture the variation in mechanical properties seen in experiments, the variation of the average orientation tensor between specimen is needed. In order to control the orientation, the cumulative distribution function of the second-order orientation tensor, a_{ij}, [106] is either calibrate, or the actual distribution is found using optical microscopy [107] or X-Ray CT scanning [29–31,105]. The use of optical microscopy and X-Ray CT scanning to find

the actual distribution is expensive and time consuming, so the distribution is calibrated. In this study is is assumed that the out-of-plane orientation is negligible, thus the second-order orientation tensor only has one component of importance, a_{11}. The probability distribution used is the Normal Distribution, and the average and standard deviation of a_{11} is calibrated to match the average and CoV of the flexure modulus found from experiments. To ensure that the a_{11} values picked are random and have no bias, the Latin Hypercube sampling method is used. The cumulative distribution function is split into $n \times m$ section, where n is the number of specimen that will be simulated and m is the number of representative volume elements (RVEs) in one coupon. A random orientation from a random section is picked for each RVE in a specimen. By doing this the whole distribution is covered and the average and the standard deviation is preserved.

As a starting point, $a_{11} = 0.5$ and a CoV of 10% is used, 30 specimens are simulated, and the RVEs are taken to have a length of 24 mm. An RVE is only taken to be in the gauge area of the specimen and the orientation tensor used for the over hang is taken to be the orientation tensor of the adjacent RVE, since the overhang has little to no effect on the performance in flexure. Orientation calibration for platelet B with a thickness of 3 mm can be seen in fig. 3.13. Using the starting a_{11} and CoV results in an average modulus of 37.60 MPa and a CoV of 13.75%, which has a percent difference to the experimental average and CoV of 7.43% and 52.27% respectively. When increasing the orientation CoV from 10% to 15% the CoV of the modulus found through simulations become closer, having a percent difference of 24.52%, however the average modulus becomes farther, having an increase in the percent difference to 10.21%. To match the experimental average modulus and its CoV, the orientation average and CoV used for the mesostructure must both be increased. The average a_{11} is increased to 0.52 and the CoV was increased to 20% and 25%. By doing this the the average became close having a percent difference of 3.48% and 7.35% respectively, while the CoV had a percent difference of about $\pm 20\%$ for both cases. Next the midpoint of the CoV, 22.5%, is used. Using $a_{11} = 0.52 \pm 22.5\%$ resulted in a perfect match, where the average modulus had a percent difference of 1.08% and the CoV had a percent difference of

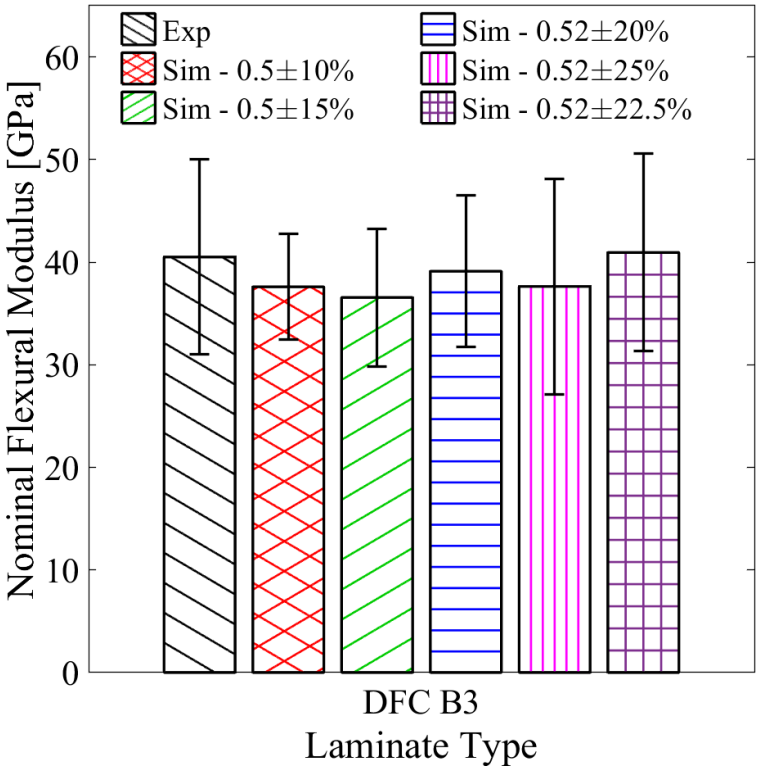

Figure 3.13: Results of orientation calibration

0.01%. Similar calibrations were done for the other platelet sizes and thicknesses, and the final orientations used can be seen in table 3.2.

From experiments it was seen that the fiber waviness plays a huge role in the average modulus and its CoV. To capture this effect in the model, a function of the fiber waviness needs to be found. The wave function of the 345×13 or 345×26 mm specimen is extremely hard to determine. One option of finding the waviness is by using X-Ray CT scanning, however this method is impractical for two reasons. The first is the size of the specimen and the second is the specimen geometry. For a long specimen, multiple scans are needed to capture the orientation, this would be expensive and time consuming. Also, since the continuous fibers are at the surface it is hard to get a good view of them due to the surface effects of the X-Rays. Long flat surfaces are really good at reflecting X-rays which causes the volume close to the surface to lack the detail needed to find the orientation. This can be fixed in many ways, such as using a higher resolution or by increasing the frames averaged which

Table 3.2: A_{11} and CoV used for mesostructure generation.

Laminate Type	Thickness [mm]	A_{11}	CoV [%]
DFC A	3	0.45	10
DFC A	6	0.50	10
DFC B	3	0.52	22.5
DFC B	6	0.50	10
DFC B	9	0.50	5
DFC B Wide	9	0.50	5
Hybrid 1 UD	9	0.45	10
Hybrid 1 UD Wide	9	0.45	10
Hybrid 1 UD Precure	9	0.45	10
Hybrid 2 UD	9	0.45	10
Hybrid 2 UD Wide	9	0.45	10
Hybrid 2 UD Precure	9	0.45	10
Hybrid 2 PW+UD	9	0.45	10
Hybrid 2 PW+UD Precure	9	0.45	10

helps with noise reduction, however both these methods results in longer scans and would be too expensive and time consuming. Another option is to perform microscopy, however this process is more time consuming than X-Ray CT scanning. So, in this study, the fracture surface is visually inspected and an estimation on the waviness is done. The wave functions are made using the largest fiber angle found and period of the wave is estimated from that fracture surface. When looking at the fracture surfaces, the largest angle of the fibers was 12° and a quarter of a period was about 51 mm, and the amplitude was about 8 mm, this can be seen in fig. 3.14. As an approximation of the waviness, a sine was used as a base. It is evident from testing the wide specimen that there is a gradient in the waviness, this can be seen from the wavy fiber fracture surface in fig. 3.6. Figure 3.15 shows the fiber paths used

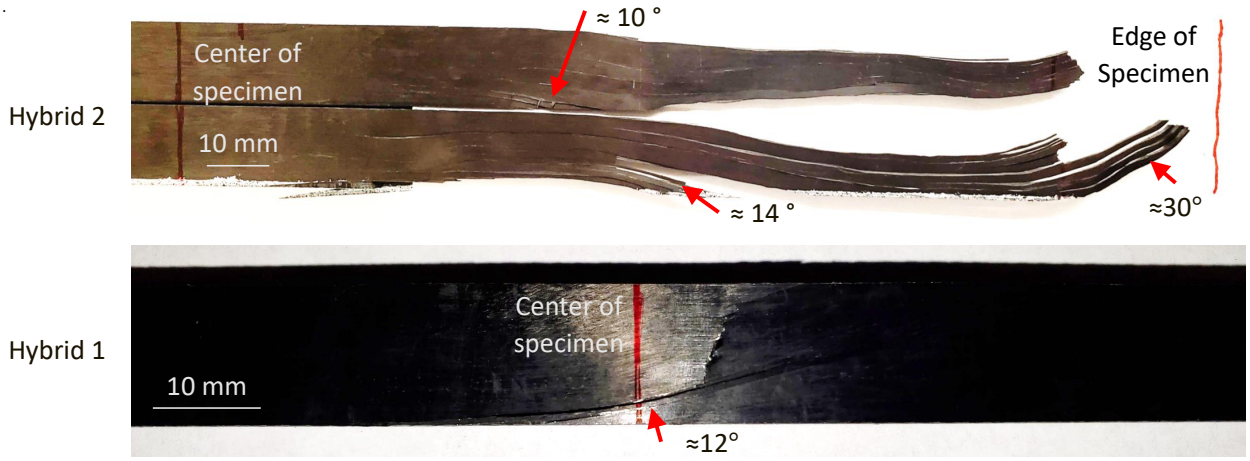

Figure 3.14: Fracture surfaces of hybrid 1 and 2 specimen exhibiting fiber waviness.

in the simulations with the probability distributions of the orientations of the fiber path. The areas in red are used for the Hybrid 2 specimen, where as the blue sections are used for the Hybrid 1. The sections are chosen in this way because when examining the stress vs strain curves of the hybrid specimen, the Hybrid 2 specimen have two distinct groups of stiffer straight UD plies and less stiff wavy UD plies, where as the Hybrid 1 specimen only have one group in the stress vs strain curves.

3.4.2 Mesostructure generation

Once the target orientations are found the mesostructure can be generated. The generation used in this work is an extension of the stochastic laminate analogy method proposed in [71–73]. A brief summary of the generation algorithm is provided here, and more details on the algorithm and its implementation can be found in [108]. The generation is split into two parts, the first is the platelet distribution, and the second is a thickness adjustment. The platelet spatial distribution is assumed to be perfectly random with a uniform distribution, and the orientation distribution is assumed to have a uniform distribution where the bounds are adjusted to obtain the target a_{11}. By using the cure ply thickness from the material data sheet and the final laminate thickness measured we get an estimate of how many platelets there are through the thickness. This number is used as an input parameter. The CoV of

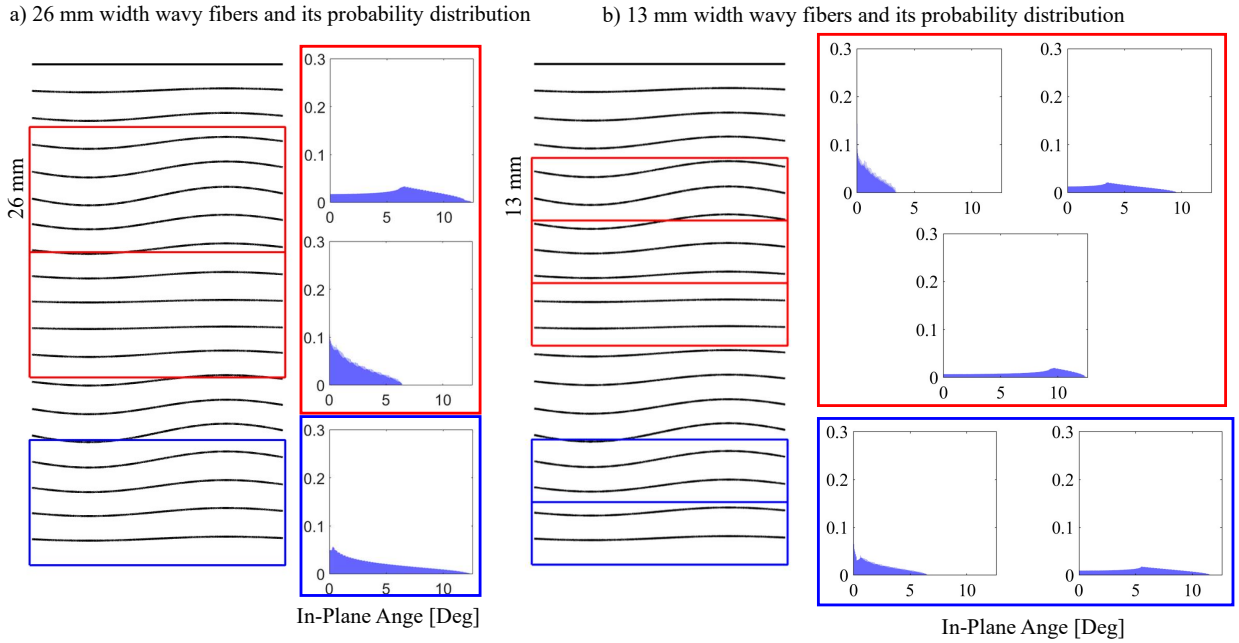

Figure 3.15: Example of wavy fibers used in the simulations with the probability distribution of the in-plane orientations. The Hybrid 2 specimen uses the orientations in the sections in red, while the Hybrid 1 specimen uses the ones in blue.

the number of platelets through the thickness is assumed to be similar to that of previous works [22, 108]. To achieve average number of platelets and CoV, saturation points and platelet limits are used to guide generation. Saturation points are set to be every three layers and the average number of platelets through the thickness must equal the current saturation point before moving on to the next saturation point. At any point on the generated laminate, the number of platelets can not exceed the platelet limit. If this set is not implemented there would be a high concentration of platelets in some areas, leading to the saturation point being met, but there would be large areas of little to no platelets. These limits are set to be the saturation point times the CoV. After the average number of platelets is met a thickness adjustment is performed and resin is added to areas where there is less platelets than the average. If the number of platelets is greater than or equal to the target number, the platelets' thickness is evenly distributed through the thickness. Once the sum thicknesses of all the elements in one partition equals the target thickness a splitting is performed to match the

maximum number of plies one partition has. The element to be split is selected at random.

Once the mesostructure is generated it is imported into Abaqus/Standard, except for the wide specimen which needs to be simulated in Abaqus/Explicit [76]. The layers of platelets and resin are kept as DFC plies, and 4-node, quadrilateral Belytschko-Tsay shell element with reduced integration (S4R) are used to model them. To model the inter-ply bonding, 8-node 3D cohesive elements are used. The pins are modeled as 4-node, bilinear quadrilateral rigid elements (R3D4) and have a radius of 5 mm. From a parametric study it was found that the change in flexure modulus using a friction coefficient of 0.05 increases by 1.49% when increasing the friction coefficient to 0.3. Thus, for linear elastic simulation the friction coefficient does not play a big role and in this study a friction coefficient of 0.1 is used. The displacement applied is such that the final nominal flexural strain is 0.0001. Table 3.3 and 3.4 state the linear elastic properties for T800S, T650 PW, the resin, and the cohesive elements.

Table 3.3: Elastic properties of platelets and resin used in the stochastic finite element model.

Description	T800S	T650 PW	Resin
Thickness, t [mm]	0.191	0.196	varies
In-plane longitudinal modulus, E_1 [GPa]	148	69.09	3
In-plane transverse modulus, E_2 [GPa]	8.3	68.26	3
In-plane shear modulus, G_{12} [GPa]	3.93	5.58	1.1
In-plane Poisson ratio, ν_{12}, ν_{31}	0.33	0.048	0.35

Table 3.4: Elastic properties of the cohesive elements used in the stochastic finite element model.

Thickness [μm]	E_{nn} [kN/mm^3]	E_{ss} [kN/mm^3]	E_{tt} [kN/mm^3]
1	10	3.7	3.7

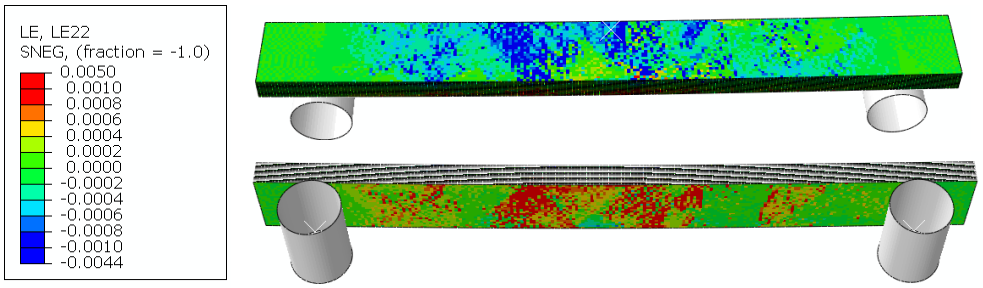

Figure 3.16: Axial strain on the top and bottom surfaces of Chip B 3 mm specimen from simulations.

3.4.3 Results of finite element simulations

Figure 3.16 shows the axial strain on the top and bottom surfaces a 3 mm Chip B specimen. The overhang of the specimen exhibits little to no axis strain, showing that the assumption that the orientation of the overhang has no effects on the overall flexure properties is valid. For conventional materials, the top surface would be in compression and the bottom in tension, however this is not the case for DFCs. Figure 3.16 has areas of tension on the top surface and compression on the bottom surface which is caused by the inhomogeneous mesostructure of the material.

Figure 3.17 shows that all normal DFC simulations match the experimental modulus and CoV well. The specimen with the largest percent difference is the Chip B 9 mm thickness specimen, with an difference of 4.70%. The CoV was also captured well, with the largest difference being Chip A 3 mm thickness which underpredicted the CoV by 2.29 percentile points. On the other hand only the Hybrid 1 simulations match the experiments, with the percent difference of the averages of the Hybrid 1 and Hybrid 1 PC specimen being 6.79% and 6.81% respectively. The CoV of the Hybrid 1 and Hybrid 1 PC is underpredicted by 4.36 and 2.95 percentile points respectively. The reason the Hybrid 2 specimen are not matching the experimental values is due to the fact that the platelet generation assumes that the platelets are planar and has no significant out-of-plane orientations. From X-Ray CT results in Section 3.3.4, it can be seen that this is not the case here. This is a limitation in the

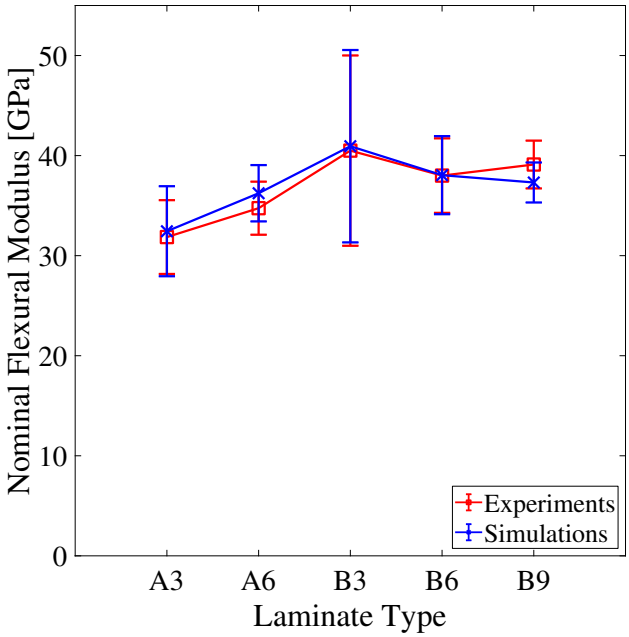

Figure 3.17: Nominal flexural modulus of DFC specimen found through experiments and simulations.

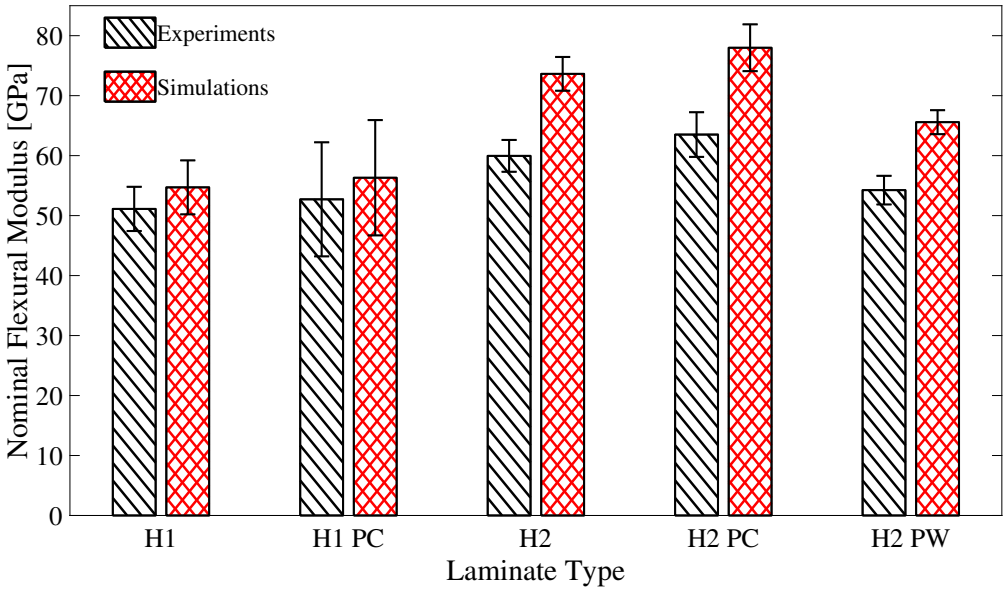

Figure 3.18: Nominal flexural modulus of hybrid specimen found through experiments and simulations.

current model and the cause of the overprediction of the modulus.

3.5 Discussion

The platelet size and thickness of the specimen had a large impact on the flexure modulus and strength. The effects on the flexure properties have been seen in previous studies using pristine prepreg by [28, 99, 101] and with other mechanical and fracture properties by [10, 12, 28, 34, 35, 38, 85, 86]. These studies also found similar fracture surfaces that were seen in this study. When the length of the platelet increased, so did the modulus, strength, and their CoV. When the thickness increased the modulus and strength of chip A specimen increased, and the CoV decreased. For chip B, the modulus and strength CoV remained the same with an increase in thickness, the modulus CoV decreased, and the strength decreased then increased. When the flexure specimen fractured, they tended to avoid fiber breakage and failed at the platelet-to-platelet interface, platelet boundaries, and along the fibers within a platelet.

For the hybrid specimen made with UD plies, platelet motion during cure has a huge impact on the the flexure modulus, strength, and their CoV. This waviness resulted in the CoV of the flexure modulus being higher than that of a purely DFC specimen. It was thought that with less randomness at the out plies, where the flexure properties have the most dependence on, the CoV would decrease drastically, however the CoV increased for both hybrid 1 and 2 specimen. A similar trend was found by Corbridge et al. [38], if the UD were transverse of the flow, the CoV of the flexure modulus did not change. Then by introducing a precure routine or by using cross ply rather than a UD layup the CoV decreased to about half of its original value. However, Corbridge et al. only found the flexure modulus and not the strength. In this study the effects the waviness has on the strength is also found. The waviness causes the strength to have a higher CoV and lower strength than if the plies were straight. To get straight fiber, a precure routine, like done here and by Corbridge et al., or by adding fibers along the direction of flow, in this study the direction of flow was in all directions thus a woven ply was used. However, as seen by Corbridge et al., the precure lowers ILSS and may not be acceptable in applications where this a concern. In these cases

using a woven fiber ply between the DFC and UD plies would a great solution.

For DFC and hybrid specimen it can be seen that the random nature of the mesostructure leads to failure away from the center of the specimen, which does not occur for continuous fiber composites. The specimen that failed at the center or off-center had no difference in their modulus except for the 3 mm chip B specimen. Here, the modulus was stiffer when failure occurred off center. It is suspected that this is caused by the length of the platelet relative to the size of the specimen. Chip B has a length of 30 mm which takes up 31% of the gauge area. It was sen here and in previous studies [10,12,28,85,86] that when failure occurs, the fracture follows the path of least resistance, avoiding fiber breakage and going along the boundaries of platelets. When a platelet is in a favorable orientation and if the platelet is centered, the edge of the platelet will be about a third the distance to the support pin thus failure would occur off center. However the width of the platelet is 9.5 mm, so if the orientation is unfavorable, the platelet could fail at the edge of the platelet or between fiber and would be considered a center failure. Also since 3 mm is about 16 plies, the outer plies have a much stronger impact on the modulus than the 6 or 9 mm specimen. This is analogous to continuous fiber plies where, as the thickness goes to infinity, the flexure modulus approaches the tensile modulus, and when the thickness is small the stacking sequence has a huge impact on the flexure modulus where there can be a percent difference of $\pm 60\%$ between the tensile and flexure modulus.

A difference in strength was also seen between the center and off-center failures for the 3 and 9 mm chip B specimen, and the hybrid 2 specimen. For the 3 mm specimen the strength was lower when failure occurred at the center. The reason for this is the same as the one stated for the modulus. The strength of the 9 mm DFC and the hybrid 2 specimens were stronger at the center of the specimen. It is suspected that the cause of this is the out-of-plane rotations that occurred in the specimens with 9 mm thickness. Also, as can be seen in fig. 3.9a, for the hybrid 2 specimen, the waviness of the UD plies are much more significant at the ends of the specimen. Both the these factors would contribute the areas further from the center being weaker and failing before the center of the specimen reach the

maximum load it can carry. These off center failures would not occur with continuous fiber laminates who are homogeneous through the length. These failures are unique to DFCs and other inhomogeneous materials.

It was also seen in fig. 3.8 that center failure became less frequent when the precure routine was introduced. This could be caused by the fact that the precure routine acts closer to co-bonding rather than co-curing. Co-bonding would result in less efficient transfer of stress between the DFC core and the continuous fiber plies. Corbridge et al. [38] performed a similar precure routine which they call "resin staging" on a DFC hybrid where 3 UD plies are added on top of the DFC core. They found that the flexure modulus did not have any significant changes with resin staging, however the Inter-Laminar Shear Strength (ILSS) decreased with increased resin staging. In their case the hybrid layup was not symmetric so the center line of the bonding between the DFC and the UD plies was at the center of the specimen. This leads to the maximum shear stress being at the bonding. In the case presented in this study, the specimen have a much larger thickness and span to thickness ratio than that of an short beam shear specimen, meaning the continuous fiber plies are at the surface and would experience much less shear at the bonding point. This could be why the flexure strength is not decreasing due to the co-bonding, however the failure location changes.

3.6 Conclusions

This work investigated the effects of platelet size, coupon thickness, and the addition of continuous fiber plies on the flexure properties of Discontinuous Fiber Composites (DFCs) made using repurposed of thermoset prepreg material. Two platelet sizes were tested, 12×9.5 mm, and 30×9.5 mm. Thicknesses of 3, and 6 mm (roughly 16 and 32 platelets through thickness respectively) were investigated for both platelet sizes, and an additional thickness 9 mm (roughly 47 platelets through thickness) was also investigated for the larger platelet. Additionally hybrid specimen with continuous fiber plies on the outer surface of a DFC core was tested. These specimen used unidirectional (UD) and woven (PW) fibers, and a precure

routine was performed to limit platelet motion during cure. Based on this study the following conclusions can be drawn:

1. As the platelet length increases, so does the flexure modulus and strength, however the Coefficient of Variation (CoV) also increases. When the platelet length increased by 150%, the modulus increased by 27% and the strength increased by 96% for the 3 mm specimen. The modulus also increased by 9% and the strength increased by 14% for the 6 mm specimen. However, the CoV of the modulus increased by 103% and the CoV of the strength did not change for the 3 mm specimen. The CoV of the modulus for the 6 mm specimen increased by by 28% and the CoV of the strength increased by 56%.

2. For the smaller platelet size (12×9.5 mm), as the thickness increases from 3 to 6 mm, the flexure modulus remains the same and there is a slight increase in the flexure strength. At the same time the CoV decreases by 34% and 25% for the modulus and strength respectively.

3. For the larger platelet size (30×9.5 mm), as the thickness increases the modulus remains the same. At the same time, the CoV decreases by 58% when going from 3 to 6 mm and by 38% when going from 6 to 9 mm. However, the strength decreases when going from 3 to 6 mm, then increases when going from 6 to 9 mm. At the same time, the CoV of the strength remains the same.

4. In this study $1 - 2$ plies where continuous fiber plies were added to the outer surfaces of a DFC core to make a hybrid laminate. This makes up 4 or 8% of the layup. Adding continuous fiber plies increases the flexure modulus and strength, however due to waviness caused by motion during curing, the CoV does not decrease. By performing a precure routine or by adding woven fiber plies between the DFC core and the unidirectional (UD) ply, the waviness is mitigated and the CoV is reduced.

5. Due to DFCs' random mesostructure, failure can occur off center, which does not happen with continuous fiber composites. Typically, the failure location did not effect the flexure properties, except for when the platelet made up a significant portion of the gauge area, when out-of-plane rotation, or when the hybrid layup has significant waviness in the UD plies.

6. The precure routine changes the bonding between the DFC core and continuous fiber plies to be co-bonded rather than co-cured. This had no effect on the flexure properties and only caused failure to be more common off center.

7. Computational models were able to match the experimental modulus and its CoV for all DFC specimen. However, the assumptions made for the model results in the hybrid simulations not perfectly matching. The most likely causes of this is, not matching fiber waviness, out-of-plane rotations of the platelets, and poor bonding between the DFC core and the UD plies. Microscopy is currently being performed on a few specimen to determine which of these are viable causes.

8. Work done here shows the immense potential DFCs have to reuse out-of-spec or scrap thermoset prepregs. By changing the platelet geometry, thickness, and by adding continuous fiber plies, one can design a part to have their desired mechanical properties. DFCs also allows for manufacturing of complex geometries, so secondary structural components can be made using reused prepreg.

Chapter 4

COMPUTATIONAL INVESTIGATION INTO THE EFFECTS OF PLATELET SIZE AND FLOW ON THE TENSILE PROPERTIES OF DISCONTINUOUS FIBER COMPOSITES

4.1 Introduction

One of the advantages that Discontinuous Fiber Composites have over conventional continuous fiber composites is their manufacturability. The platelets that make up DFCs allows for complex parts to be made using compression or injection molding. However, one draw back of this is the complexity of the mesostructure caused by flow. When dealing with complex geometries there will be areas of low and high flow, which will cause a biased orientation of the platelets at various points in the structure. These effects need to be captured through predictive models to reduce the number of physical tests needed when certifying parts made using DFCs.

There has been limited research into the effects biased orientations caused by platelet flow on DFCs [31, 38, 109]. Evans et al. [109] investigated flow effects on tensile properties of DFCs with varying fiber lengths. To induce flow they filled the mold with 50%, 75%, and 100% charge coverage. They found that the ratio between the longitudinal and transverse tensile properties increased with the lower charge coverage (higher flow). Additionally, they found that shorter fibers tended to have more fiber alignment at the lower charge coverage. They also saw that lower charge coverage induced higher levels of out-of-plane orientations. Corbridge et al. [38] investigated the flexure modulus and Interlaminar Shear Strength (ILSS) of DFCs and hybrid laminates, where three layers of unidirectional (UD) plies were added on top of two layers of DFC plies. They induced platelet flow by filling a third of the mold on two sides. This makes the platelets only flow to the center while keeping the applied pressure

balanced. They found that the flexure modulus of DFCs was higher when the flow was aligned with the length of the specimen. This is also true for when the UD plies were along the direction of flow. When the UD plies were transverse to the flow direction, the modulus became similar of the 100% DFC laminate with flow along the length of the specimen. They also found that the ILSS was higher for the hybrid than the DFC laminates. Due to the flow of the platelets there was a lot of rotation and translations of the UD fibers. This was seen by placing a uniform grid on the UD ply before curing. They saw that there were rotations as high as 30° and the original length of the grid was stretched and compressed by as much as $1.5 - 0.8$ times the original length. To mitigate this a precure routine was introduced, which kept the UD fibers straight, but decreased the ILSS. Sommer et al. [31] investigated the effects of flow on tensile properties of DFCs. Flow was induced by using a 40% charge coverage of the mold. They found that the flow aligned the fibers with the direction of flow which increase the tensile properties longitudinal to the flow and decreased the properties transverse to the flow, when compared with specimen that had no flow.

By using orientation data obtained from X-Ray CT scans, a statistical study is performed to help guide the mesostructure generation used for simulations. The mesostructure generation algorithm developed by Ko et al. [35] is modified to use the Cumulative Density Function (CDF) of the orientations found from the X-Ray CT scans. In addition to this, the CT data is used to make a one to one copy of the specimen and is then simulated. The results form the simulations will also be compared with experimental data. All specimen tested were manufacture by Sekisui Aerospace [98].

4.2 Materials and testing methods

4.2.1 Material preparation

In this study, two manufacturing processes are performed to make low-flow and high-flow DFC specimens. The low-flow specimens are made by filling a square mold completely, thus little flow of the platelet will occur during the compression molding process. The resulting

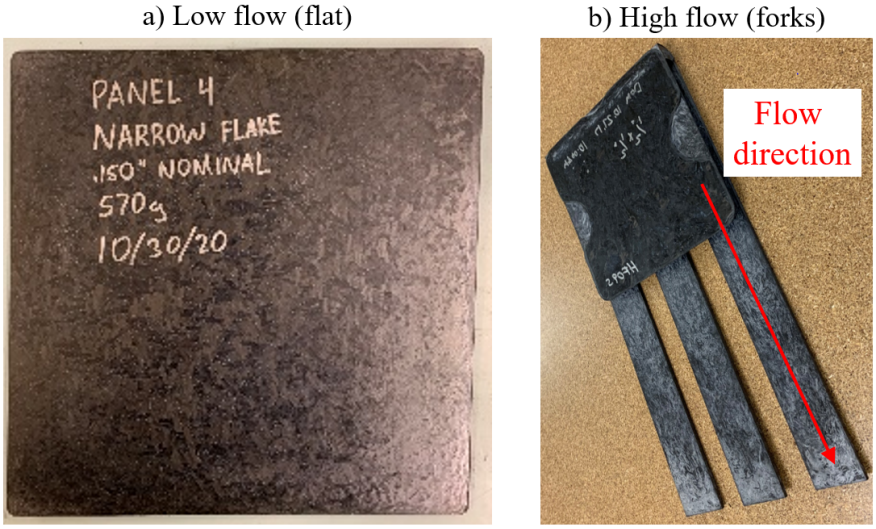

Figure 4.1: Examples of a) low-flow laminate, and b) hihg-flow laminate.

laminate can be seen in Figure 4.1a. From the low-flow laminate, 12.7 mm is trimmed from the edges and tensile coupons are obtained using a wet tile saw with a diamond coated blade. For the high-flow case, a mold with three outlets is filled with platelets, which, when compressed, will result in the platelets filling into the three cavities. The result of this process can be seen in Figure 4.1b. Tensile coupons of the same size as the low-flow specimen are cut from the "fork." All laminates used in this study are made by Sekisui Aerospace [98] using AS4D/PEKK thermoplastic tape from Solvay. Two platelet sizes are investigated, a square platelets, 12.7 mm $\times$12.7 mm, and a narrow platelet with a significantly reduced width. The exact width can not be disclosed due to intellectual property issues.

4.2.2 Mechanical tests

4.2.2.1 Data acquisition

Tests were performed using an Instron 5585H 250 kN electro-mechanical load frame with an Interface 1210ACK-50kN-B load cell. The load cell recorded with a sampling frequency of 10 Hz while Digital Image Correlation (DIC) was used to obtain the strain values needed. Images were captured using a Nikon D5600 DSLR camera with Nikon AF micro 200 mm

and Sigma 135 mm DG HSM lenses with a sampling rate of 1 Hz. GOM Correlate [52] was used to process the photos and obtain the strain values.

4.2.2.2 Tension

Tensile tests were performed based on ASTM D3039 [53]. Specimens were made to have a width of 25.4 mm and a gauge length of 153 mm. The tabs were made with 3.175 mm (1/8 in.) thick garolite and JB-Weld Cold Weld Steel Reinforced Epoxy and had a length of 55 mm with a bevel of 8°. A displacement rate of 2 mm/min was maintained for all the tests. In total, 30 low-flow and 12 high-flow specimens of each platelet type were tested.

4.2.3 X-Ray micro-computed tomography

Prior to testing, X-Ray micro-computed tomography (μCT) was performed on 5 coupons of each type, except for the narrow platelet low-flow specimen where only 3 coupons were scanned. X-Ray CT scans were performed using a North Star Imaging X5000 [104] and scans with a voxel size of about 26 µm were obtained. These scans are analyzed using an in-house code which uses a 3D Gaussian distribution derivative filter to find the local density gradients and reduce noise [110]. The probability distribution of orientations is then used as an input to a mesostructure generation algorithm to recreate coupons with the same orientations as the ones scanned.

4.3 Experimental results

4.3.1 Tensile tests

The flow effect on the tensile modulus and strength of narrow and square platelet DFC coupons can be seen in Figure 4.2 and Table 4.2. The results of the experiments have been normalized to the theoretical quasi-isotropic laminate properties calculated using Classical Laminate Theory and Tsai-Hill failure criterion. When looking at the platelet size effect, the narrow platelet consistently out performers the square platelet specimen. The percent

difference of the low-flow modulus and strength between the two platelets are 7.61% and 20.44% respectively. Whereas, the percent difference of the high-flow modulus and strength between the two platelets are 2.90% and 2.65% respectively. The flow effects the tensile properties of the square platelets more strongly than the narrow. For the narrow platelets, there is a percent difference of 11% and 4% when going from low- to high- flow for the modulus and strength respectively. This is an increase in the modulus from 0.90 to 1.04 and an decrease in strength from 0.40 to 0.39. The increase in modulus is due to the flow reorienting platelets into the loading direction. There is no change in the strength due to void formation, which can be seen in section 4.3.2. For the modulus, the Coefficient of Variation (CoV) decreases from 12.71% to 8.32% when going from low- to high-flow, and CoV of the strength decreases from 14.16% to 9.35%. For the square platelets, there is a percent difference of 22% and 10% when going from low- to high-flow for the modulus and strength respectively. This is an increase in the modulus from 0.82 to 1.01 and an increase in strength from 0.33 to 0.38. These increases in the mechanical performances are caused by the flow realigning the platelets into the loading direction. Now that there are more fibers in the loading direction, the specimen becomes stiffer and stronger. The effects of flow on the variation are inconclusive. For the modulus, the Coefficient of Variation (CoV) decreases from 7.04% to 5.41% when going from low- to high-flow. However, the CoV of strength increases from 8.75% to 12.98%.

Table 4.1: Tensile properties of narrow and square platelet, low- and high-flow specimen. Results are normalized to the quasi-isotropic properties.

	Narrow Low	Narrow High	Square Low	Square High
Modulus [E/E_{QI}] (%)	0.90 ± 12.71	1.04 ± 8.32	0.83 ± 7.00	1.01 ± 5.41
Strength [σ/σ_{QI}] (%)	0.40 ± 14.16	0.39 ± 9.35	0.33 ± 8.75	0.38 ± 12.98

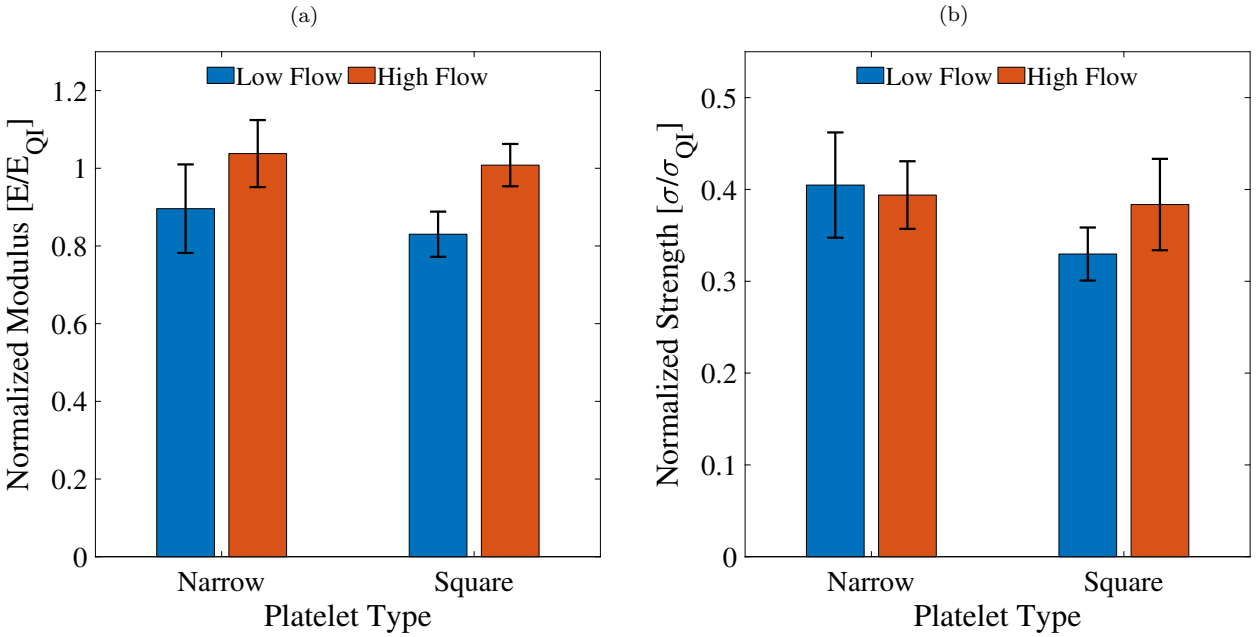

Figure 4.2: Normalized tensile modulus and strength of low-flow and high-flow narrow and square platelet DFC specimen

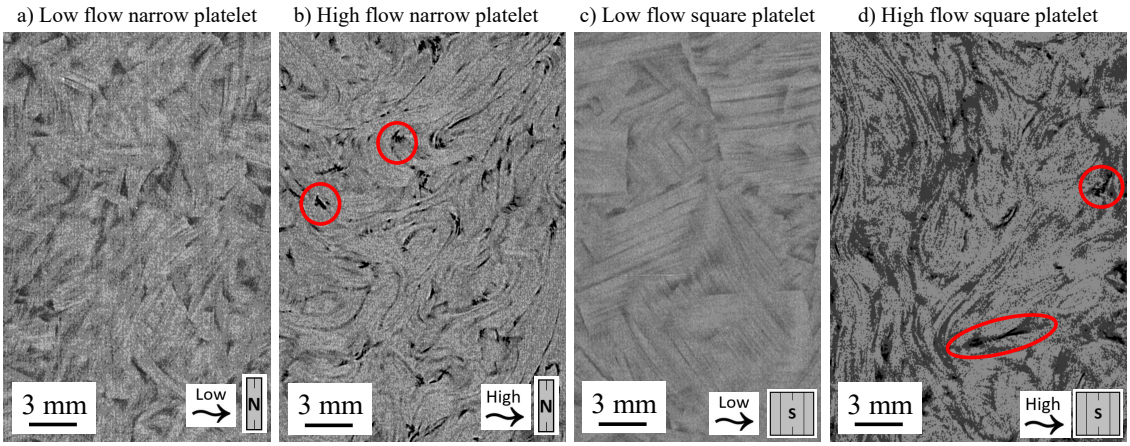

Figure 4.3: Cross section of DFC coupons showing voids in the high flow coupons.

4.3.2 X-Ray μCT

4.3.2.1 Void Content

Figure 4.3 shows a cross section from one scan of each type. A larger number of voids can be seen in the high-flow specimen, while little to no voids can be seen in the low-flow ones. The red circles in Fig. 4.3b and d are dark spots resulting from voids in the coupon. The void content calculated from the scans can be seen in Fig. 4.4. The low-flow narrow platelet specimen have a void content of $0.08\% \pm 0.13\%$ and the void content of high-flow coupons are $1.39\% \pm 0.11\%$. The low-flow square platelet specimen have a void content of $0.12\% \pm 0.07\%$ and the void content of high-flow coupons are $1.29\% \pm 0.16\%$. This increase in void content due to flow could be the reason for the increase in strength not being as pronounced as the increase in modulus.

In addition to the increase in voids between flow conditions, it is observed that there is a change in void content between the top and bottom of the high-flow specimen. Figure 4.5 shows the void content at the top and bottom half of the high-flow specimen, where the bottom half is the half closer to the inlet of the mold, and the top half is closer to the end of the mold. This increase of voids at the top can be as high as $4.26\times$ that of the bottom.

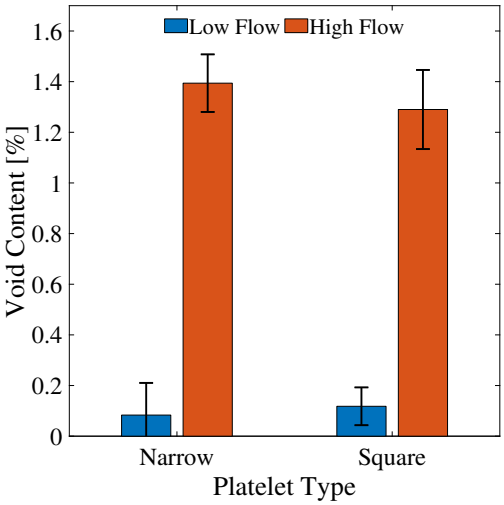

Figure 4.4: Compression of void content between low and high flow coupons found through CT scans.

This could be caused by turbulence in the flow changing along the flow path. The mold used has the flow of platelets bend into the prongs of the "fork". This change in flow could cause turbulence at the inlet, then as the flow continues the turbulence decreases until the end of the mold where there is a wall. The tensile coupon is taken from the end of the mold to about half the length of the fork's prong, so the bottom of the tensile coupon is in a less turbulent part of the flow which is why the void content is lower. Another factor is that the trapped air has nowhere to go at the end of the mold. This spatial variation is another factor to consider when manufacturing a part made using DFCs. When manufacturing a DFC part, small volumes of high-flow can be good to reorient fibers into a loading direction, but longer areas of flow could result in void formation. However, more work needs to be done to determine if the flow length affects the void formation in DFCs.

4.3.2.2 Orientation Tensor

From the CT scans, the orientation tensors (A_{ij}) [106] of low- and high-flow coupons are found. The orientation tenor is found by taking the dyadic product of the orientation vector of a fiber. The out-of-plane orientation is found to be minimal, thus the orientation tensor

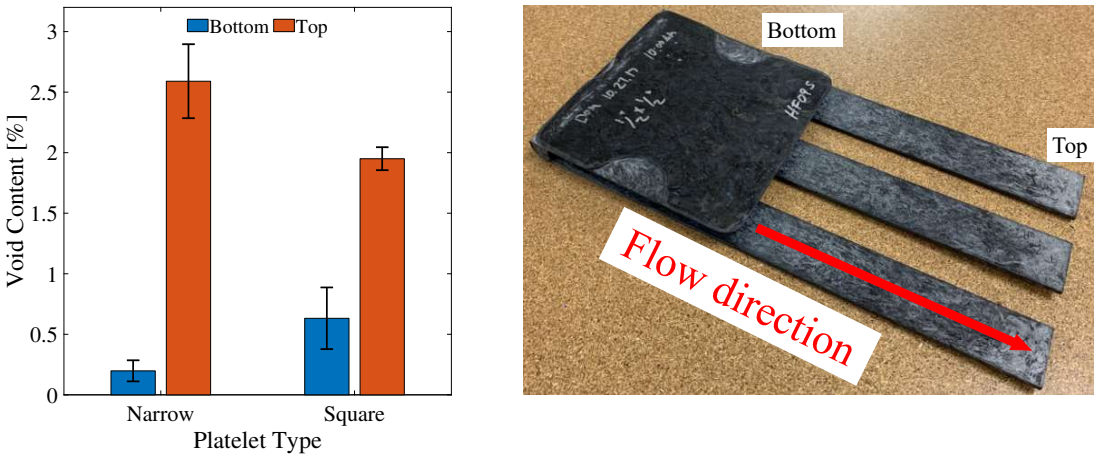

Figure 4.5: Void content of the two halves of the high flow specimen.

can be described with the first entry of the tensor, A_{11}. An A_{11} of 0.5 means the orientation is perfectly random, and an A_{11} of 1 means all fibers are aligned in the loading direction. The A_{11} of low-flow narrow platelet coupons are $0.49 \pm 4.8\%$ and the A_{11} of high-flow coupons are $0.63 \pm 5.8\%$. This is a percent increase of 29% and shows why there is an increase in the tensile strength of high-flow tensile coupons. The A_{11} of low-flow square platelet coupons are $0.49 \pm 9.2\%$ and the A_{11} of high-flow coupons are $0.62 \pm 7.7\%$. This is a percent increase of 27% and shows why there is an increase in the tensile properties of high-flow tensile coupons.

Table 4.2: Summary of the average orientation tensor found through X-Ray μCT.

	Narrow	Square
Low Flow	$0.49 \pm 4.8\%$	$0.49 \pm 9.2\%$
High Flow	$0.63 \pm 5.8\%$	$0.62 \pm 7.7\%$
Percent Increase [%]	29%	27%

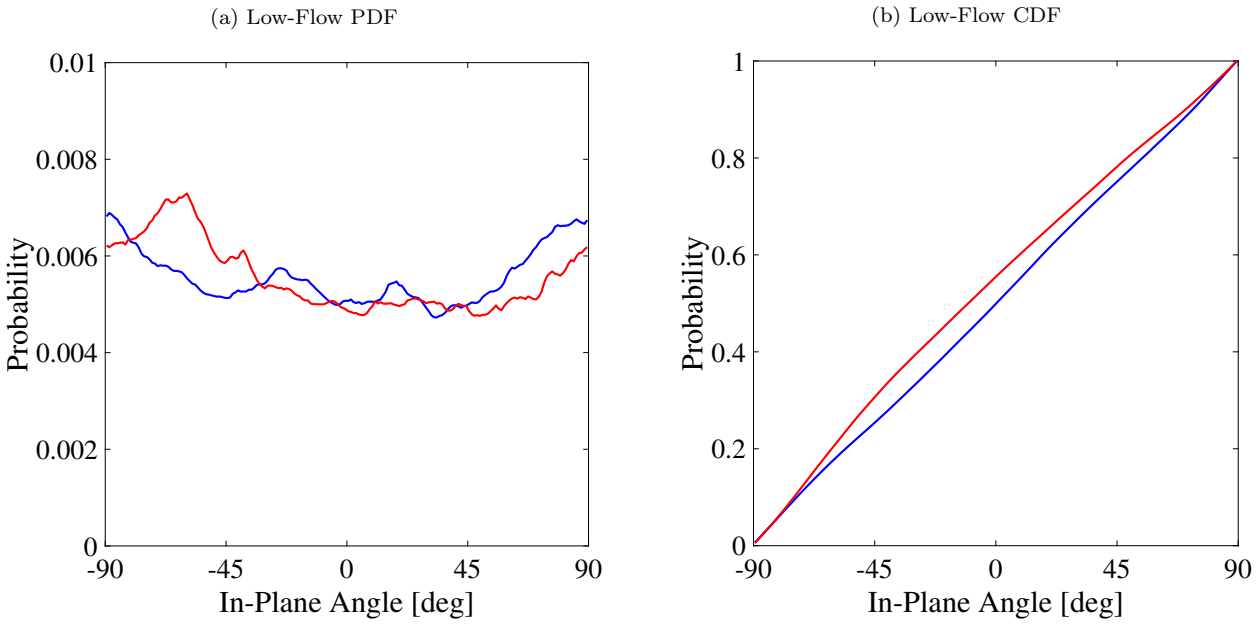

Figure 4.6: Probability Distribution Functions (PDFs) and Cumulative Distribution Functions (CDFs) of two 25.4 × 25.4 mm sections on a low-flow square platelet coupon.

4.3.2.3 Platelet Orientation Statistical Analysis

Figures 4.6 and 4.7 shows two Probability Distribution Functions (PDFs) and Cumulative Distribution Functions (CDFs) of a low and high-flow coupon. From Fig. 4.6, it can be seen that the low-flow coupon follows a uniform distribution closely. On the other hand, the high-flow orientations follow a mix of a uniform and normal distribution. Close to the flow direction (0°) the orientations follow a normal distribution, then transverse to the flow direction (±90°) the orientations become more uniform.

Figure 4.8 shows the cured DFC specimens, a slice from the scan, and the in-plan angle probability distribution for 6 1×1 inch Statistical Representative Volume Elements (SRVEs). The initial charge is compressed and flows into fingers to promote the biased orientation. It can be seen that the six sections are similar and the probability distribution of the in-plane fiber angles do not change along the length of the specimen. On the other hand, the

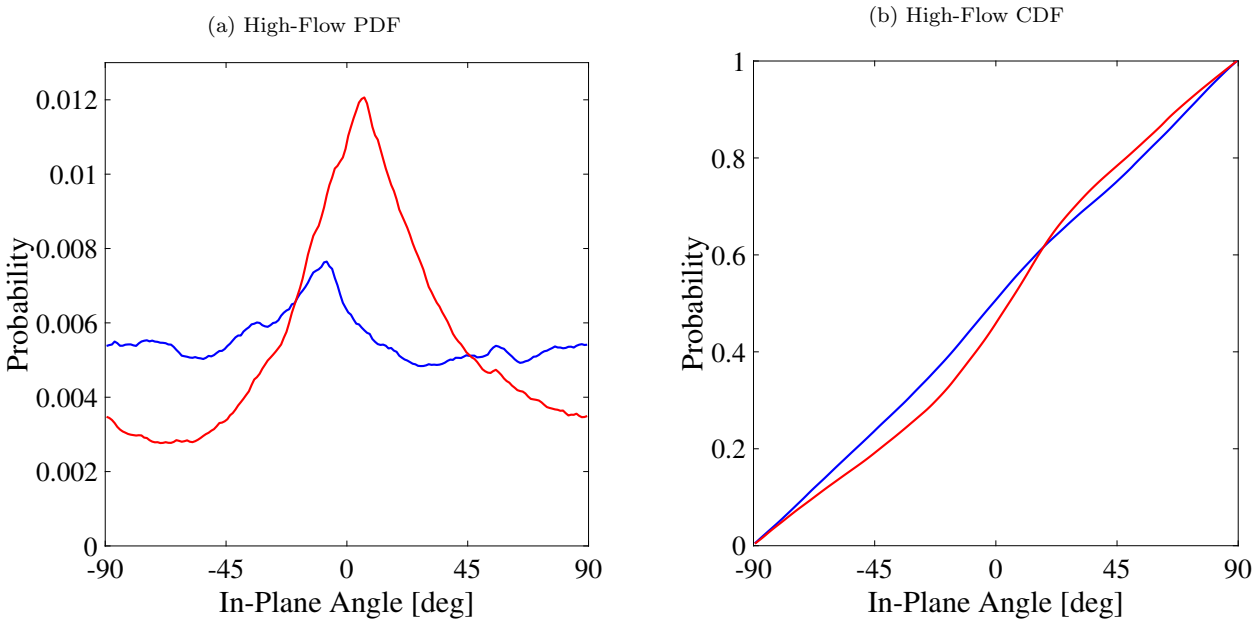

Figure 4.7: Probability Distribution Functions (PDFs) and Cumulative Distribution Functions (CDFs) of two 25.4 × 25.4 mm sections on a high-flow square platelet coupon.

out-of-plane fiber angle appears to be more aligned to the xy-plane at the center of the specimen (sections 3 and 4), this can be seen in fig. 4.9. Here, an out-of-plane fiber angle of 90° indicates that the fibers are on the xy-plane. Starting from section 1, the peak at 90° is low, and as you go to the center of the specimen, the peak becomes higher. After section 4, the peak starts to become lower again. This is due to the flow being turbulent at the beginning, since the platelets have to go through a bend. At the center of the specimen the flow becomes laminar which allows for more fiber aligned with the xy-plane. Finally, as the platelets reach the edge of the mold, the flow becomes more turbulent.

In order to use the probability data for mesostructure generation, the Cumulative Density Function (CDF) is obtained. The following equation is used to fit the CDF:

$$F(x) = \left[a - b * erf(\frac{x-\mu}{\sqrt{2}\sigma})\right] + c * (x - d) \tag{4.1}$$

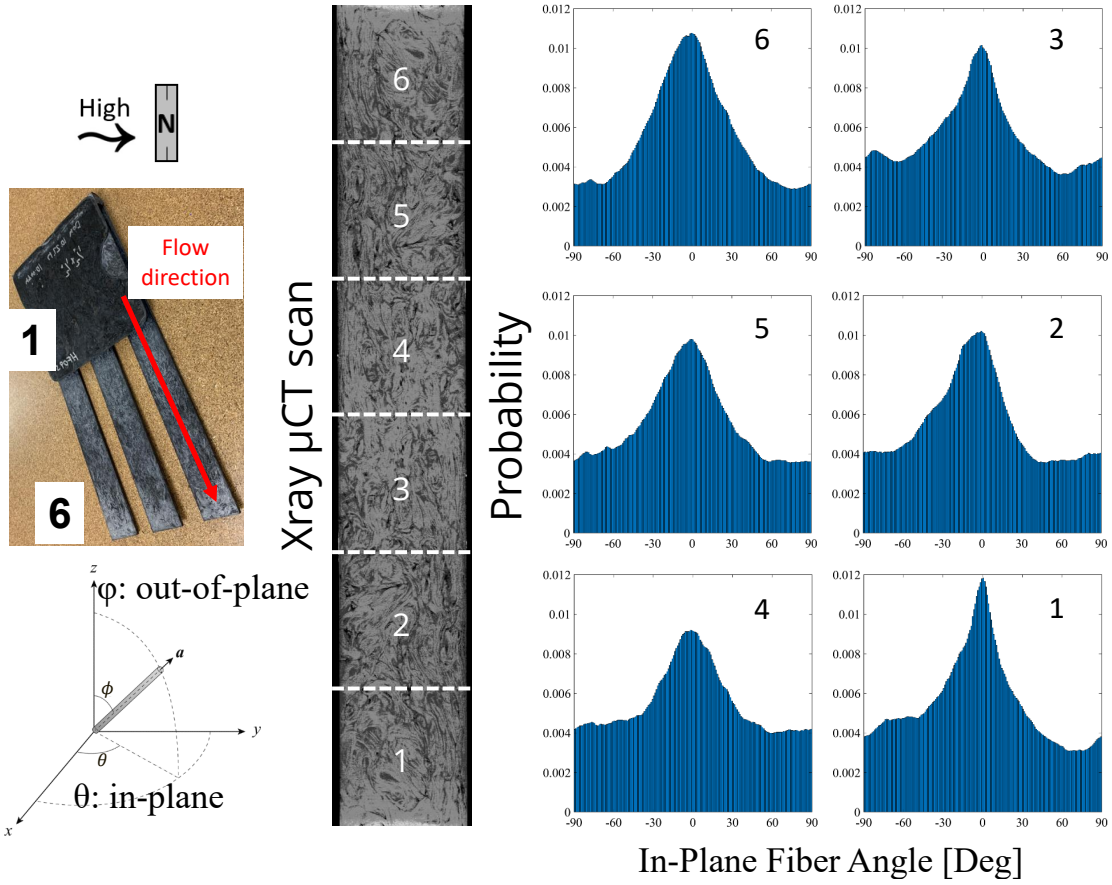

Figure 4.8: The probability distribution of the in-plane platelet angels of high flow narrow platelet specimen found through X-Ray CT scanning. The specimen is divided into 6 1×1 inch SRVEs.

The first part of this equation is the CDF for a Normal distribution, and the second part of the equation is the CDF for a uniform distribution. This was chosen because the PDF of the in-plane fiber angles appears to be a combination of these two distributions. The PDFs have a bell curve at the center, but do not go to zero at the tails, instead they level off like a uniform distribution. An example of the fitting can be seen in fig. 4.10. Here, the fitted CDF using eq. 4.1 matches the empirical CDF found from the CT scans with a percent difference of 1.84%. It can be seen that the uniform part of the CDF equation is tangent to the tails of the empirical CDF. At about $-45°$, the Normal part of the distribution kicks in and at $45°$

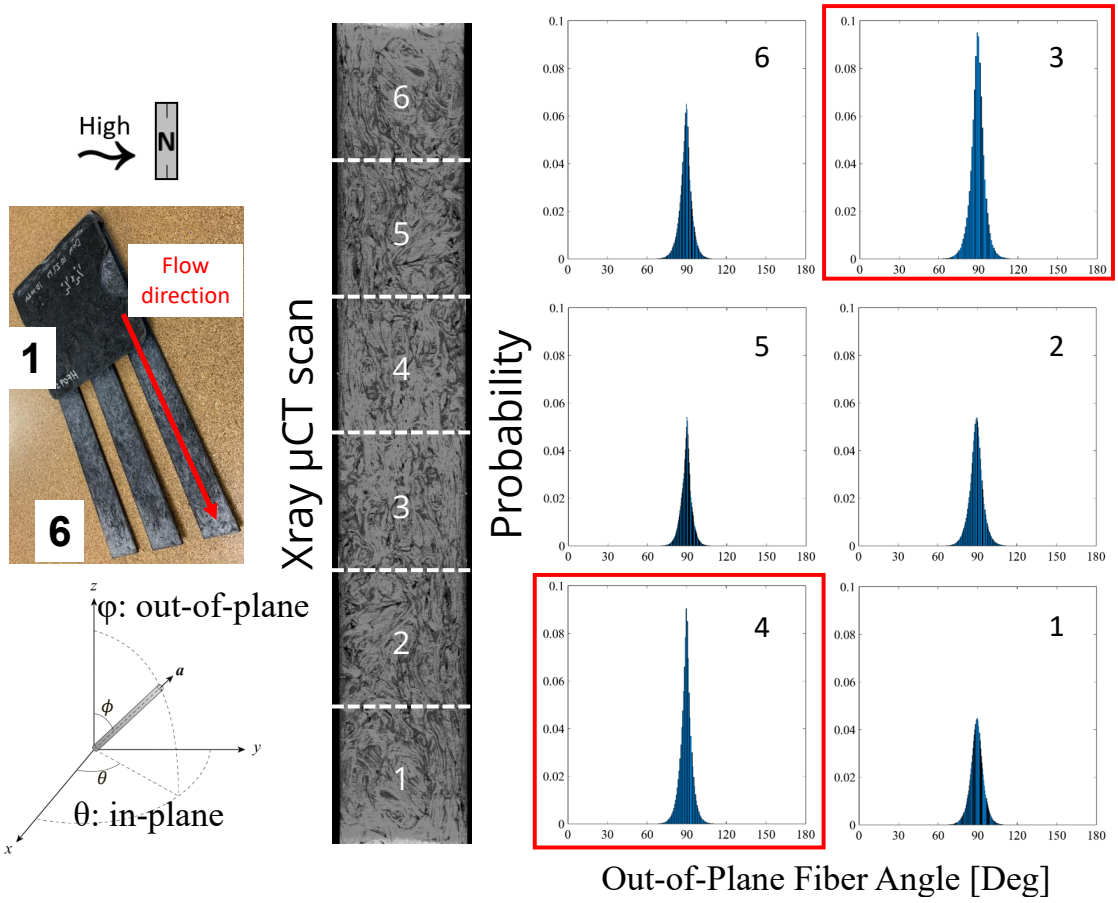

Figure 4.9: The probability distribution of the out-of-plane platelet angels of high flow narrow platelet specimen found through X-Ray CT scanning. The specimen is divided into 6 1×1 inch SRVEs.

it levels off again so that the uniform part takes over.

4.4 Finite element model

In this study, finite element modeling is used to predict the modulus and strength of DFCs with various sizes and flow conditions. Due to the inhomogeneous mesostructure of DFCs, the platelet constitutive properties and orientation distribution is very important in order to capture the performance of structures made with this material. Also, the partition size must be sufficiently small in order capture the platelets, but not too small to make the simulations

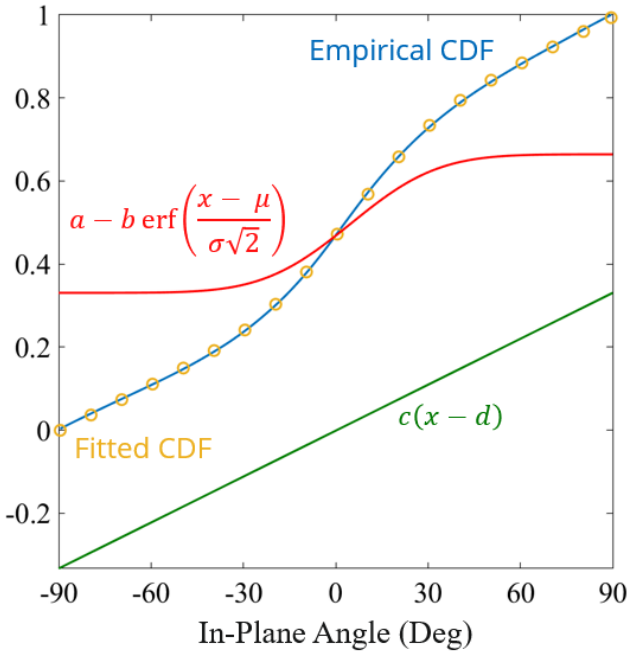

Figure 4.10: An example of a CDF found for a norrow platelet high flow coupon.

to computationally expensive. In this study, platelets are partitioned into grids of 0.5×0.5 mm.

4.4.1 Mesostructure Generation

The mesostructure generation proposed by Ko et al. [111] is modified to use any given CDF as an input for fiber angles. To ensure that the whole CDF is explored while generating platelets, the Latin Hypercube Sampling (LHS) method is implemented. LHS cuts a domain into even sections and randomly chooses a point in every subsection in order to ensure the full probability distribution is covered. The final number of platelets in the mesostructure generation can not be known at the start, the initial domain is set to be the full CDF, then once a point is select from all available subdomain, the domain is evenly divided into further subdomains. The first three subdomain divines can be seen in fig. 4.11. The order of which subdomain is selected from is chosen at random. This ensures that there is no bias. This

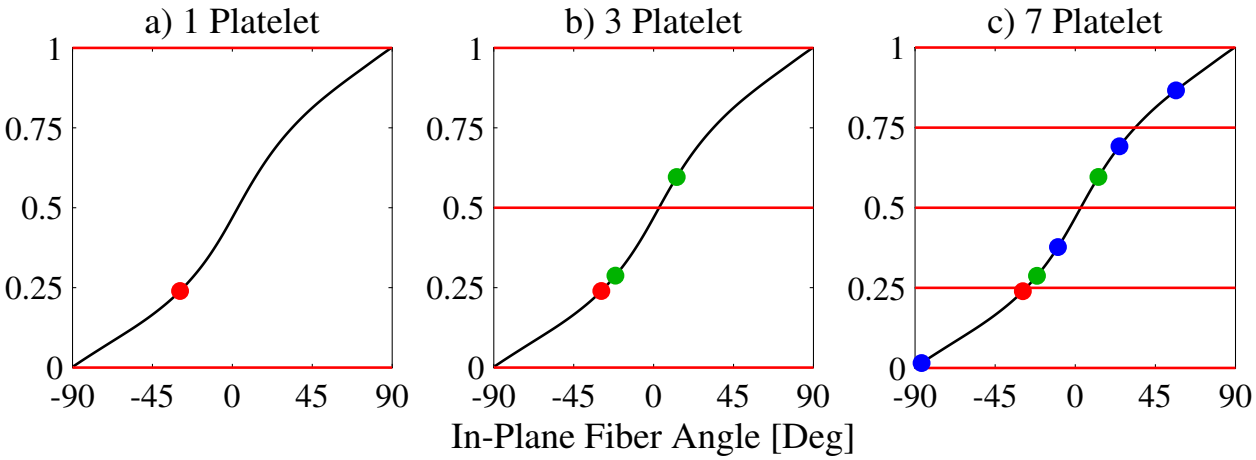

Figure 4.11: Example of fiber angle generation using the empirical CDF and LHS. a) Is the initial domain of sampling, b) is the second domain of sampling, and c) is the third domain.

is important for the final parts of the orientation selection since not all subdomains will be used in the final division.

Figure 4.12 compares the probability distribution from the CT scans to the ones from the mesostructure generation. Figure 4.12a shows the six SRVEs not matching perfectly. This is due to the fact that there is only about 1500 unique platelets in each section. However looking at fig. 4.12b, when comparing the probability distribution of the whole coupon, the generated mesostructure matches the CT scanned data closely. The match of the two distributions become closer when averaging through multiple coupons. Figure 4.13 compares the probability distribution from the CT scans to the ones from the mesostructure generation across 5 coupons. When using the orientations across 5 coupons, there is now about 7500 platelets in each section and the probability distributions of the six SRVEs match more closely to the CT scanned data. At the same time, the overall coupon distribution also match better.

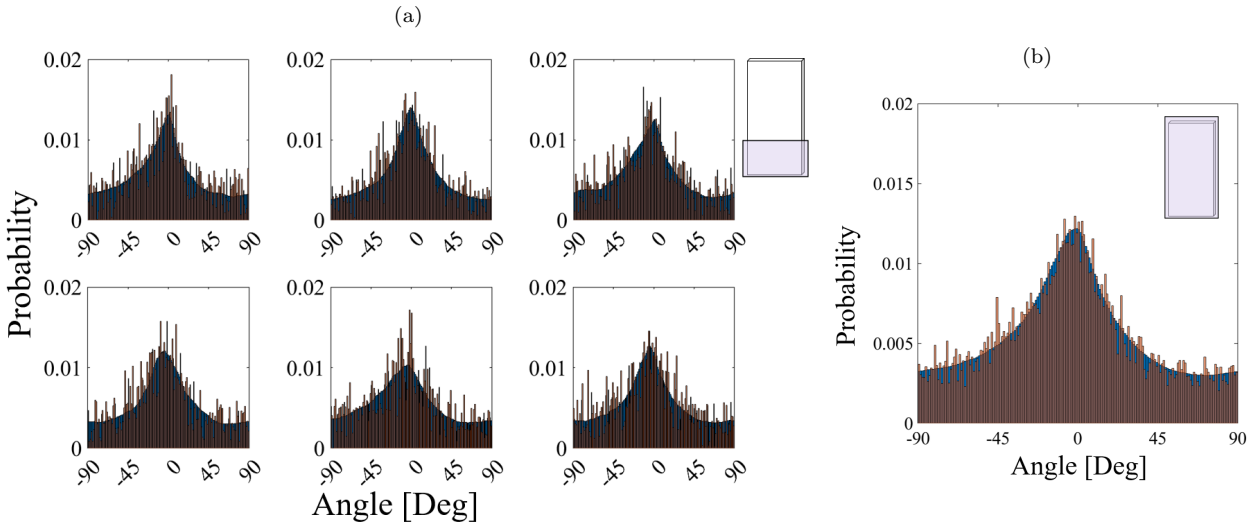

Figure 4.12: Probability distribution from the CT scans and from the mesostructure generation. The blue bars are from the CT scans, and the orange is from the generation. a) shows the distributions for 6 1×1 inch SRVEs, and b) shows the distribution of 1 coupon.

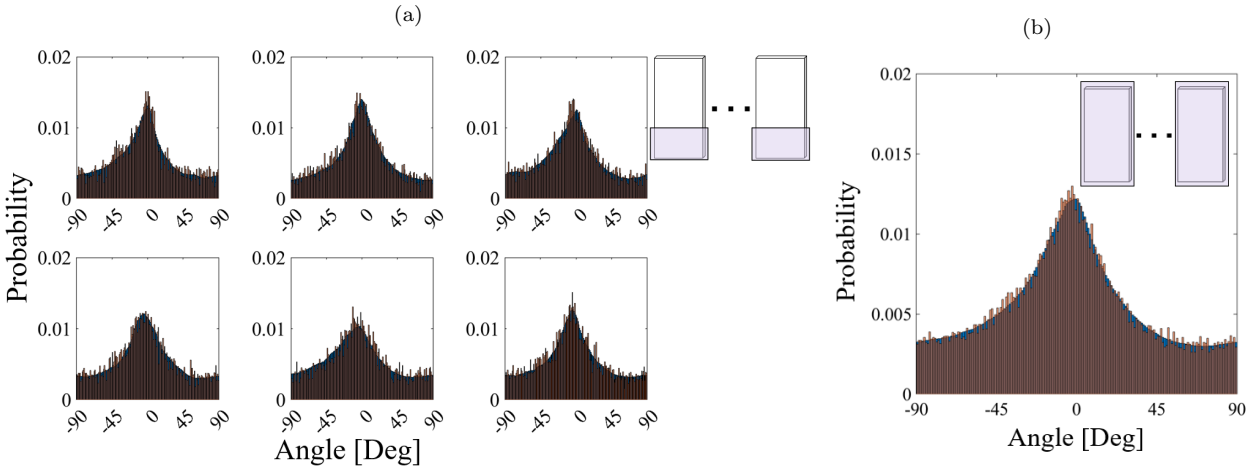

Figure 4.13: Probability distribution from the CT scans and from the mesostructure generation. The blue bars are from the CT scans, and the orange is from the generation. a) shows the distributions for 6 1×1 inch SRVEs across 5 coupons, and b) shows the distribution of 5 coupon.

Once the mesostructure is generated it is imported into Abaqus/Standard to obtain the modulus and Abaqus/Explicit to obtain the strength [76]. The layers of platelets and resin are kept as DFC plies, and 4-node, quadrilateral Belytschko-Tsay shell element with reduced integration (S4R) are used to model them. To model the inter-ply bonding, 8-node 3D cohesive elements are used.

4.4.2 Results of finite element simulations

Figure 4.14 shows the contour plot of the matrix, fiber, and delamination damage variables from a low flow square platelet simulation. It can be seen that the main damage experienced is the matrix damage variable (transverse to fiber). The matrix and delamination damage is spread through out the specimen. On the other hand, fiber damage is very limited and is mainly located at the failure location. This distribution of damage is typical of DFC structure and have been seen in many previous works [10,12,28,34,35,48,85,86,94,95]. Similar damage morphology is also observed in the narrow platelet, and high flow specimen simulations.

Figures 4.15 and 4.16 shows the fracture surfaces of the CT scanned specimen along side the contour plots of the matrix damage variable of the simulations. The figure only shows the specimen that failed in the gauge and leaves out the specimen that failed in the tabs. It can be seen that by using the CDF found in X-Ray CT scans, the exact failure location can be matched accurately.

Figure 4.17, and tables 4.3 and 4.4 show the average modulus and strength found experimentally and computationally for each platelet size and flow condition. Both platelet size effect and flow effects are captured in the simulations. The percent difference in the modulus found from simulations to the experimental value is under 9%. The percent difference of the strength found from simulations to the experimental value is typically under 5%, with only the low flow narrow platelet simulations having a higher percent difference. However, the variation seen in experiments in high and the simulation values fall with in the standard deviation.

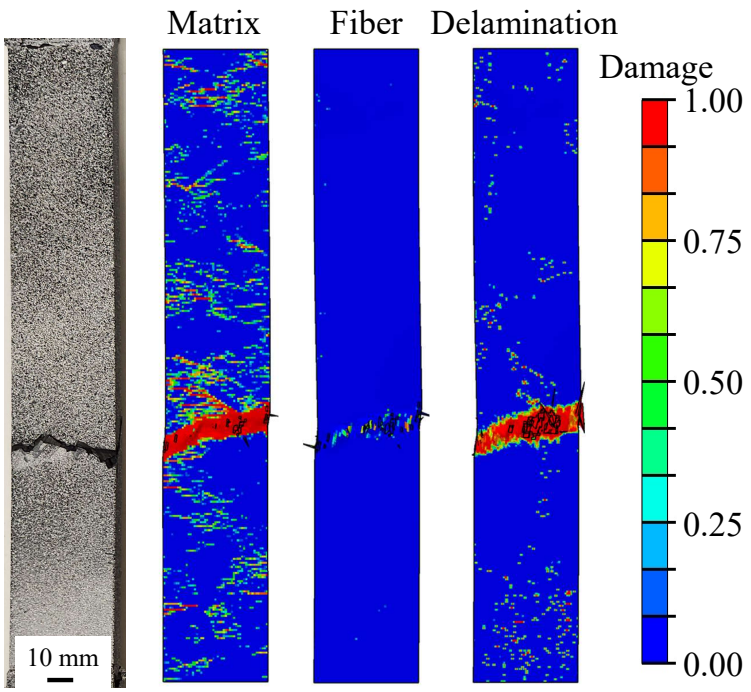

Figure 4.14: Contour plot of the matrix, fiber, and delamination damage variables from simulations.

4.5 Conclusion

In this study, the effects of platelet width and flow on the platelet orientation and tensile properties of Discontinuous Fiber Composites (DFCs) are studied. To do this, narrow and square platelets are used to manufacture DFC laminates. Two manufacture methods are used, 1) a closed mold is used in compression molding, and 2) a "fork" mold is used where platelets are distributed into a rectangular charge and compression forces the platelets into the "prongs" of the fork". From this, specimen are tested in tension and the orientations are found through X-Ray μCT. Based on the results, the following conclusions can be made:

1. For low flow specimen, as platelet width decreases tensile properties increase. The percent difference in modulus and strength between the two platelets are 8% and 20% respectively. However, the high flow specimen did not see the same difference between the two platelet sizes. Here the modulus and strength are about the same between the

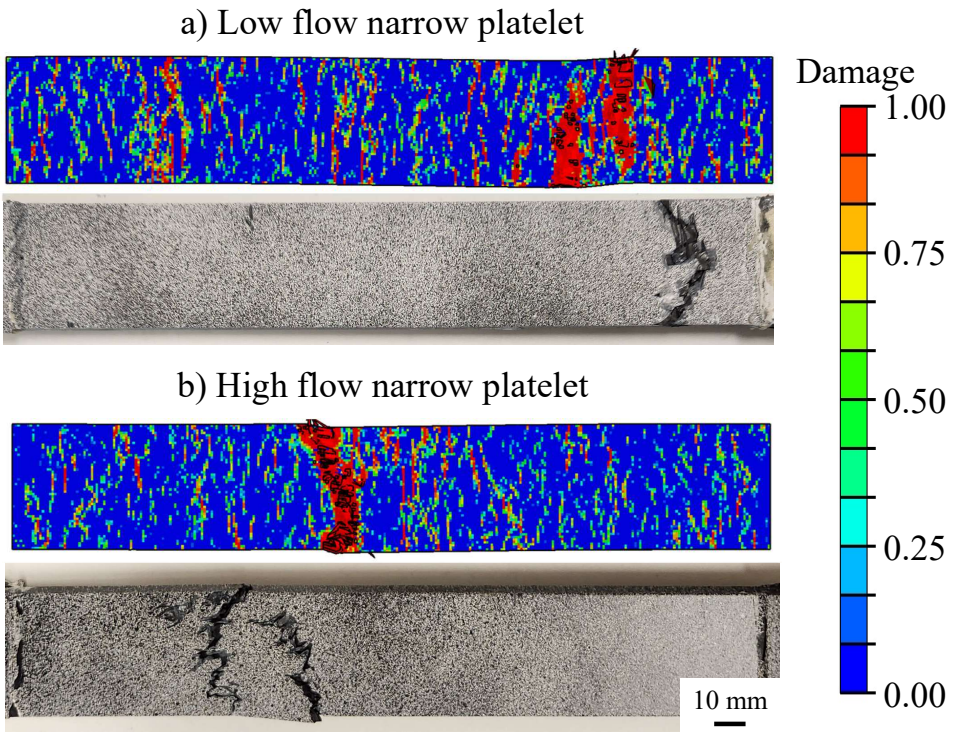

Figure 4.15: a) Matrix damage of the low flow narrow platelet simulation. b) Matrix damage of the high flow narrow platelet simulation.

two platelet sizes.

2. The platelets reorient to align with the flow, which causes the tensile properties in the flow direction to improve. For the square platelets the modulus is improved by 22%, and the strength by 10%. On the other hand, only the modulus improved by 11% for the narrow platelet specimen while the strength remained the same. It is suspected that void formation caused by flow is the reason for not seeing improvement in strength for the narrow platelet specimen.

3. High flow specimen exhibited a higher void content than the low flow specimen. The void formation caused by flow has a spacial dependence, where the bottom of the tensile coupon, close to the inlet of the mold, has a lower void content than the the top, at

a) Low flow square platelet

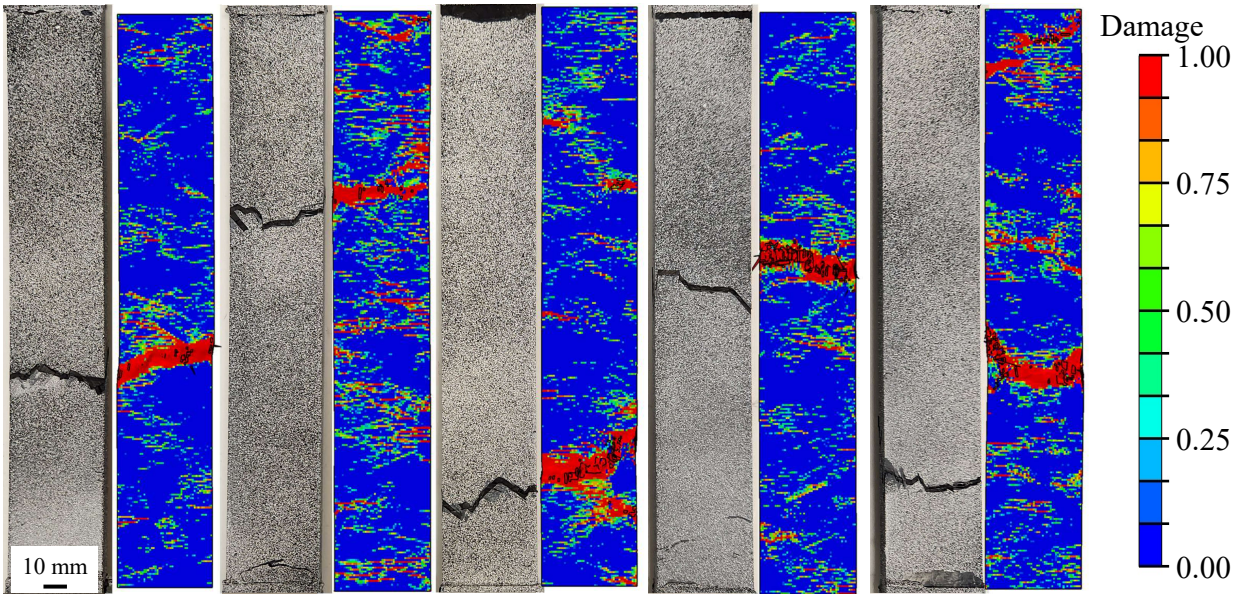

b) High flow square platelet

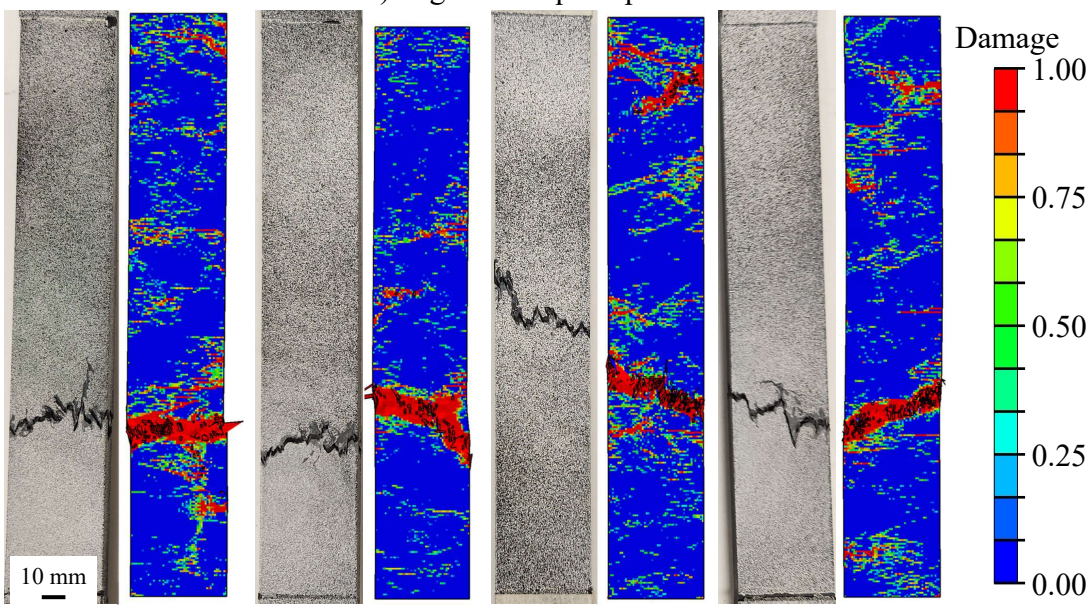

Figure 4.16: a) Matrix damage of the low flow square platelet simulation. b) Matrix damage of the high flow square platelet simulation.

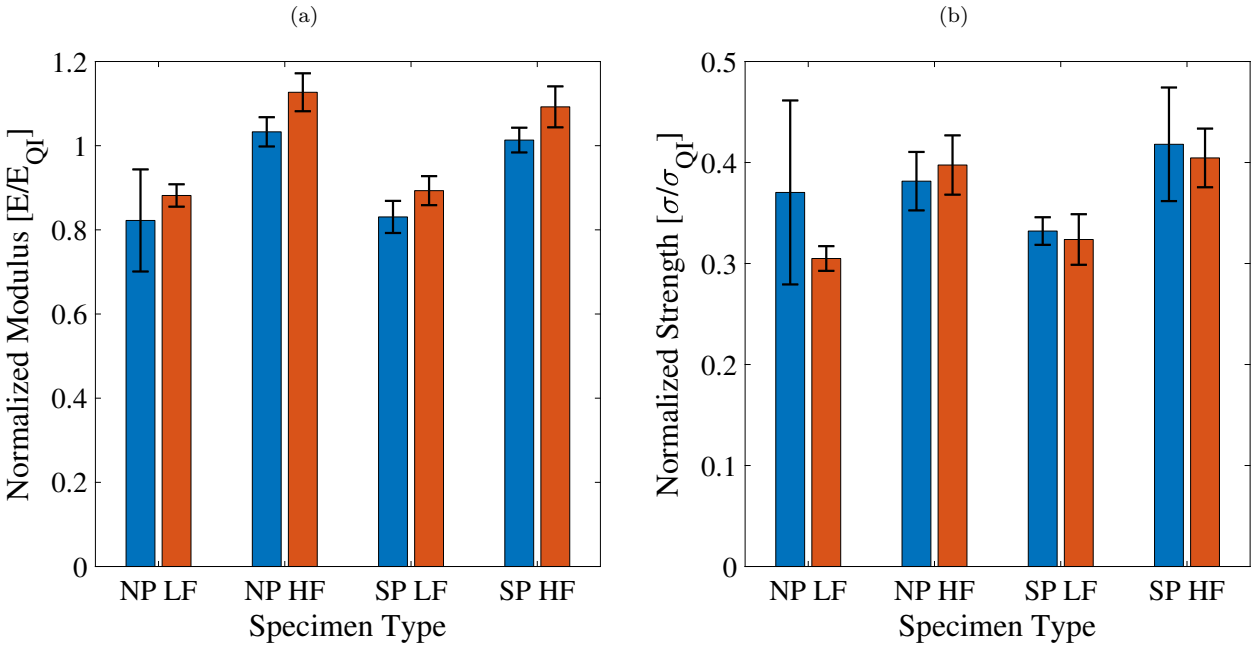

Figure 4.17: Comparison of modulus and strength results from experiments and simulations.

the end of the mold. This is most likely caused by changes in flow conditions along the length of the specimen and trapped air. The length of the high flow specimen tested in this study is much shorter than what would be seen in an actual part. More work can be done to determine the optimal length of flow to achieve reorientation of platelets while not introducing porosity.

4. A mesostructure generator is developed to take a cumulative distribution function of fiber orientations to randomly generate a realistic mesostructure based on X-Ray Computed Tomography scans. The generated coupons are able to accurately match the tensile response of the scanned DFC coupons. This tool can be used to minimize physical testing of DFC parts which are highly stochastic.

Table 4.3: Summary of the normalized modulus results from experiments and simulations.

	Narrow Low	Narrow High	Square Low	Square High
Experimental Modulus	$0.82 \pm 14.75\%$	$1.03 \pm 3.37\%$	$0.83 \pm 4.59\%$	$1.01 \pm 2.90\%$
Simulation Modulus	$0.88 \pm 3.01\%$	$1.13 \pm 4.00\%$	$0.89 \pm 3.86\%$	$1.09 \pm 4.46\%$
Percent Difference [%]	6.97%	8.71%	7.24%	7.50%

Table 4.4: Summary of the normalized strength results from experiments and simulations.

	Narrow Low	Narrow High	Square Low	Square High
Experimental Strength	$0.37 \pm 24.59\%$	$0.38 \pm 7.59\%$	$0.33 \pm 4.11\%$	$0.42 \pm 13.45\%$
Simulation Strength	$0.30 \pm 4.01\%$	$0.40 \pm 7.38\%$	$0.32 \pm 7.73\%$	$0.40 \pm 7.18\%$
Percent Difference [%]	19.37%	4.11%	2.55%	3.28%

Chapter 5

ANALYZING THE REAL APPLICATION MADE OF DFCS

5.1 Introduction

When manufacturing parts with complex geometries, like brackets, traditional composites have many drawbacks. When manufacturing parts with curves, traditional composites can easily have wrinkles [112], and using an automated fiber placement machine to mitigate this will introduce gaps and overlaps of fiber tows [113]. Additionally, without these defects, there is still a need to use an autoclave to cure the composite parts which is a time-consuming process when manufacturing a bracket which requires high throughput. This is where Discontinuous Fiber Composites (DFCs) can be used to solve these problems. Due to being made with platelets, complex shapes are easier to make, and compression molding can be used to cure parts in minutes [34,114]. However, DFCs come with their own challenges, such as the reorientation of platelets due to the flow in the mold. This work aims to study the intricacies of the use of DFCs in the manufacturing of brackets.

Previous studies have been performed on flat coupons [10, 12, 28, 31, 34, 35, 38, 85, 86, 99, 101, 109]. However, when it comes to complex 3D structure, minimal work can be found in literature [115–119]. In addition, the work on 3D structure made with DFCs focuses on flow simulations and obtaining the fiber orientations of the structure [115–117]. Work done on the mechanical performance and simulation of complex structures made using DFCs is very limited [118, 119]. These works focused on mechanical testing and simulations only reporting the stiffness of the brackets. This work aims to tackle this gap in literature by testing a bracket made of DFCs in tension and simulating these tests using X-ray Computed Tomography data.

5.2 Materials and testing methods

5.2.1 Material preparation

In this study, two platelet sizes were investigated, a narrow and square platelet. The square platelet was 12.7 mm ×12.7 mm, while the narrow platelet used the same length but with a reduced width (the exact width cannot be disclosed due to intellectual property issues). The platelets were made using AS4D/PEKK thermoplastic tape from Solvay. Figure 5.1 shows the brackets that were manufactured by Sekisui Aerospace [98]. A total of 14 brackets of each platelet size were manufactured for testing, of which half were tested in tension, while the other half was tested in bending.

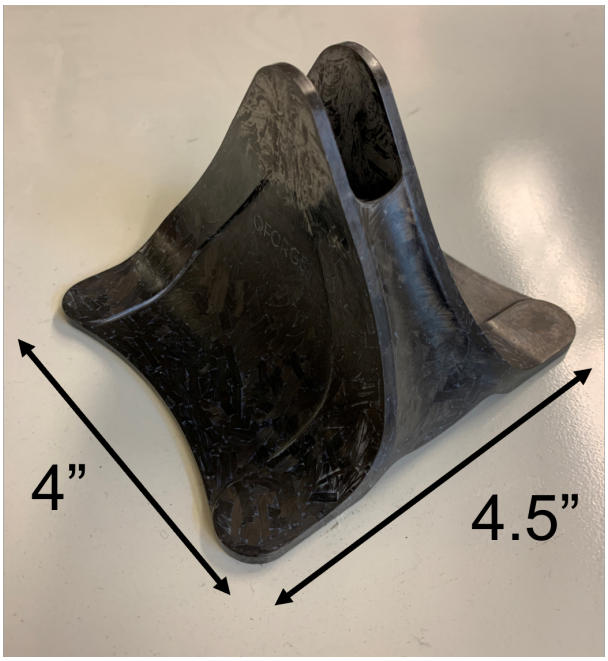

Figure 5.1: Bracket made by Sekisui Aerospace using DFC.

5.2.1.1 Data acquisition

A Shore Western servo-hydraulic axial-torsion load frame with a closed-loop control and 445 kN capacity was used for the tests. The load was sampled at a rate of 10 Hz. To observe the strain field close to the top pin and to obtain displacements without the influence of the

compliance of the load frame and the fixture, Digital Image Correlation (DIC) was used. Two cameras were used to capture the displacements on both sides of the bracket. A Nikon D5600 DSLR and a Nikon D7500 DSLR with Nikon AF micro 200 mm and Sigma 135 mm DG HSM lenses were used to capture the DIC. The images were sampled at a rate of 1 Hz and GOM Correlate was used to analyze the DIC to find the strain and displacement fields [52]. For the bending tests, two 5 MP cameras with Schneider lenses were used to perform 3D DIC on the base of the bracket. The images were sampled at a rate of 1 Hz and Vic-3D was used to analyze the DIC to find the strain field [120].

5.2.2 Mechanical tests

Figure 5.2a shows the fixtures used to test the brackets in tension. The tests were performed at a deflection rate of 0.3 mm/min. The bolts at the base of the fixture were torqued to 13.56 N-m. Seven brackets of each platelet size were tested in tension.

Figure 5.2b shows the fixtures used to test the brackets in bending. The tests were performed at a deflection rate of 0.6 mm/min. The bolts at the base of the fixture were torqued to 13.56 N-m. Seven brackets of each platelet size were tested in bending.

5.2.3 X-Ray micro-computed tomography

Prior to testing, X-Ray micro-computed tomography (μCT) was performed to obtain the exact mesostructure of the bracket. A total of 16 brackets were scanned, so that 4 out of the 7 brackets tested in each configuration and each platelet size had a μCT scan. A NSI X5000 [104] was used to obtain scans with a voxel size of 38μm. These scans are analyzed using an in-house code which uses a 3D Gaussian distribution derivative filter to find the local density gradients and reduce noise [110]. The probability distribution of orientations is then used as an input to a mesostructure generation algorithm to recreate coupons with the same orientations as the ones scanned. In addition to the in-house code, Dragonfly [121] is used to obtain the void content from the μCT scans,

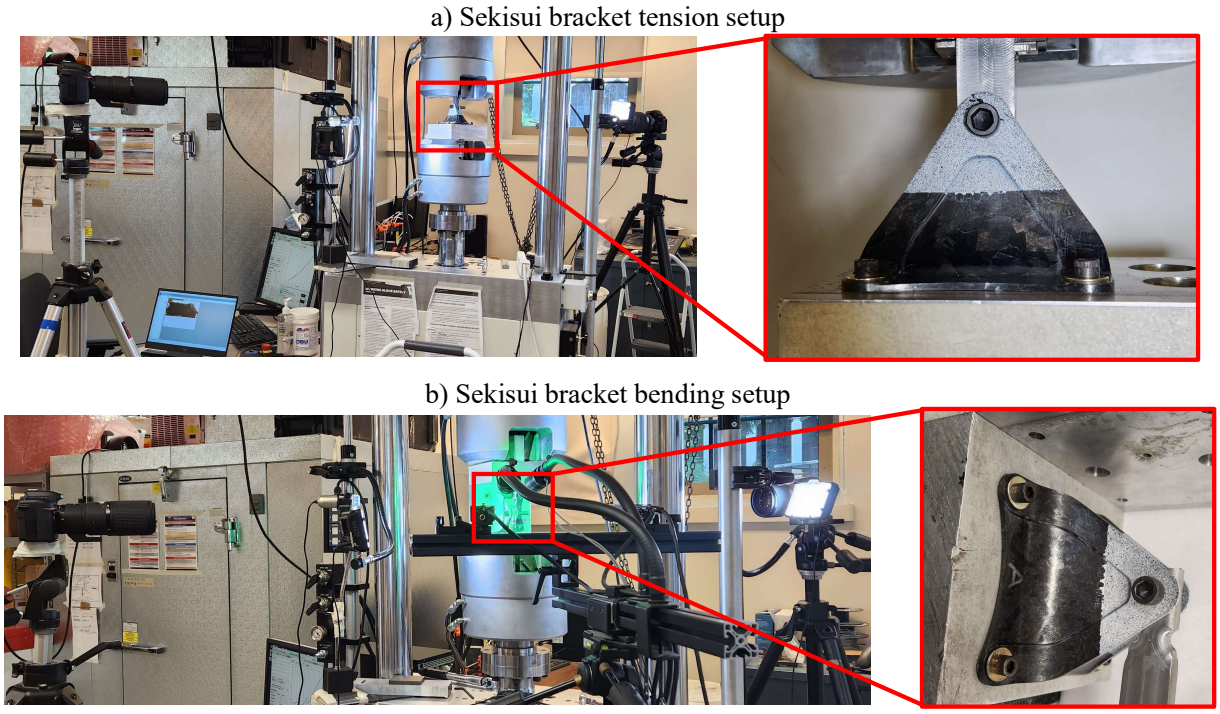

Figure 5.2: a) Tension test setup for the Sekisui bracket. b) Bending test setup for the Sekisui bracket.

5.3 Experimental results

5.3.1 Tensile tests

Figure 5.3 show the force vs displacement curves of the Sekisui brackets tested in tension. Similar to what was seen in Chapter 4, the narrow platelet brackets out performed the square platelet ones. There is a 31% difference between the stiffness of the narrow and square platelet brackets, and a 38% difference in the strength. The percent difference in modulus and strength between the two platelet sizes in tension seen in the previous chapter is 7.61% and 20.44%.

Both the narrow and square platelet brackets have specimen with nonlinear curves. However, the nonlinearity seen in the square brackets only occur after the first drop in load, whereas the nonlinearity in the narrow platelets occurs before any drop in load. By looking

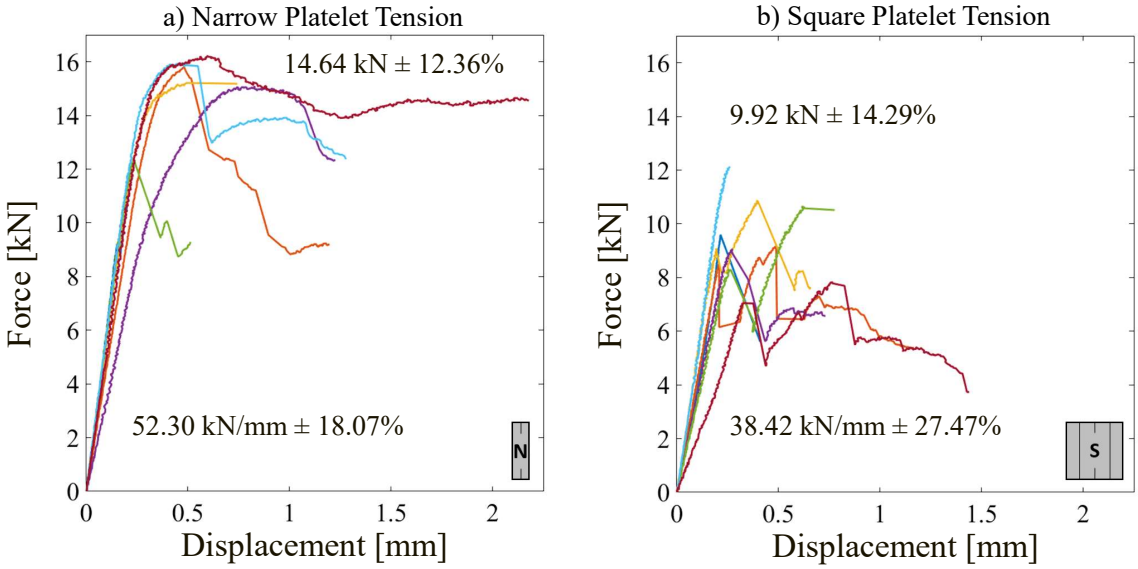

Figure 5.3: Tensile force vs displacement curves of a) narrow platelet and b) square platelet Sekisui brackets.

at the fracture surfaces of the brackets in Figure 5.4 the cause of the nonlinearity can be seen. It can be seen that the narrow platelet brackets that experience nonlinearity have crushing at the contact between the pin and bracket. This crushing is not seen in the square platelet brackets. For the square platelet brackets the nonlinearity is caused by progressive failure and crack propagation.

Figure 5.5 shows a vector plot of orientations found through X-Ray μCT overlayed onto the fracture surface of a square platelet bracket. All vector plots and contour plots of the orientation tensor with fracture surfaces can be found in the Appendix A. It can be seen that the fracture path propagates parallel to the fiber orientations. This is to be expected, since the path of least resistance would be between fibers rather than through them. This sort of damage has been seen in previous studies on flat DFC coupons [10, 12, 28, 34, 35, 48, 85, 86, 94, 95]

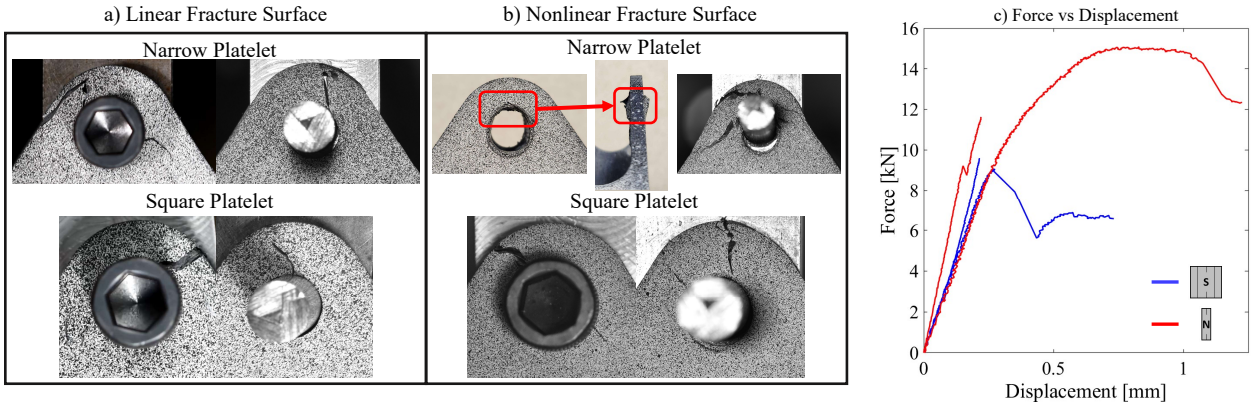

Figure 5.4: a) Fracture surface of specimen exhibiting a linear force vs displacement curve. b) fracture surface of specimen exhibiting a nonlinear force vs displacement curve. c) Force vs displacement curves of the specimen shown in a) and b).

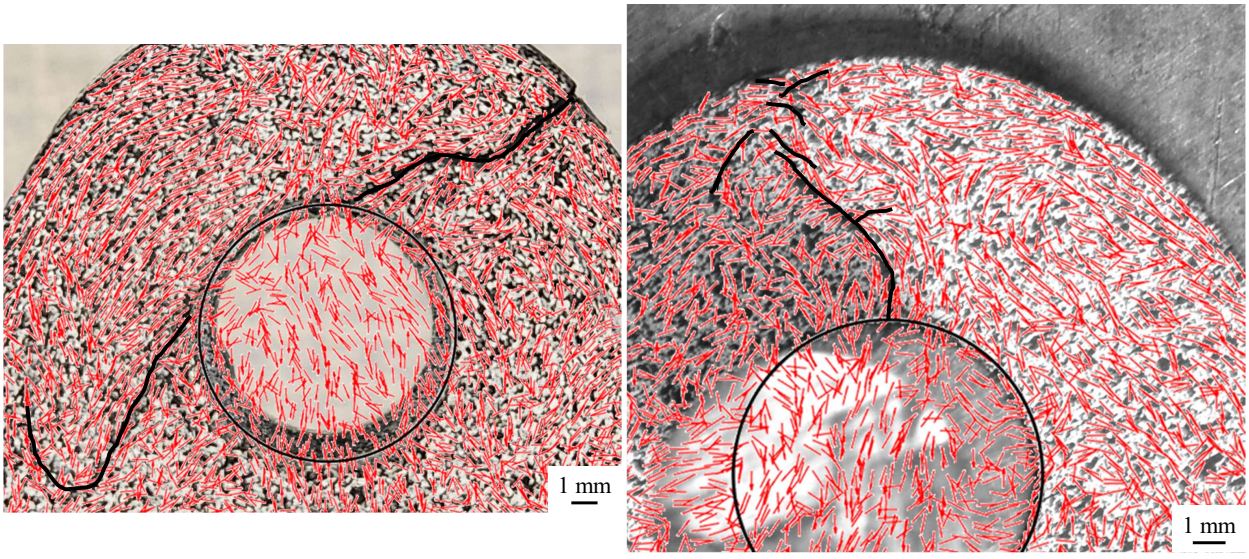

Figure 5.5: Vector plot obtained through a CT scan overlayed onto the fracture surface of a square platelet bracket tested in tension.

5.3.2 Bending tests

Figure 5.6 show the force vs displacement curves of the Sekisui brackets tested in bending. Similar to what was seen in Chapter 4 and with tension tests, the narrow platelet brackets out

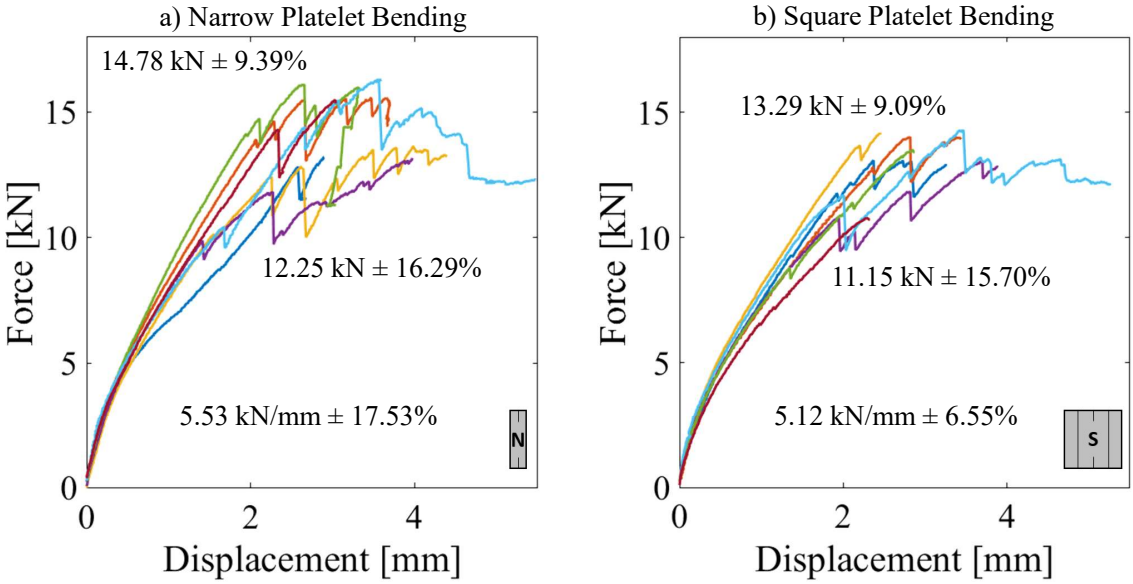

Figure 5.6: Bending force vs displacement curves of a) narrow platelet and b) square platelet Sekisui brackets.

performed the square platelet ones. There is a 8% difference in the the stiffness of the narrow and square platelet brackets, a 9% difference in the initial strength, and a 11% difference in the ultimate strength. The percent difference in modulus and strength between the two platelet sizes in tension seen in the previous chapter is 7.61% and 20.44%.

Although all specimen has damage at the base of the bracket on the side theat experience tension, both the narrow and square platelet brackets have specimen that also failed at the top pin. This can be seen in Figure 5.7. Three out of seven narrow platelet and two out of seven square platelet brackets had cracks at the top pin hole. However, when failure at the top pin occurred, fracture at the bottom of the bracket always occurred first. The continuous drops in load that occur after the first drop is due to progressive damage at the base of the bracket, or from failure occurring at the top pin hole.

Figure 5.8 shows a vector plot of orientations found through X-Ray μCT overlayed onto the fracture surface of a square platelet bracket. All vector plots and contour plots of the orientation tensor with fracture surfaces can be found in the Appendix A. It can be seen that the fracture path propagates parallel to the fiber orientations. This is to be expected,

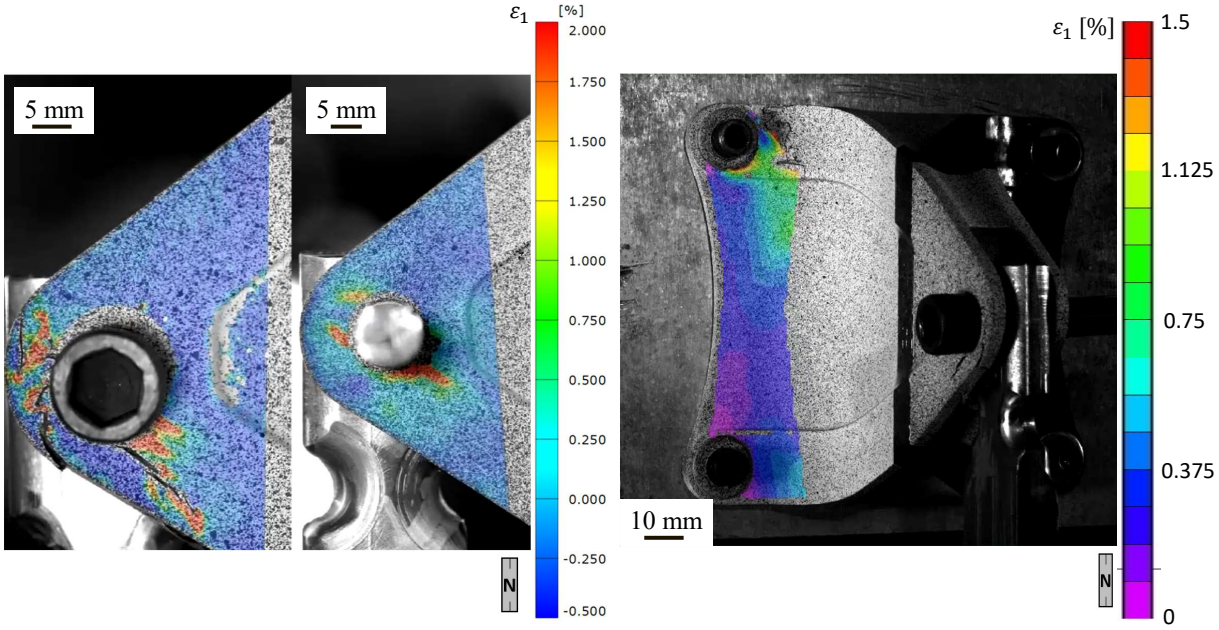

Figure 5.7: Contour plot of the max principle strain of a bending specimen who has fracture at the top of the bracket. When failure occurs at the top of the bracket, failure at the base of the bracket always occur first.

since the path of least resistance would be between fibers rather than through them. This sort of damage has been seen in previous studies on flat DFC coupons [10, 12, 28, 34, 35, 48, 85, 86, 94, 95]

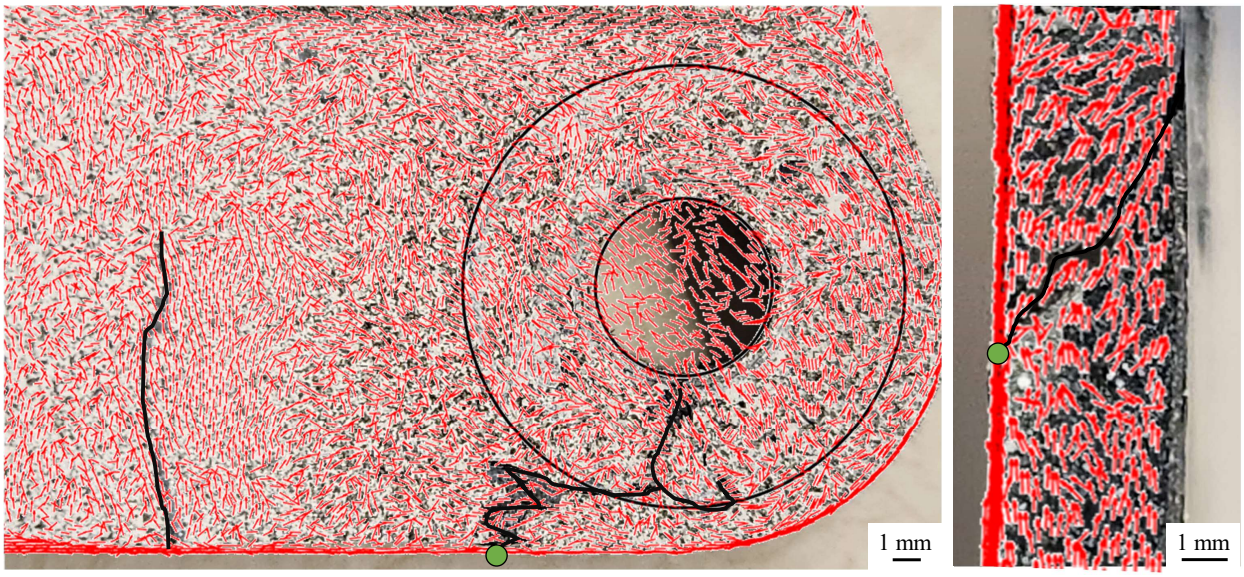

Figure 5.8: Vector plot obtained through a CT scan overlayed onto the fracture surface of a square platelet bracket tested in bending. The green circle is the matching point between the two images.

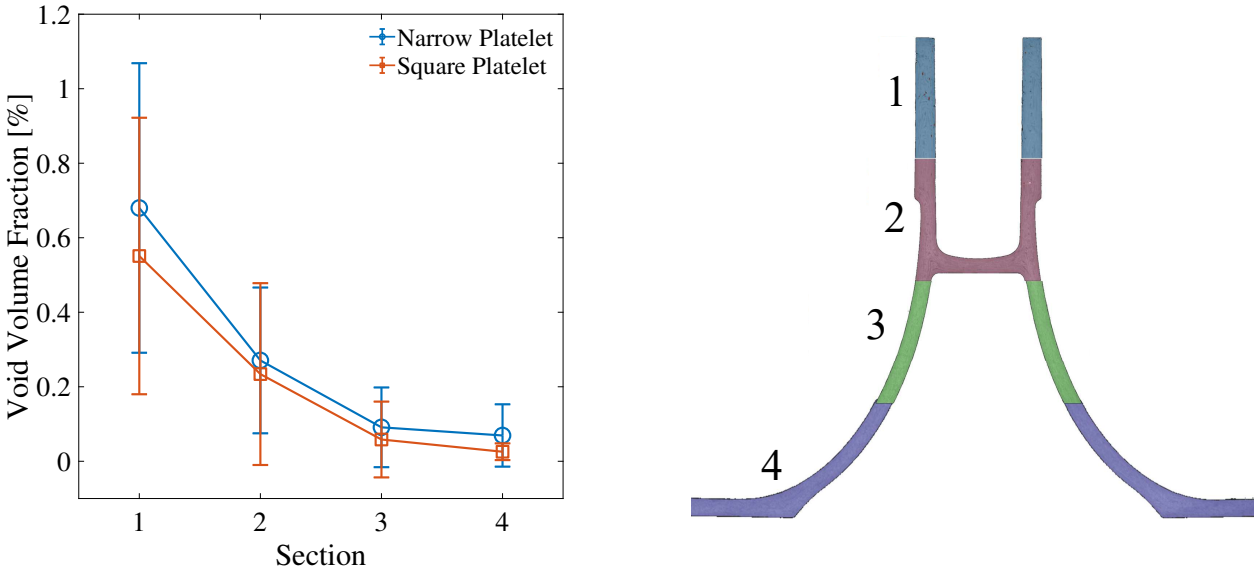

Figure 5.9: Void content of the Sekisui bracket found though CT scans.

5.3.3 Void content

From the X-Ray μCT scans, not only the orientations, but also the void content of the bracket can be found. Figure 5.9 shows the void content of the bracket for both platelet sizes. The bracket is subdivided into 4 sections along the height of the bracket. It can be seen that the void content has a spatial dependence along the height of the bracket. At the top of the bracket the void content of the narrow and square platelet brackets are on average 0.68% and 0.55%, respectively, and decreases to 0.07% and 0.03%, respectively. At the top of the bracket, the maximum void content seen in the narrow and square platelet brackets are 1.32% and 1.24%, respectively. This spatial dependence was expected when look at the bracket in Figure 5.10. Figure 5.10a show the top of the bracket and Figure 5.10b shows the bottom of the bracket. It can be seen that there is some level of flow at the very top of the bracket. This is evident due to the waviness of the platelets at the surface. When looking at the lower half of Fig. 5.10a or at Fig. 5.10b, it is easy to make out the square platelets, but this is not the case for the top of Fig. 5.10a. From Chapter 4, flow induces void formation and this is also seen here. However, even with this void formation there is little impact in mechanical performance. Even though the narrow platelet brackets have a slightly higher void content, they still out perform the square platelet brackets. This is counter to what you would expect when thinking about void content in composites, and is a benefit when using DFCs. This insensitivity to voids have also been seen in previous work [12, 19, 22].

5.4 Simulation

From the μCT scans, Finite Element (FE) simulations can be performed by mapping the orientations onto a mesh, creating a digital twin. In this study, a STEP file the bracket is imported into FEMAP [122] to obtain the tetrahedral mesh. The nodal coordinates and element connectivity are then imported into Matlab [51] to map the orientations. To do this, the center point of each element is found and a nearest neighbor search is performed with the results from μCT scans. To do this quickly, the mesh and the μCT scan are segmented into

(a) (b)

Figure 5.10: View of the a) top and b) bottom of the bracket.

a $3 \times 3 \times 3$ grid and the nearest neighbor search is done in parallel on the smaller chunks. To ensure that the nearest neighbor is accurate close to the edges of the sections, each section of the μCT scan data has a 1 mm overlap with each other.

Once the orientations are mapped, the orientation and mesh information are imported into Abaqus/Explicit [76]. Figure 5.11 shows an example of the simulation assembly. Here, the fixture is explicitly modeled, and the boundary conditions are applied such that they are similar to that of the experiments. The bracket uses C3D10 quadratic tetrahedral elements, while the base plate and top pin are modeled with R3D4 elements, and the bolts are C3D8R and C3D6 elements. The friction coefficient between the various surfaces is taken to be 0.2. The bracket uses the 3D Hashin failure criteria [123] implemented in VUMAT with bi-linear softening in the fiber direction, and linear softening for failure in the matrix direction and in shear. The platelet material properties used in the simulations are taken from [30].

So far, only preliminary simulations have been performed on the Sekisui brackets in tension. The final frame of the simulations along side the fracture surface from experiments can be seen in Figure 5.12 and 5.13. Here the contour plot is of the damage variable in the matrix direction. The preliminary results are very promising, with the fracture in the simulations matching fairly closely with the ones seen in experiments. Currently the material

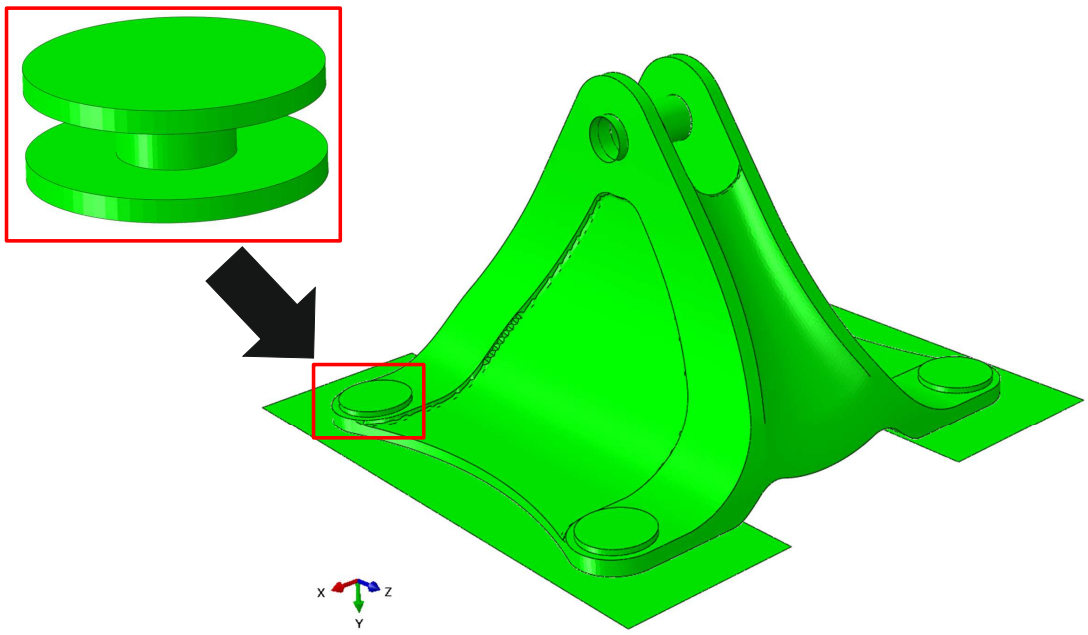

Figure 5.11: Assembly of the FE simulation of the bracket.

properties are being calibrated to match the experimental force vs displacement curves.

(a)

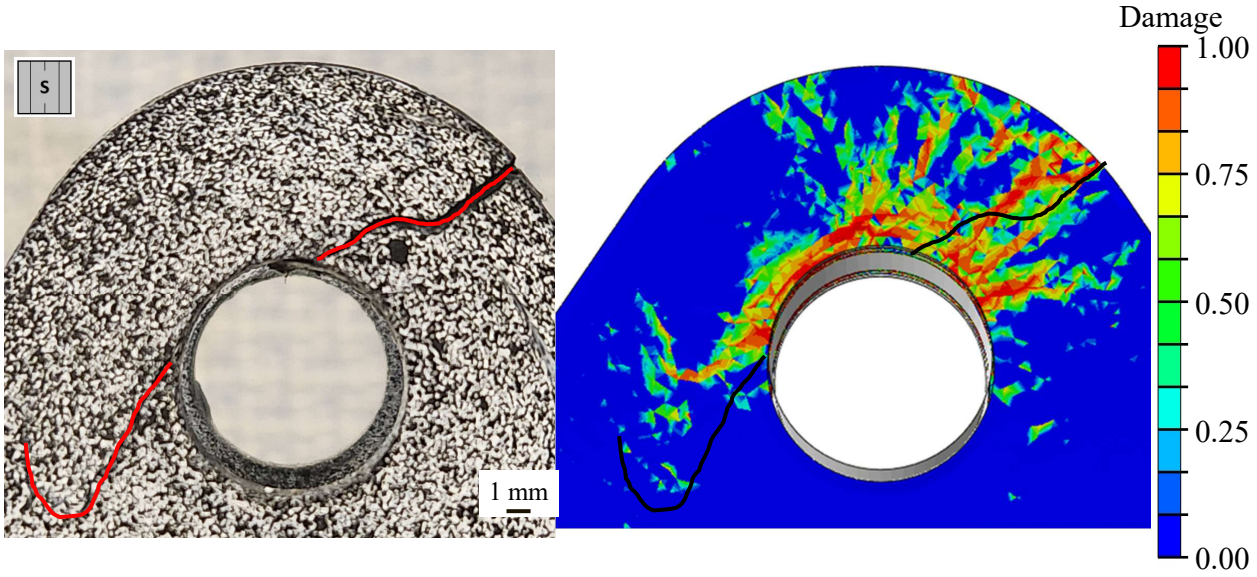

(b)

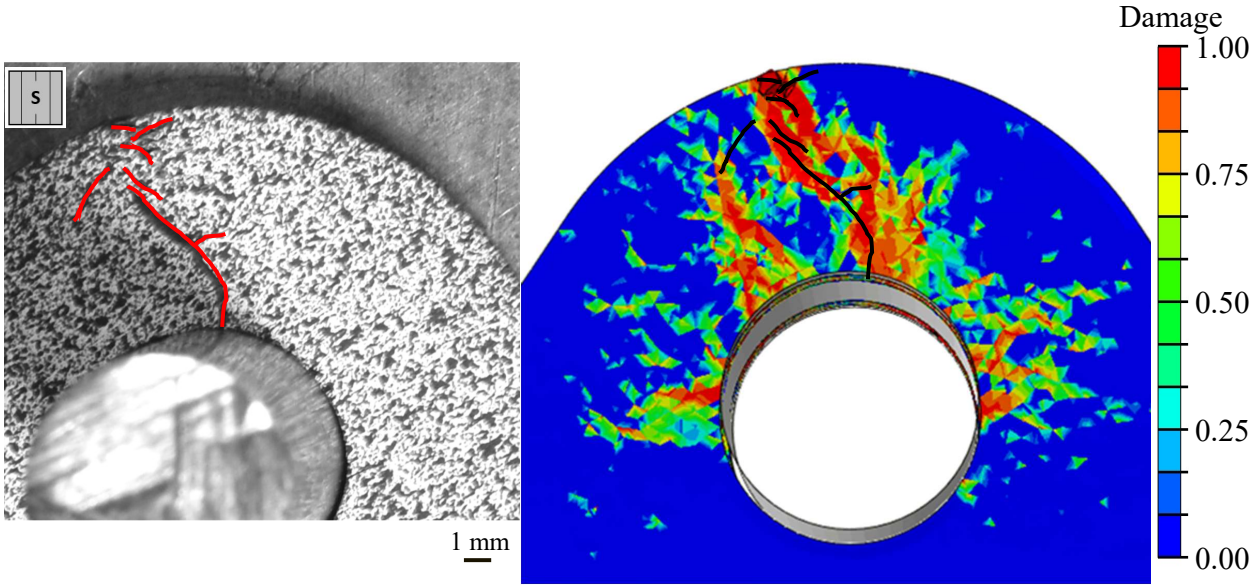

Figure 5.12: Fracture surface of the square platelet Sekisui bracket along side the contour plot of the matrix damage variable.

(a)

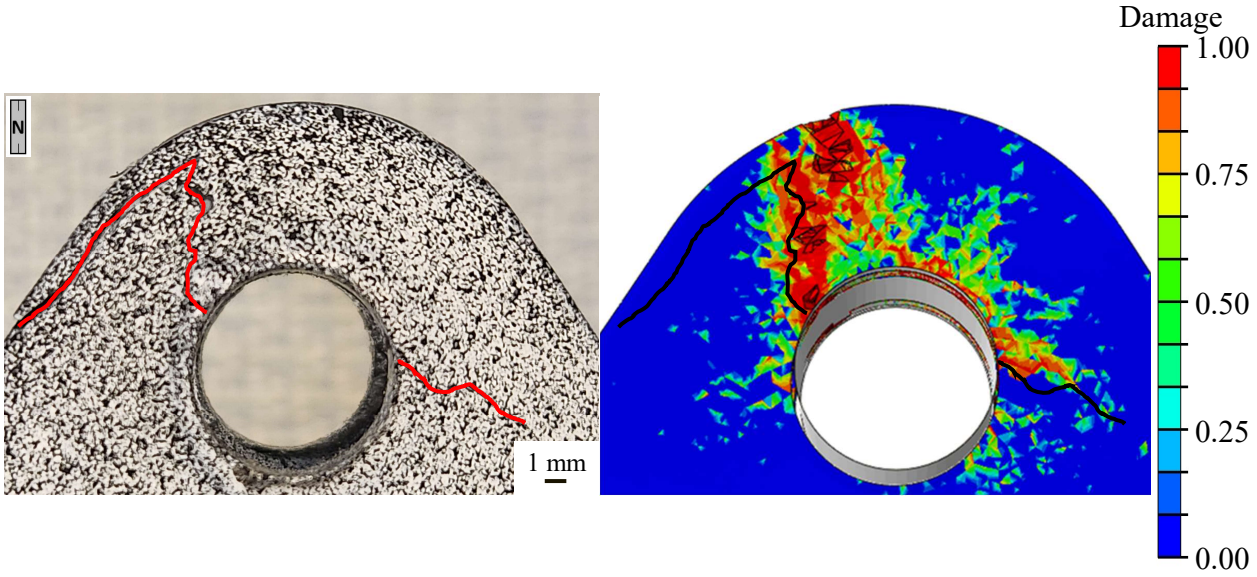

(b)

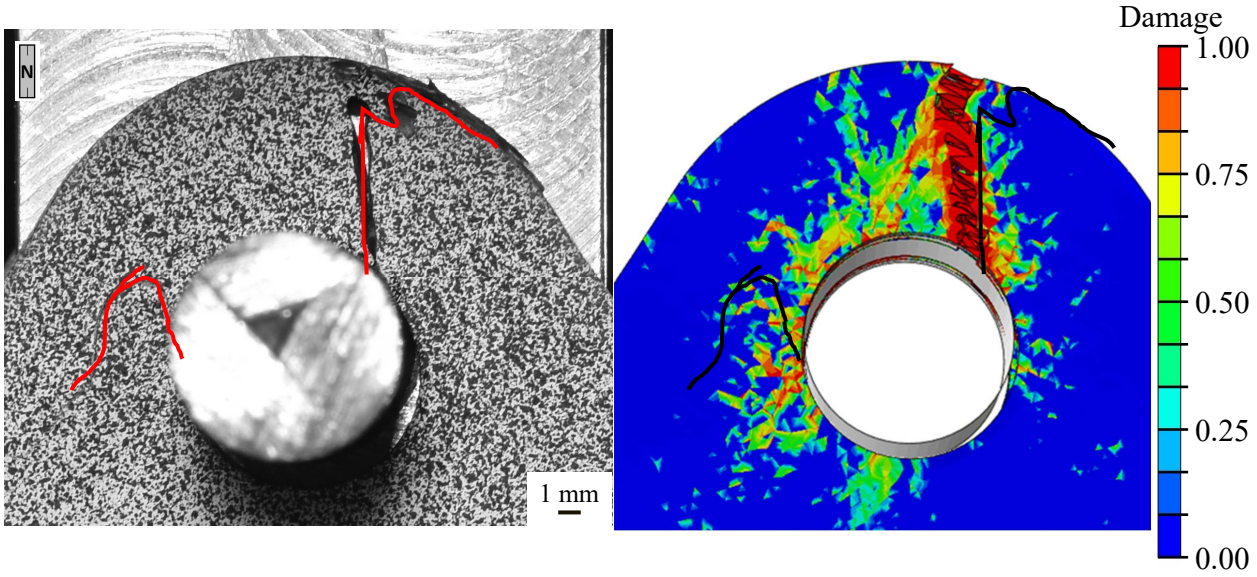

Figure 5.13: Fracture surface of the narrow platelet Sekisui bracket along side the contour plot of the matrix damage variable.

5.5 Conclusion

In this study, two platelets of varying widths were used to manufacture brackets. The brackets were tested in both tension and bending to obtain their mechanical performance. Before testing, a subset of these brackets were X-Ray μCT scanned to analyze the mesostructure of the brackets. From this the following conclusions can be made:

1. Sekisui brackets made with narrow platelets out performed the square platelet brackets. In tension the percent difference in stiffness and strength is about 31% and 38% respectively. In bending the percent difference in stiffness and strength is about 8% and 10% respectively.

2. When looking at the vector plots of the X-Ray μCT scans, it is evident that the fracture path, in both bending and tension, runs parallel to the fiber path. The fracture avoids fiber breakage and will follow the path of least resistance between platelets or between fibers within a platelet.

3. Due to flow, the top of the bracket has more voids than what is seen at the bottom of the bracket. On average, the void content is still low, but can be as high as 1.32%. However, the higher void content does not effect the mechanical performance of Discontinuous Fiber Composite (DFC) structures as much as with continuous fiber composite structures. This is evident by the fact that even though the narrow platelet brackets have a higher void content, they still out perform the square platelet ones. In any case, some care can be taken when fill the mold to mitigate void formation due to flow.

4. Some preliminary simulations have been performed by creating a digital twin of the Sekisui brackets. The digital twins match the fracture patterns seen in experiments and work is being done to match the stiffness and strength of the brackets.

5. This works showcases the viability to use DFCs to manufacture parts with complex geometries, like brackets. When manufacturing parts with DFCs careful consideration

needs to be done with platelet geometry and mold design. One can design a mold that will induce flow, to bias the orientation of platelets to the loading direction, but voids can form because of this. However, this is not a problem with void content close to 1%, as seen in this work. With the current study it is seen that DFCs are a great option to manufacture complex, light weight parts.

Chapter 6

CONCLUSIONS AND FUTURE WORKS

6.1 Conclusions

In this study, various aspects of Discontinuous Fiber Composites (DFCs) were investigated. Prepreg was aged to 84 days (3× the out life of the prepreg), and the mechanical and fracture properties were investigated. Then, platelet size effect, coupon thickness effect, and the effects of adding continuous fiber plies to the outer surface of a DFC core was investigated. Thirdly, the effects of flow on the tensile properties of DFCs were studied. Finally, DFCs were used to manufacture a bracket and was tested under two loading conditions. Based on the results, the following conclusions are made:

1. The effects of prepreg age on the mechanical and fracture properties of DFCs were investigated. Even though the manufacturing process of all the DFC laminates were the same, there was an increase in thickness with age. This is due to the viscosity of the resin increasing with age. This also explains why there is an increase in void content. The tensile, compression, and shear moduli did not change with aging, however a strengthening was observed. This is due to the matrix plasticizing with age which allows for the matrix to absorb more energy and so the fibers can carry more load. At fist, the aging caused the fracture energy to decrease, indicating that the material was becoming more brittle. This was due to the thickness increase. Then at the final aging time, the fracture energy became higher than the unaged DFC specimen. This is due to the plasticization of the matrix. The plasticization and increase in thickness are dictating the fracture energy. Overall this work shows that DFCs are an excellent candidate to reduce prepreg waste. By using repurposed prepreg to make DFCs the mechanical performance is comparable or better than that of DFCs made with virgin

material. Using DFCs for repurposing will greatly reduce the environmental impact of using composites and also can make composites cheaper to use.

2. The effects of platelet length showed that using a longer platelet lead to an increase in the flexural modulus and strength. However, this also increases the Coefficient of Variation (CoV) of the flexure properties. There was little effect on the average flexure properties when increasing the thickness, however the CoV can be significantly decreased. By adding continuous fiber plies to the outer surfaces of a DFC core the flexure properties of the structure can be increased, but due to waviness of these plies caused by platelet motion during curing, the CoV may not decrease. By performing a precure routine or by adding woven fiber plies between the DFC core and the unidirectional (UD) ply, the waviness is mitigated and the CoV is reduced. Computational models were able to match the experimental modulus and its CoV for all DFC specimen in flexure. However, the assumptions made for the model results in the hybrid simulations not perfectly matching. This is due to the out-of-plane rotations of the platelets. The use of shell elements make it so that the platelets in the simulations have no out of plane orientations. However, from X-Ray μCT scans, the out-of-plane rotations of platelets can lead to platelets that are vertical through half the specimen thickness. This does not occur with DFC specimen.

3. Platelet width effects and flow effects on the tensile properties of DFCs were investigated. In low flow the narrow platelets outperformed the square platelets. However, the high flow specimen did not see the same difference between the two platelet sizes. Between the low and high flow specimen, the square platelets' modulus and strength improved due to the biased orientation caused by the flow. On the other hand, only the modulus improved for the narrow platelet specimen while the strength remained the same. This could be due to void formations, which was slightly higher in the narrow platelets than the square. Flow induced voids to form in the mesostructure. Low flow coupons had about a 0.1% void content for both platelet sizes, whereas the high flow

coupons had about a 1.3% void content. Additionally, the high flow coupons showed a spatial dependence on void content, where the lower half of the coupon, close to the inlet of the mold, had a lower void content than the upper half, close to the end of the mold. This is due to trapped air. A statistical analysis on the orientations found through X-Ray CT scanning was performed. A DFC specimen was split into six 1 inch Statistical Representative Volume Elements (SRVEs). The in-plane orientations of platelets was found to not change much along the length of the specimen, however the out-of-plane orientation aligns closer to the xy-plane at the center of the specimen than at the edges. This is due to turbulent flow at the beginning where platelets enter the mold, and at the end due to the edge of the mold. The in-plane orientation was also found to follow the sum of a Normal and Uniform distribution. By using the equations of the CDFs of these two distributions, the empirical CDF can be fitted. By using Latin Hypercube Sampling with the fitted CDFs, the mesostructure generated matches the CDF found through the CT scans.

4. Sekisui brackets made with narrow and square platelets were tested in tension and bending. The brackets made with narrow platelets out performed the square platelet brackets. The fracture path, in both bending and tension, runs parallel to the fiber path. The fracture avoids fiber breakage and will follow the path of least resistance between platelets or between fibers within a platelet. Due to flow, the top of the bracket has more voids than what is seen at the bottom of the bracket. However, the higher void content does not effect the mechanical performance of DFC structures as much as with continuous fiber composite structures. This is evident by the fact that even though the narrow platelet brackets have a higher void content, they still out perform the square platelet ones. In any case, some care can be taken when fill the mold to mitigate void formation due to flow. From a given X-Ray μCT data, a digital twin can be generate. Currently, simulations are able to match the fracture patterns seen in experiments and work is being done to match the stiffness and strength. This works showcases the

viability to use DFCs to manufacture parts with complex geometries, like brackets. When manufacturing parts with DFCs careful consideration needs to be done with platelet geometry and mold design. With the current study it is seen that DFCs are a great option to manufacture complex, light weight parts.

The mechanical behavior of DFCs were experimentally and numerically investigated. Extensive testing was performed to obtain the statistical distribution of the mechanical properties of DFCs. Computational tools were developed to predict the mechanical responses of DFCs. Having such tools will expand the applications of DFCs and minimize the unnecessary and costly physical tests. This study shows a thorough engineering methodology for characterizing DFC materials.

6.2 Future Works

Despite the comprehensive analysis conducted, there are many aspects of DFCs that still need to be investigated. The following list is the summary of possible future works:

1. We've discovered that the variability in the tensile modulus and strength of DFCs is influenced by the distribution of platelets at a local level. As a result, accurately matching this local platelet distribution holds the key to predicting the material properties of DFCs. This distribution can be determined either directly from X-ray μCT scans, or by indirectly fine-tuning meso-structures using extensive experimental data. Additionally, a suitable size for the statistically representative volume element (SRVE) is necessary. However, at present, we lack an analytical approach to determine the appropriate SRVE size. If we can establish the correct SRVE size and couple it with the local platelet orientation distribution obtained from CT scans, it becomes possible to comprehensively characterize the statistical variations in material properties, eliminating the need for physical testing of DFC coupons.

2. DFC structures find extensive use in various applications, particularly as connectors

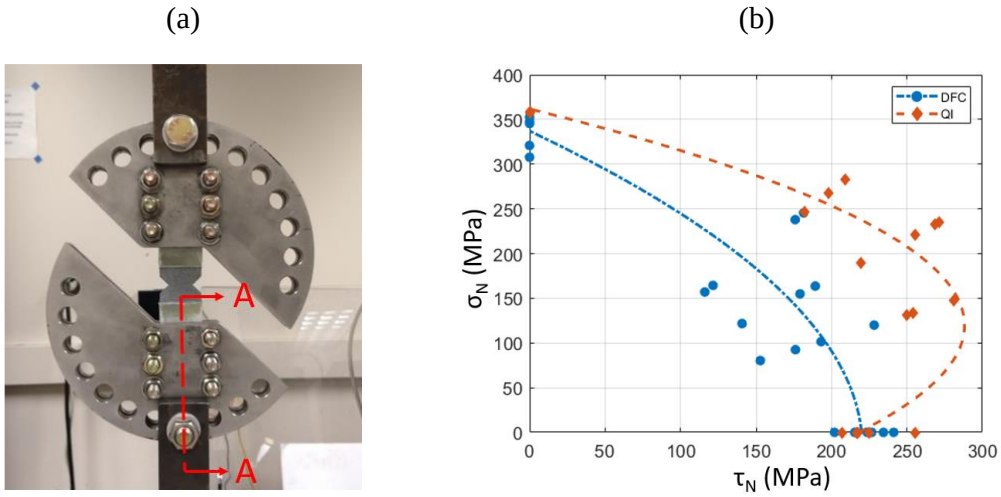

Figure 6.1: DFC double V-notch coupons were tested in the Arcan fixture setup as detailed by Nguyen [124]. The Arcan fixture links axial and shear loading through the utilization of pins. During testing, the positions of these pins were varied, ranging from conditions of pure tension to those of pure shear. The outcomes of these experiments are depicted in (b).

joining multiple components. In such scenarios, these structures often encounter complex multi-axial loading conditions. At the University of Washington, we have conducted thorough experimental and numerical investigations into how DFCs respond under these multi-axial loading conditions. The detailed study was documented by Nguyen [124]. To summarize, we employed the Arcan fixture depicted in Fig. 6.1a. This fixture enabled us to subject double V-notch DFC samples to combined tension and shear loads. The outcomes of the experiments are graphically represented in Fig. 6.1b. Notably, this study marks the first instance in the existing literature where the multi-axial fracturing behaviors of DFCs have been extensively explored. Our next step involves fine-tuning stochastic finite element models to accurately capture these distinctive behaviors, thereby facilitating the prediction of responses across various DFC meso-structures.

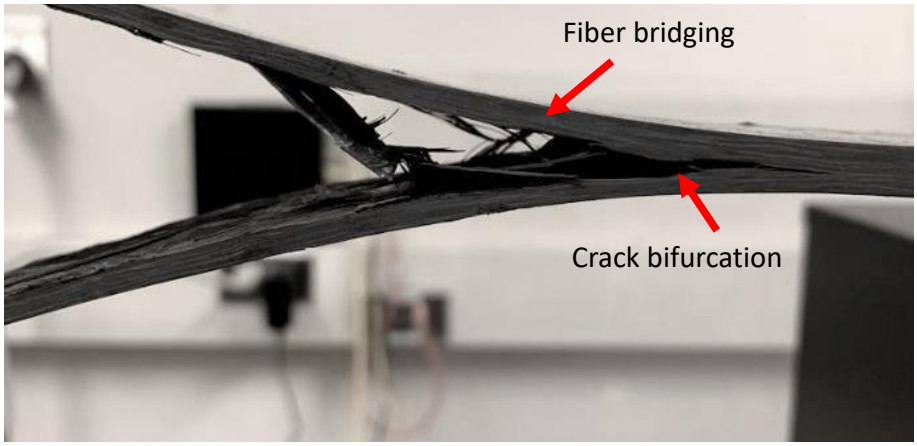

Figure 6.2: The fracture surfaces resulting from the double cantilever beam (DCB) test, as detailed by Tidwell [125]. When subjected to out-of-plane loading, DFCs exhibit considerably more intricate damage patterns compared to continuous fiber composites.

3. In addition to examining mode I intra-laminar fracture, we've also delved into mode I inter-laminar fracture through double cantilever beam tests. A comprehensive account of the experimental findings has been provided by Tidwell [125]. Due to the inherent randomness in platelet orientation, the fracture surfaces exhibit a notably higher degree of disorder compared to continuous fiber composites (as illustrated in Fig.6.2). Notably, certain test specimens displayed crack bifurcation, resulting in the emergence of two separate crack fronts stemming from a single crack tip. Consequently, the fracture energy observed in DFCs surpasses the reported values for continuous fiber composites by a substantial margin, ranging from 80% to 167% [125]. However, in order to comprehensively characterize the fracture energy, an exploration into the scaling effects within this failure mode is still required. Employing computational modeling becomes imperative to attain a comprehensive understanding of the intricate fracturing behaviors exhibited by this material.

BIBLIOGRAPHY

[1] Tushar Kanti Das, Prosenjit Ghosh, and Narayan Ch Das. Preparation, development, outcomes, and application versatility of carbon fiber-based polymer composites: a review. *Advanced Composites and Hybrid Materials*, pages 1–20, 2019.

[2] Charles E Harris, James H Starnes Jr, and Mark J Shuart. Design and manufacturing of aerospace composite structures, state-of-the-art assessment. *Journal of aircraft*, 39(4):545–560, 2002.

[3] Rozaini Othman, Noor Iswadi Ismail, MAAH Pahmi, Mahamad Hisyam Mahamad Basri, Hazim Sharudin, and Abdul Rahman Hemdi. Application of carbon fiber reinforced plastics in automotive industry: A review. *J. Mech. Manuf*, 1:144–154, 2018.

[4] S.D. Mazumdar, M. Pichler, W. Benevento, R. Seneviratine, and Witten E. State of the industry report. *Composites Manufacturing*, 2020.

[5] *American Composites Manufacturers Association (ACMA) website*, (visited: December 2021).

[6] A Baker, S Dutton, and D Kelly. *Composite Materials for Aircraft Structures*. American Institute of Aeronautics and Astronautics, 2004.

[7] A Rashidi and AS Milani. A multi-step biaxial bias extension test for wrinkling/dewrinkling characterization of woven fabrics: Towards optimum forming design guidelines. *Materials & Design*, 146:273–285, 2018.

[8] P Wang, X Legrand, P Boisse, N Hamila, and D Soulat. Experimental and numerical analyses of manufacturing process of a composite square box part: Comparison between textile reinforcement forming and surface 3d weaving. *Composites Part B: Engineering*, 78:26–34, 2015.

[9] Composite Recycling Technology Center, (CRTC), 2021.

[10] M Selezneva and L Lessard. Characterization of mechanical properties of randomly oriented strand thermoplastic composites. *Journal of composite materials*, 50(20):2833–2851, 2016.

[11] BR Denos, DE Sommer, AJ Favaloro, RB Pipes, and WB Avery. Fiber orientation measurement from mesoscale ct scans of prepreg platelet molded composites. *Composites Part A: Applied Science and Manufacturing*, 114:241–249, 2018.

[12] Y Wan and J Takahashi. Tensile and compressive properties of chopped carbon fiber tapes reinforced thermoplastics with different fiber lengths and molding pressures. *Composites Part A: Applied Science and Manufacturing*, 87:271–281, 2016.

[13] Z Chen, T Huang, Y Shao, Y Li, H Xu, K Avery, D Zeng, W Chen, and X Su. Multiscale finite element modeling of sheet molding compound (smc) composite structure based on stochastic mesostructure reconstruction. *Composite Structures*, 188:25–38, 2018.

[14] Hexcel, Stamford, CT. https://www.hexcel.com/Products/HexMC-Materials-for-Industries.

[15] Moore S. SMC adopted for rear door frame of Toyota's new Prius PHV, Plastics Today, 3 April 2017 https://www.plasticstoday.com/automotive-and-mobility/smc-adopted-rear-door-frame-toyota-s-new-prius-phv/163725208056557.

[16] Mitsubishi Chemical Corporation, Irvine, CA. https://www.m-chemical.co.jp/carbon-fiber/en/case/car/.

[17] P Feraboli, F Gasco, B Wade, S Maier, R Kwan, W Salmon, A Masini, L DeOto, and ML Reggiani. Forged compositer" technology for the suspension arms of the sesto elemento. In *ASC 26rd Annual technical conference. Montreal*, 2011.

[18] S Black. Military oem makes the switch from sandwich construction to compression molding to optimize composite aerospace part. *High Perf Compos*, 2012.

[19] G Nilakantan and S Nutt. Reuse and upcycling of thermoset prepreg scrap: Case study with out-of-autoclave carbon fiber/epoxy prepreg. *Journal of composite materials*, 52(3):341–360, 2018.

[20] Sanzida Sultana, Amir Asadi, Jonathan Colton, and Kyriaki Kalaitzidou. Composites made from cf prepreg trim waste tapes using sheet molding compounds (smc) technology: Challenges and potential. *Composites Part A: Applied Science and Manufacturing*, 134:105906, 2020.

[21] Pete George, Benjamin Rutz, Felix Nguyen, and Toshiya Kamae. High performance, low cost, discontinuous fiber molding compound based on reclaimed carbon fiber-epoxy prepreg. *CAMX 2019-Composites and Advanced Materials Expo*, 2019.

[22] Troy Nakagawa, Seunghyun Ko, Cory Slaughter, Talal Abdullah, Guy Houser, and Marco Salviato. Effects of aging on the mechanical and fracture properties of chopped fiber composites made from repurposed aerospace prepreg scrap and waste. *Sustainable Materials and Technologies*, 33:e00470, 2022.

[23] *Composite Materials Handbook, Volume 3 - Polymer Matrix Composites - Materials Usage, Design, and Analysis (CMH-17) Chapter 18 Environmental Management*. SAE International on behalf of CMH-17, a division of Wichita State University, 2012.

[24] M Turtle, T Shifman, and B Boursier. Simplifying certification of discontinuous composite material forms primary aircraft structures. *Hexcel research and technology*, 2010.

[25] Quantum Composites, Bay City, MI. https://www.quantumcomposites.com/applications/lamborghini.

[26] Y Pan, L Iorga, and A Pelegri. Numerical generation of a random chopped fiber composite rve and its elastic properties. *Compos Sci and Tech*, 68:2792–2798, 2008.

[27] SB Visweswaraiah, M Selezneva, L Lessard, and P Hubert. Mechanical characterisation and modelling of randomly oriented strand architecture and their hybrids–a general review. *Journal of Reinforced Plastics and Composites*, 37(8):548–580, 2018.

[28] P Feraboli, E Peitso, F Deleo, T Cleveland, and PB Stickler. Characterization of prepreg-based discontinuous carbon fiber/epoxy systems. *Journal of reinforced plastics and composites*, 28(10):1191–1214, 2009.

[29] SG Kravchenko, DE Sommer, BR Denos, AJ Favaloro, CM Tow, WB Avery, and B Pipes. Tensile properties of a stochastic prepreg platelet molded composite. *Composites Part A: Applied Science and Manufacturing*, 124:105507, 2019.

[30] SG Kravchenko, DE Sommer, BR Denos, WB Avery, and B Pipes. Structure-property relationship for a prepreg platelet molded composite with engineered meso-morphology. *Composite Structures*, 210:430–445, 2019.

[31] DE Sommer, SG Kravchenko, BR Denos, AJ Favaloro, and RB Pipes. Integrative analysis for prediction of process-induced, orientation-dependent tensile properties in a stochastic prepreg platelet molded composite. *Composites Part A: Applied Science and Manufacturing*, 130:105759, 2020.

[32] H Tang, Z Chen, G Zhou, Y Li, K Avery, H Guo, H Kang, D Zeng, and X Su. Correlation between failure and local material property in chopped carbon fiber chip-reinforced sheet molding compound composites under tensile load. *Polymer Composites*, 40(S2):E962–E974, 2019.

[33] Z Chen, H Tang, Y Shao, Q Sun, G Zhou, Y Li, H Xu, D Zeng, and X Su. Failure of chopped carbon fiber sheet molding compound (smc) composites under uniaxial tensile loading: Computational prediction and experimental analysis. *Composites Part A: Applied Science and Manufacturing*, 118:117–130, 2019.

[34] S Ko, J Yang, ME Tuttle, and M Salviato. Effect of the platelet size on the fracturing behavior and size effect of discontinuous fiber composite structures. *Composite Structures*, 227:111245, 2019.

[35] S Ko, J Davey, S Douglass, J Yang, ME Tuttle, and M Salviato. Effect of the thickness on the fracturing behavior of discontinuous fiber composite structures. *Composites Part A: Applied Science and Manufacturing*, 125:105520, 2019.

[36] Y Li, S Pimenta, J Singgih, S Nothdurfter, and K Schuffenhauer. Experimental investigation of randomly-oriented tow-based discontinuous composites and their equivalent laminates. *Composites Part A: Applied Science and Manufacturing*, 102:64–75, 2017.

[37] M Alves, D Carlstedt, F Ohlsson, LE Asp, and S Pimenta. Ultra-strong and stiff randomly-oriented discontinuous composites: Closing the gap to quasi-isotropic continuous-fibre laminates. *Composites Part A: Applied Science and Manufacturing*, 132:105826, 2020.

[38] DM Corbridge, Lee Thomas Harper, Davide SA De Focatiis, and NA Warrior. Compression moulding of composites with hybrid fibre architectures. *Compos Part A*, 95:87–99, 2017.

[39] SR Naqvi, H Mysore Prabhakara, EA Bramer, W Dierkes, R Akkerman, and G Brem. A critical review on recycling of end-of-life carbon fibre/glass fibre reinforced composites waste using pyrolysis towards a circular economy. *Resources, conservation and recycling*, 136:118–129, 2018.

[40] Yijia Ma and Steven Nutt. Chemical treatment for recycling of amine/epoxy composites at atmospheric pressure. *Polymer degradation and stability*, 153:307–317, 2018.

[41] Xiao Kuang, Yunying Zhou, Qian Shi, Tiejun Wang, and H Jerry Qi. Recycling of epoxy thermoset and composites via good solvent assisted and small molecules participated exchange reactions. *ACS Sustainable Chemistry & Engineering*, 6(7):9189–9197, 2018.

[42] Stephen J Pickering. Recycling technologies for thermoset composite materials—current status. *Composites Part A: applied science and manufacturing*, 37(8):1206–1215, 2006.

[43] Vannessa Goodship. *Management, recycling and reuse of waste composites*. CRC Press, Boca Raton, FL, USA, 2009.

[44] Robert A Witik, Remy Teuscher, Véronique Michaud, Christian Ludwig, and Jan-Anders E Månson. Carbon fibre reinforced composite waste: an environmental assessment of recycling, energy recovery and landfilling. *Composites Part A: Applied Science and Manufacturing*, 49:89–99, 2013.

[45] I Bianchi, A Forcellese, Marco Marconi, M Simoncini, A Vita, and V Castorani. Environmental impact assessment of zero waste approach for carbon fiber prepreg scraps. *Sustainable Materials and Technologies*, 29:e00308, 2021.

[46] SANZIDA SULTANA, PETE GEORGE, JONATHAN COLTON, and KYRIAKI KALAITZIDOU. A novel and sustainable approach to recycle prepreg trim waste via sheet molding compound (smc) technique. In *Proceedings of the American Society for Composites—Thirty-third Technical Conference*, 2018.

[47] ASTM D4332-14. Standard practice for conditioning containers, packages, or packaging components for testing. *ASTM International*, 2015.

[48] S Ko, K Chan, R Hawkins, R Jayaram, C Lynch, R El Mamoune, M Nguyen, N Pekhotin, N Stokes, D Wu, J Yang, ME Tuttle, and M Salviato. Characterization and computational modeling of the fracturing behavior in discontinuous fiber composite structures. In *SAMPE Conference. Long Beach, CA.*, 2018.

[49] ASTM D3418-15. Sstandard test method for transition temperatures and enthalpies of fusion and crystallization of polymers by differential scanning calorimetry. *ASTM International*, 2015.

[50] *ASTM E1356-08. Standard test method for assignment of the glass transition temperatures by differential scanning calorimetry.* West Conshohocken, PA, 2014.

[51] The MathWorks, Inc., "Matlab 2019b," The MathWorks, Inc., Natick, MA, 2019.

[52] GOM, Braunschweig, Germany. https://www.gom.com.

[53] *ASTM D1356-17. Standard test method for tensile properties of polymer matrix composite materials.* West Conshohocken, PA, 2017.

[54] *ASTM D3410-16. Standard test method for compressive properties of polymer matrix composite materials with unsupported gage section by shear loading.* West Conshohocken, PA, 2016.

[55] *ASTM D5379-12. Standard test method for shear properties of composite materials by the v-notch beam method*. West Conshohocken, PA, 2012.

[56] M Salviato, K Kirane, ZP Bažant, and G Cusatis. Experimental and numerical investigation of intra-laminar size effect in textile composites. *Comps Sci Technol*, 135:67–75, 2016.

[57] Zdenek P Bažant, Jia-Liang Le, and Marco Salviato. *Quasibrittle Fracture Mechanics and Size Effect: A First Course*. Oxford University Press, 2021.

[58] Zdeněk P Bažant. Scaling theory for quasibrittle structural failure. *Proceedings of the National Academy of Sciences*, 101(37):13400–13407, 2004.

[59] Weixin Li, Yao Qiao, Joel Fenner, Kyle Warren, Marco Salviato, Zdeněk P Bažant, and Gianluca Cusatis. Elastic and fracture behavior of three-dimensional ply-to-ply angle interlock woven composites: Through-thickness, size effect, and multiaxial tests. *Composites Part C: Open Access*, 4:100098, 2021.

[60] Marco Salviato, Kedar Kirane, Zdeněk P Bažant, and Gianluca Cusatis. Mode I and II interlaminar fracture in laminated composites: a size effect study. *Journal of Applied Mechanics*, 86(9), 2019.

[61] Marco Salviato, Shiva Esna Ashari, and Gianluca Cusatis. Spectral stiffness microplane model for damage and fracture of textile composites. *Composite Structures*, 137:170–184, 2016.

[62] Yao Qiao and Marco Salviato. Strength and cohesive behavior of thermoset polymers at the microscale: A size-effect study. *Engineering Fracture Mechanics*, 213:100–117, 2019.

[63] Cory Hage Mefford, Yao Qiao, and Marco Salviato. Failure behavior and scaling of graphene nanocomposites. *Composite Structures*, 176:961–972, 2017.

[64] Yao Qiao and Marco Salviato. Study of the fracturing behavior of thermoset polymer nanocomposites via cohesive zone modeling. *Composite Structures*, 220:127–147, 2019.

[65] Zdenek P Bazant, Phillip A Pfeiffer, et al. Determination of fracture energy from size effect and brittleness number. *ACI Materials Journal*, 84(6):463–480, 1987.

[66] Christian Carloni, Gianluca Cusatis, Marco Salviato, Jia-Liang Le, Christian G Hoover, and Zdeněk P Bažant. Critical comparison of the boundary effect model with cohesive crack model and size effect law. *Engineering Fracture Mechanics*, 215:193–210, 2019.

[67] Hoang T Nguyen, A Abdullah Dönmez, and Zdeněk P Bažant. Structural strength scaling law for fracture of plastic-hardening metals and testing of fracture properties. *Extreme Mechanics Letters*, 43:101141, 2021.

[68] GR Irwin. *Fracture Handbuch der Physik vol. 6*. Springer, 1958.

[69] Jaime Planas and Zdenek P. Bazant. *Fracture and size effect in concrete and other quasibrittle materials*. CRC Press, 1998.

[70] Zdeněk P Bažant. Size effect in blunt fracture: concrete, rock, metal. *Journal of engineering mechanics*, 110(4):518–535, 1984.

[71] M Selezneva, S Roy, S Meldrum, L Lessard, and A Yousefpour. Modelling of mechanical properties of randomly oriented strand thermoplastic composites. *Journal of Composite Materials*, 51(6):831–845, 2017.

[72] P Feraboli, T Cleveland, P Stickler, and JC Halpin. Stochastic laminate analogy for simulating the variability in modulus of discontinuous composite materials. *Composites Part A: Applied Science and Manufacturing*, 41(4):557–570, 2010.

[73] K Harban and ME Tuttle. Reducing certification costs of discontinuous fiber composite structures via stochastic modeling. *US Dept. of Transportation FAA*, 2017.

[74] S Ko, J Yang, ME Tuttle, and M Salviato. Stochastic computational modeling of the fracturing behavior in discontinuous fiber composite structures. In *SAMPE Conference. Virtual*, 2020.

[75] S Ko, T Nakagawa, Z Chen, J Davey, T Abdullah, L Kuklenski, E Adams, M Soja, C Park, W Avery, J Yang, and M Salviato. Experimental and numerical investigations of stochastic thickness effects in discontinuous fiber composites. In *American Society of Composites Conference. Virtual*, 2021.

[76] Dassault Systemes ABAQUS. ABAQUS Documentation, Providence, RI. 2021.

[77] JR Rice. A path independent integral and the approximate analysis of strain concentrations by notches and cracks. *J Appl Mech ASME*, 35:379–86, 1969.

[78] David Blass, Stefan Kreling, and Klaus Dilger. The impact of prepreg aging on its processability and the postcure mechanical properties of epoxy-based carbon-fiber reinforced plastics. *P I MECH ENG L-J MAT*, 231:62–72, 2017.

[79] SG Miller, JK Sutter, DA Scheiman, M Maryanski, and M Schlea. Study of out-time on the processing and properties if im7/977-3 composites. *SAMPE conference*, 2010.

[80] LK Grunenfelder and SR Nutt. Prepreg age monitoring via differential scanning calorimetry. *J Reinf Plast Comp*, 31:295–302, 2012.

[81] D Kim, T Centea, and ST Nutt. Modelling and monitoring of out-time and moisture absorption effects on cure kinetics and viscosity for an out-of-autoclave (OoA) prepreg. *Compos Sci Technol*, 138:200–208, 2017.

[82] KC Cole, D Noël, and JJ Hechler. Room temperature aging of narmco 5208 carbon-epoxy prepreg. part i: physicochemical characterization. *Polym Composite*, 10:150–161, 1989.

[83] D Scola and J Vontell. Effects of ambient aging of 5245C/graphite prepreg on composition and mechanical properties of fabricated composites. *Polym Composite*, 8:244–252, 1987.

[84] D Kim, T Centea, and SR Nutt. Effect of room-temperature out-time on tow impregnation in an out-of-autoclave prepreg. *Compos Part A*, 45:119–216, 2013.

[85] P Feraboli, E Peitso, T Cleveland, and PB Stickler. Modulus measurement for prepreg-based discontinuous carbon fiber/epoxy systems. *Journal of composite materials*, 43(19):1947–1965, 2009.

[86] S Yamashita, K Hashimoto, H Suganuma, and J Takahashi. Experimental characterization of the tensile failure mode of ultra-thin chopped carbon fiber tape-reinforced thermoplastics. *Journal of Reinforced Plastics and Composites*, 35(18):1342–1352, 2016.

[87] RW Jones, Y Ng, and JF McClelland. Monitoring ambient-temperature aging of a carbon-fiber/epoxy composite prepreg with photoacoustic spectroscopy. *Compos Part A*, 29:965–971, 2008.

[88] KC Cole, D Noël, JJ Hechler, P Cielo, and JC Krapez. Room temperature aging of Narmco 5208 carbon-epoxy prepreg. part ii: physical, mechanical, and nondestructive characterization. *Polym Composite*, 12:203–212, 1991.

[89] C Schmidt, P Weber, T Hocke, and B Denkena. Influence of prepreg material quality on carbon fiber reinforced plastic laminates processed by automated fiber placement. *11th CIRP Conference*, 2017.

[90] M Akay. Effects of prepreg ageing and post-cure hygrothermal conditioning on the mechanical behaviour of carbon fibre/epoxy laminates. *Compos Sci Technol*, 38:359–370, 1990.

[91] J Zhou and J.P. Lucas. Hygrothermal effects of epoxy resin. part I: the nature of water in epoxy. *Polymer*, 40:5505–5512, 1999.

[92] L.E Asp. The effects of moisture and temperature on the interlaminar delamination toughness of a carbon/epoxy composite. *Compos Sci and Tech*, 58:967–977, 1998.

[93] N Sharp. *Effects of moisture on the properties of epoxies and carbon-epoxy composite laminates*. PhD thesis, Purdue University, 2015. (Publication No. 3734368).

[94] P Feraboli, E Peitso, T Cleveland, PB Stickler, and JC Halpin. Notched behavior of prepreg-based discontinuous carbon fiber/epoxy systems. *Composites Part A: Applied Science and Manufacturing*, 40(3):289–299, 2009.

[95] C Qian, LT Harper, TA Turner, and NA Warrior. Notched behaviour of discontinuous carbon fibre composites: comparison with quasi-isotropic non-crimp fabric. *Compos Part A*, 42:293–302, 2011.

[96] *Composite Materials Handbook, Volume 1 - Polymer Matrix Composites - Guidelines for Characterization of Structural Materials (CMH-17) Chapter 8 Statistical Methods*. SAE International on behalf of CMH-17, a division of Wichita State University, 2012.

[97] Key Technology A Duravant Company, Walla Walla, WA. https://www.key.net/.

[98] Sekisui aerospace corporation, Renton, WA. https://www.sekisuiaerospace.com/.

[99] Siavash Sattar, Benjamin Beltran Laredo, Sergii G Kravchenko, and Oleksandr G Kravchenko. Effect of platelet length and stochastic morphology on flexural behavior of prepreg platelet molded composites. *Polymer Composites*, 2023.

[100] Richard Larson, Von C Jamora, Siavash Sattar, Sergii G Kravchenko, and Oleksandr G Kravchenko. Role of discontinuous fiber core material on the mechanical behavior of hybrid sandwich polyester composites. *Journal of Reinforced Plastics and Composites*, page 07316844221145559, 2022.

[101] Yuto Nakashima, Shinichiro Yamashita, Xin Zhang, Hirofumi Suganuma, and Jun Takahashi. Analytical modelling of the behaviour and scatter of the flexural modulus of randomly oriented carbon fibre strand thermoplastic composites. *Composite Structures*, 178:217–224, 2017.

[102] ASTM D790-17. Standard test method for flexural properties of polymer matrix composite materials. *ASTM International*, 2017.

[103] ASTM D7264-15. Standard test method for flexural properties of unreinforced and reinforced plastics and electrical insulating materials. *ASTM International*, 2015.

[104] *North Star Imaging. https://4nsi.com/; 2021.*

[105] G Cai, T Shirai, Y Wan, K Uzawa, and J Takahashi. Application of x-ray computed tomography to measuring fiber orientation distribution of chopped carbon fiber tape reinforced thermoplastics. *Applied Composite Materials*, 28(2):573–586, 2021.

[106] SG Advani and CL Tucker. The use of tensors to describe and predict fiber orientation in short fiber composites. *Journal of Rheology*, 31(8):751–784, 1987.

[107] Randy S Bay and Charles L Tucker III. Stereological measurement and error estimates for three-dimensional fiber orientation. *Polymer Engineering & Science*, 32(4):240–253, 1992.

[108] S Ko, J Yang, ME Tuttle, and M Salviato. Fracturing behavior and size effect of discontinuous fiber composite structures with different platelet sizes. 2018. Available from: ArXiv:1812.08312.

[109] AD Evans, CC Qian, TA Turner, LT Harper, and NA Warrior. Flow characteristics of carbon fibre moulding compounds. *Composites Part A: Applied Science and Manufacturing*, 90:1–12, 2016.

[110] Linda G Shapiro and George C Stockman. *Computer Vision*. Pearson, 2011.

[111] S Ko, K Chan, R Hawkins, R Jayaram, C Lynch, R El Mamoune, M Nguyen, N Pekhotin, N Stokes, D Wu, J Yang, ME Tuttle, and M Salviato. Experimental and numerical characterization of the intra-laminar fracturing behavior in discontinuous fiber composite structures. In *Proceedings of the 33th ASC Conference, Seattle, WA, USA*, pages 24–26, 2018.

[112] P Boisse, J Colmars, N Hamila, N Naouar, and Q Steer. Bending and wrinkling of composite fiber preforms and prepregs. a review and new developments in the draping simulations. *Composites Part B: Engineering*, 141:234–249, 2018.

[113] Xiangqian Li, Stephen R Hallett, and Michael R Wisnom. Modelling the effect of gaps and overlaps in automated fibre placement (afp)-manufactured laminates. *Science and Engineering of Composite Materials*, 22(2):115–129, 2015.

[114] J Aubry. Hexmc—bridging the gap between prepreg and smc. *Reinforced Plastics*, 45(6):38–40, 2001.

[115] AJ Favaloro, DE Sommer, BR Denos, and RB Pipes. Simulation of prepreg platelet compression molding: Method and orientation validation. *Journal of Rheology*, 62(6):1443–1455, 2018.

[116] Jan Teuwsen, Stephan K Hohn, and Tim A Osswald. Direct fiber simulation of a compression molded ribbed structure made of a sheet molding compound with randomly oriented carbon/epoxy prepreg strands—a comparison of predicted fiber orientations with computed tomography analyses. *Journal of Composites Science*, 4(4):164, 2020.

[117] Shinya Hayashi, Hao Chen, and Wei Hu. Development of new simulation technology for compression molding of long fiber reinforced plastics. In *Proceedings of the 15th International LS-DYNA® Users Conference, Detroit, MI, USA*, pages 10–12, 2018.

[118] DREW E SOMMER, ANTHONY J FAVALORO, SERGII G KRAVCHENKO, BENJAMIN R DENOS, and R BYRON PIPES. Stochastic process modeling of a prepreg platelet molded composite bracket. In *Proceedings of the American Society for Composites â€" Thirty-third Technical Conference*, 2018.

[119] E Barocio, M Eichenhofer, J Kalman, LM Fjeld, J Kirchhoff, G Kim, and R Byron Pipes. Compression molding of hybrid continuous and discontinuous fiber reinforced thermoplastics for enhancing strength characteristics. In *SAMPE Conference*, 2023.

[120] Correlated Solutions, Columbia, SC. https://www.correlatedsolutions.com/.

[121] Dragonfly, Object Research Systems (ORS) Inc, Montreal, Canada. http://www.theobjects.com/dragonfly.

[122] Siemens Digital Industries Software, Plano, TX, USA. https://plm.sw.siemens.com/en-US/simcenter/mechanical-simulation/femap/; 2022.

[123] Z Hashin. Failure criteria for unidirectional fiber composites. *J Appl Mech*, 47:329–34, 1980.

[124] M Nguyen. *Experimental and Numerical Investigation of the Mechanical Behavior of Discontinuous Fiber Composite Structures Under Multi-Axial Loading*. University of Washington, 2020.

[125] Kathryn Tidwell. *Investigating the Fracture Behavior and Damage Mechanisms of Discontinuous Fiber Composites Under Significant Out-of-plane Loading*. University of Washington, 2020.

Appendix A

BRACKET X-RAY μCT PLOTS

Below are various plots of orientations found through X-Ray μCT with the fracture surfaces from tests done on the Sekisui breackets in chapter 5. Figures A.1 and A.2 show the contour plots of the orientation tensor with the fracture of the brackets in tension. Figures A.3 and A.4 show the vector plots of the fiber orientation with the fracture of the brackets in tension. Figures A.5 and A.6 show the vector plots of the fiber orientation with the fracture of the brackets in bending.

a) Square Platelet Tension Failure 1

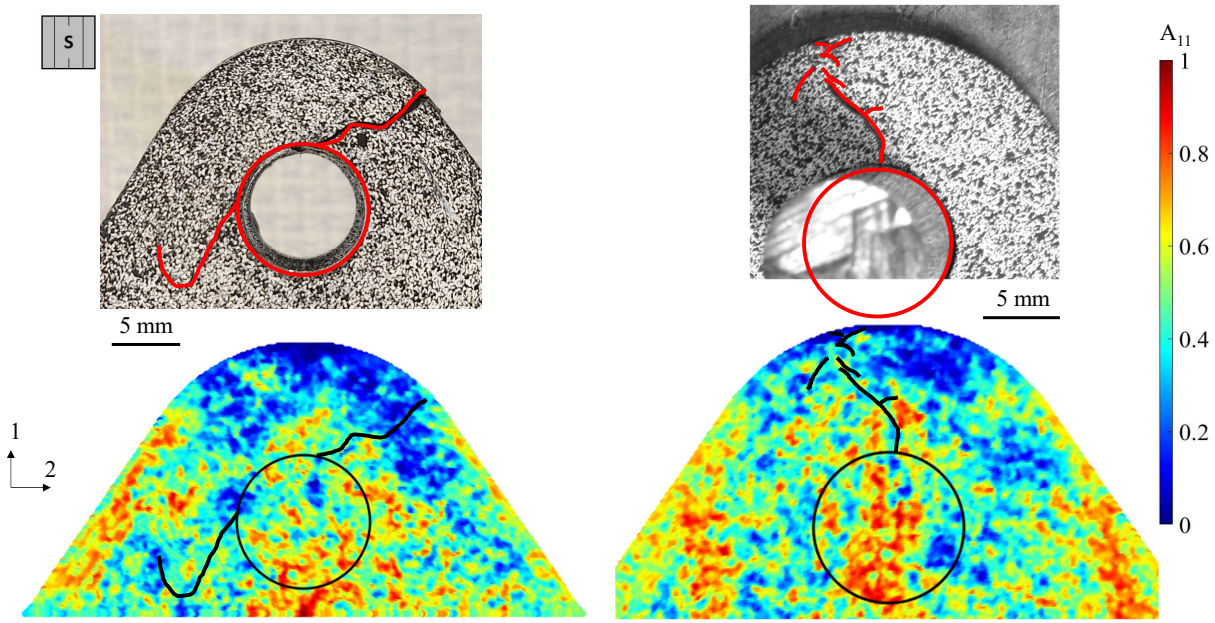

b) Square Platelet Tension Failure 2

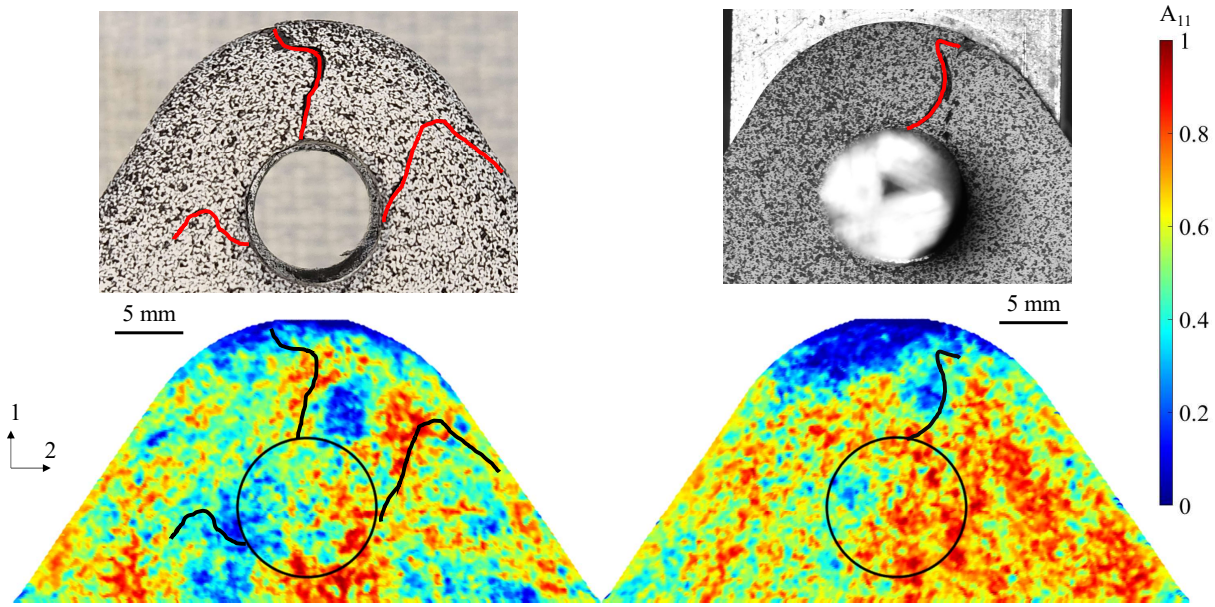

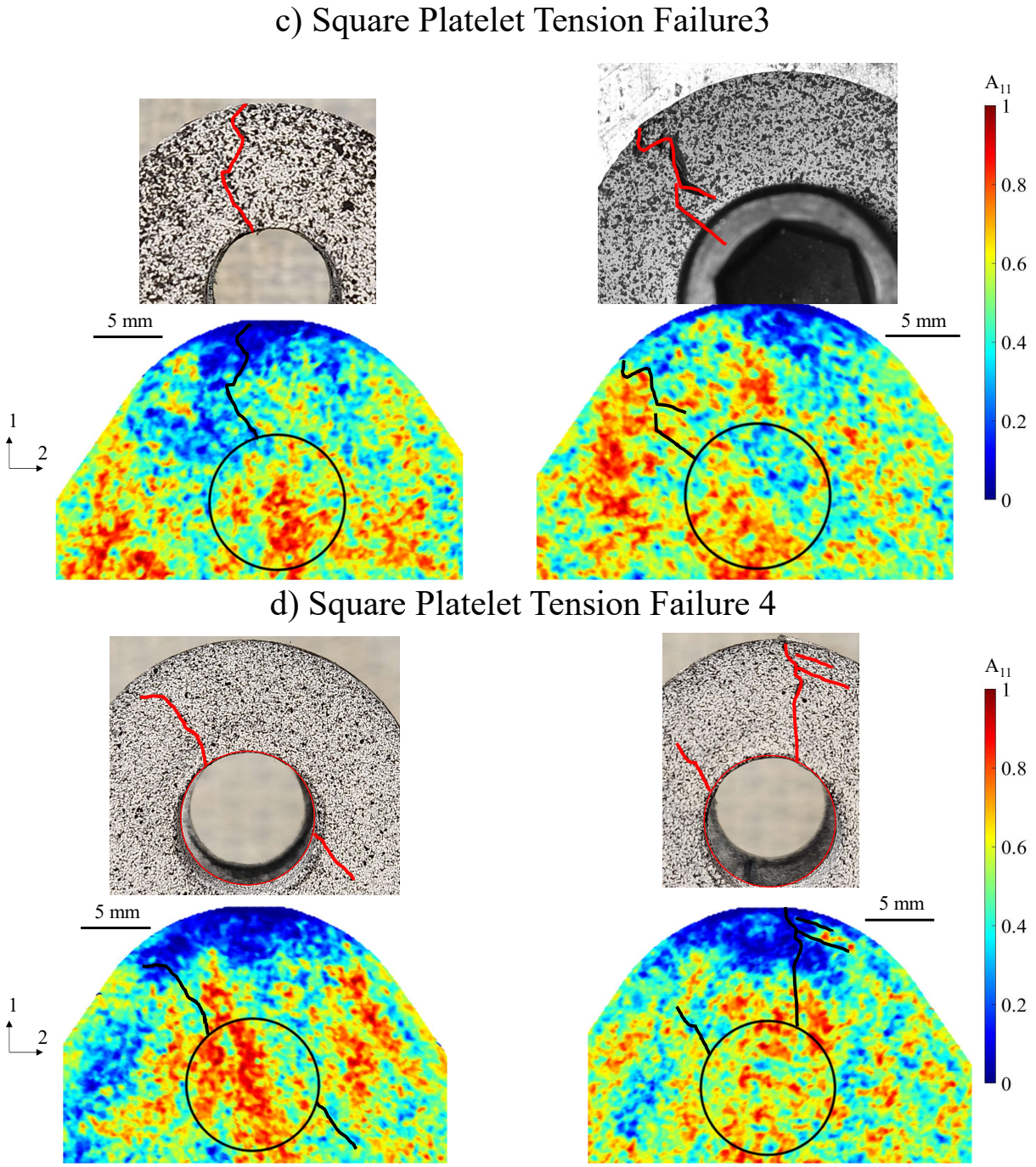

Figure A.1: Contour plots of square platelet Sekisui brackets of the orientation tensor component corresponding to the 1 direction with the fracture path in tension.

a) Narrow Platelet Tension Failure 1

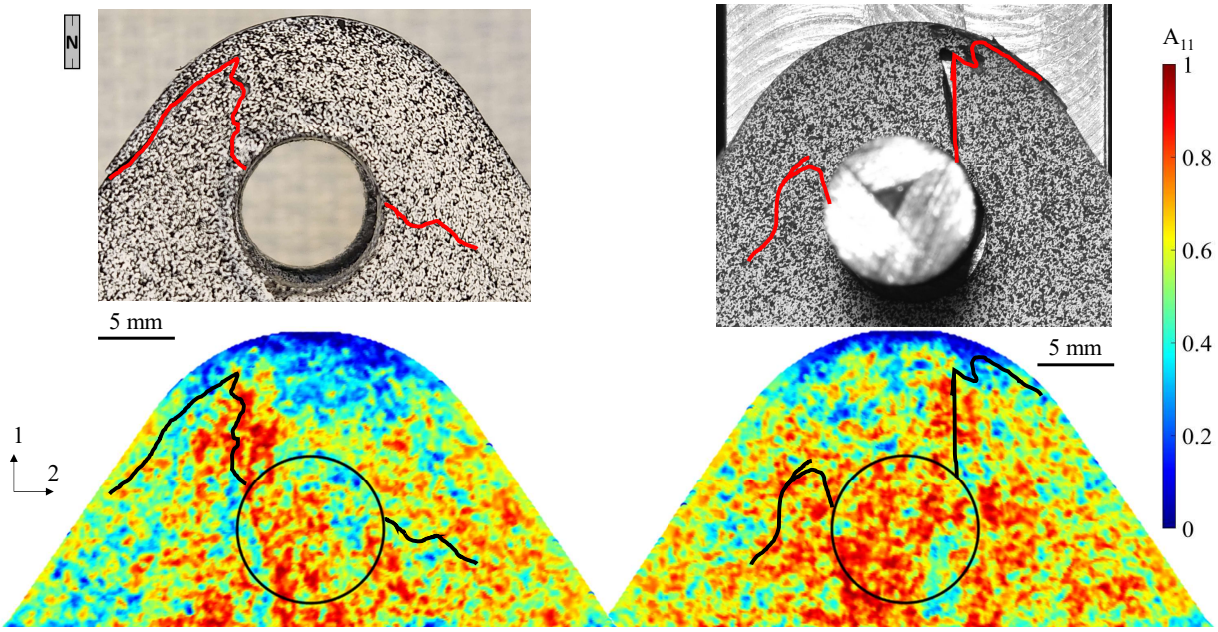

b) Narrow Platelet Tension Failure 2

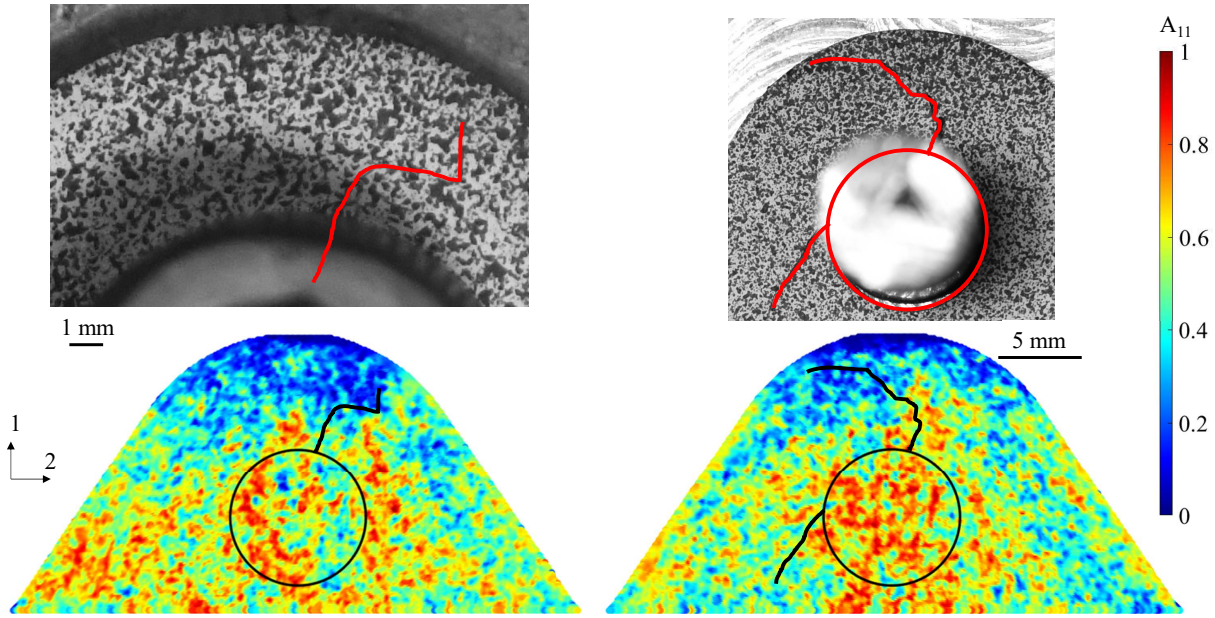

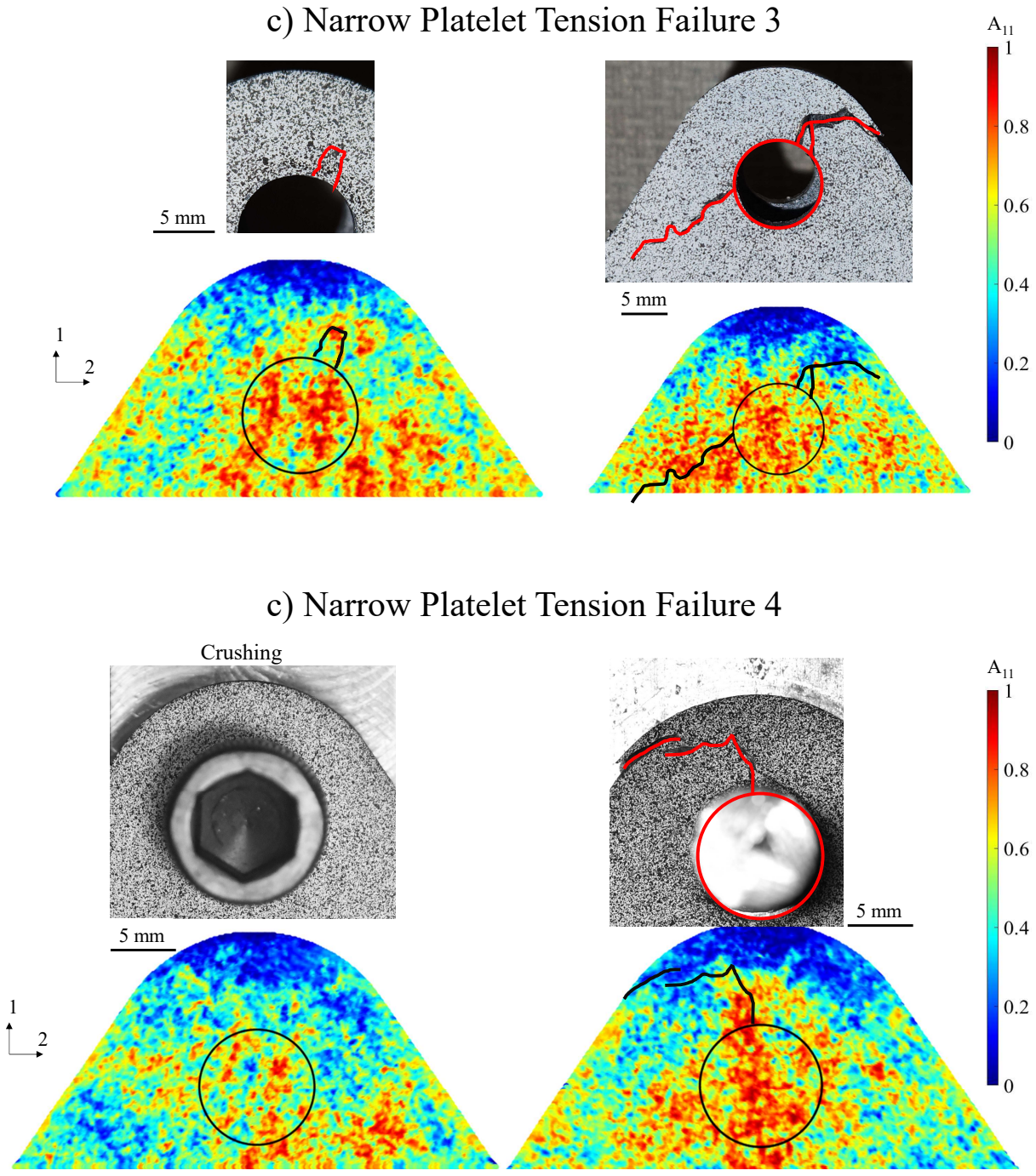

Figure A.2: Contour plots of narrow platelet Sekisui brackets of the orientation tensor component corresponding to the 1 direction with the fracture path in tension.

a) Square Platelet Tension Failure 1

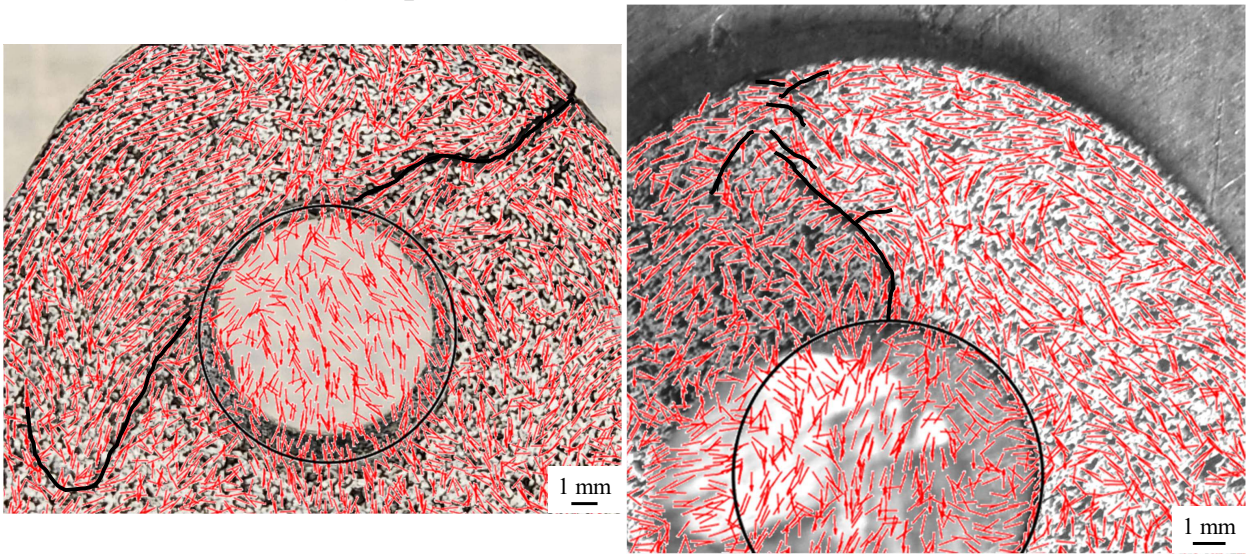

b) Square Platelet Tension Failure 2

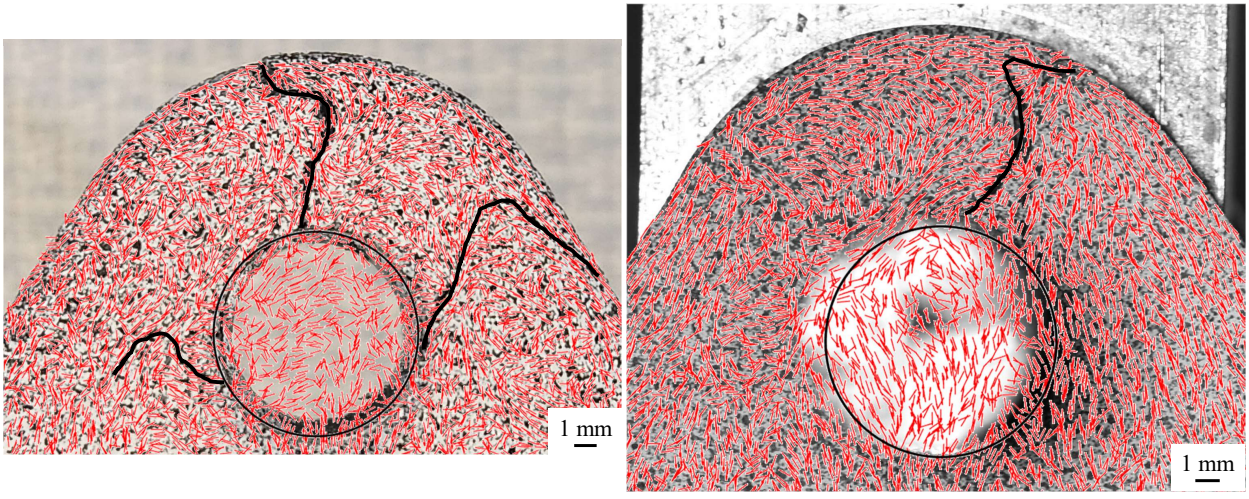

c) Square Platelet Tension Failure 3

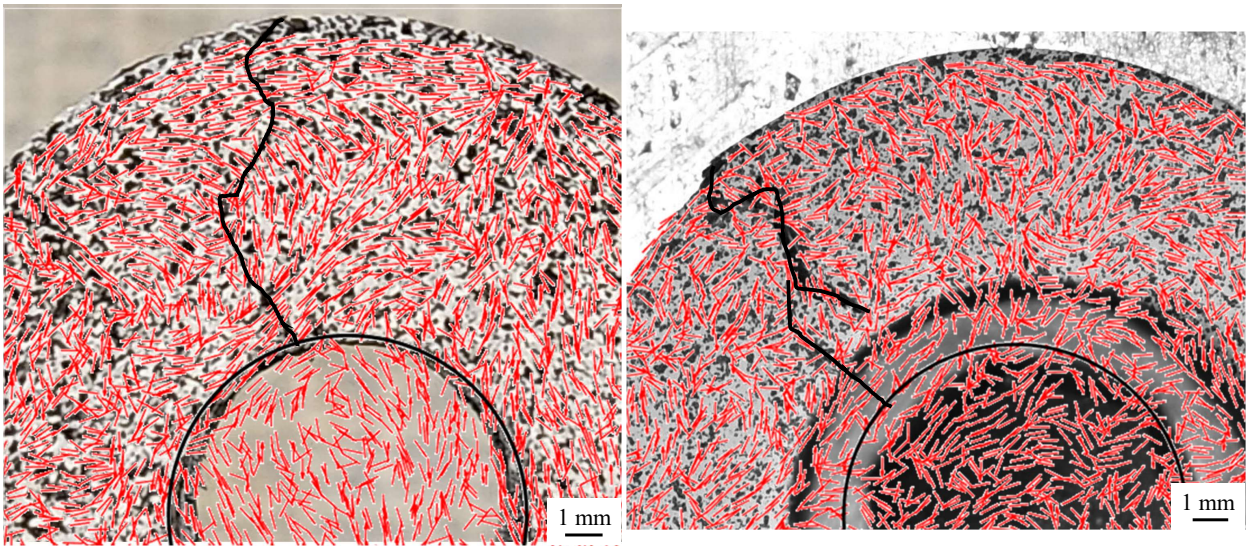

d) Square Platelet Tension Failure 4

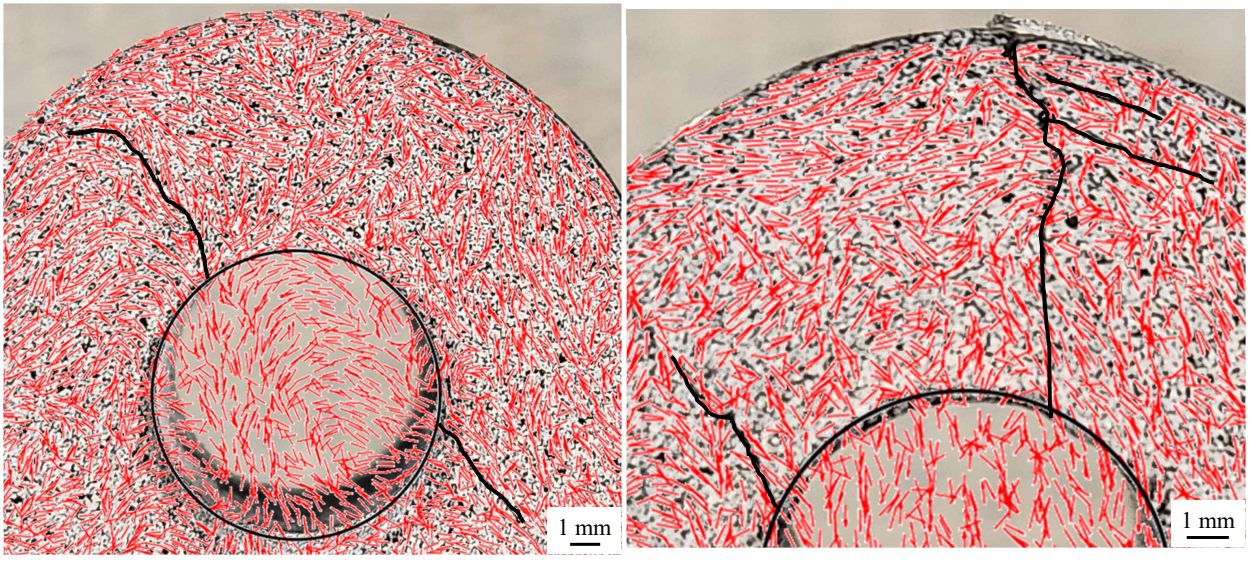

Figure A.3: Vector plots of square platelet Sekisui brackets of the orientation with the fracture path in tension.

a) Narrow Platelet Tension Failure 1

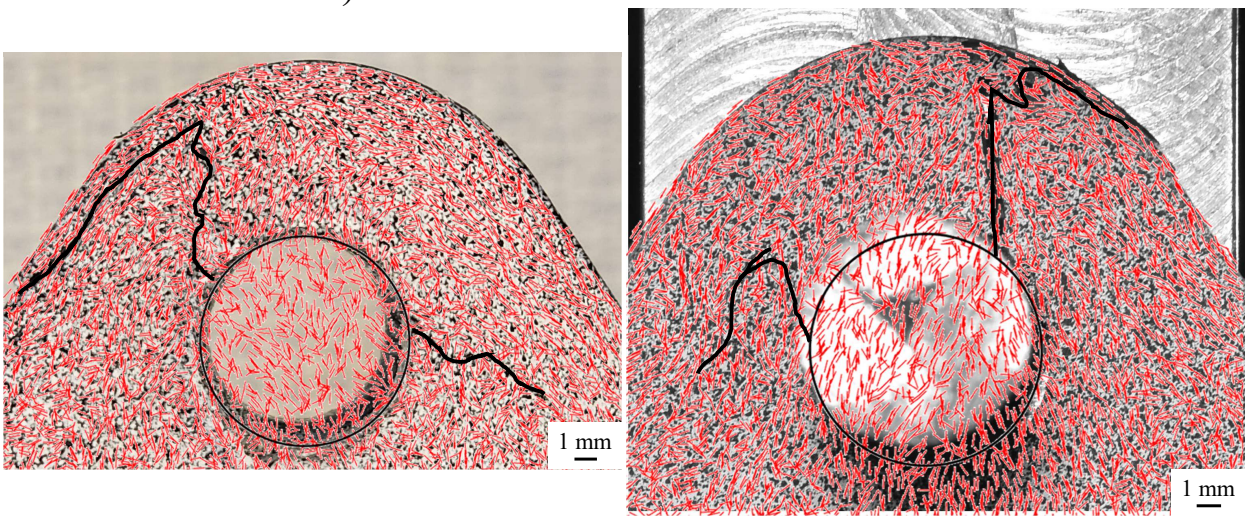

b) Narrow Platelet Tension Failure 2

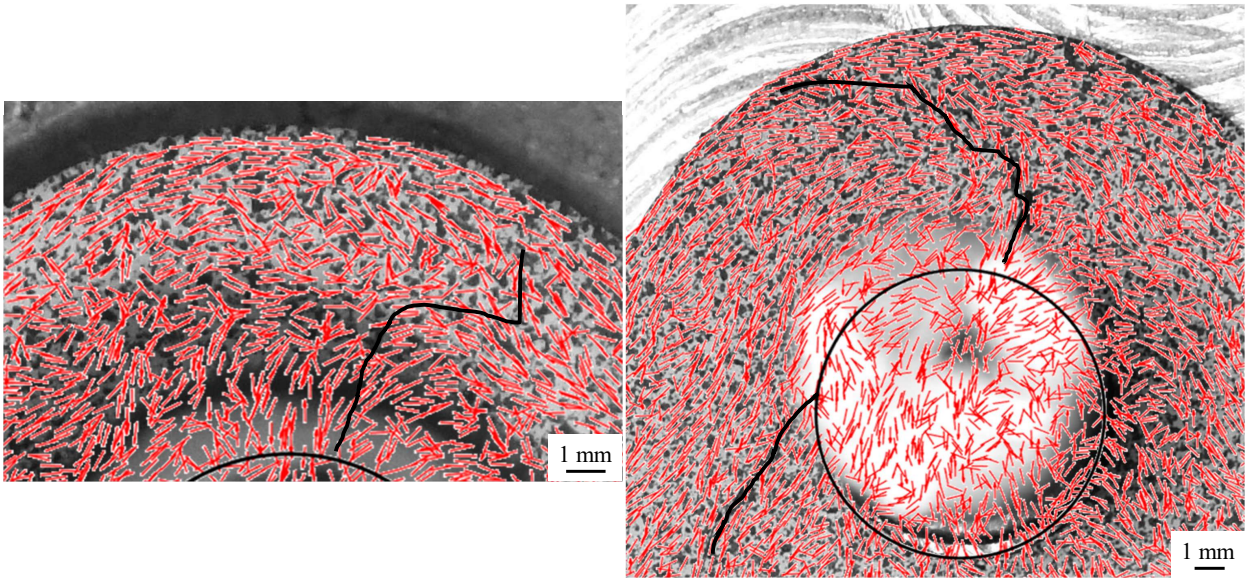

c) Narrow Platelet 3 Sekisui Failure

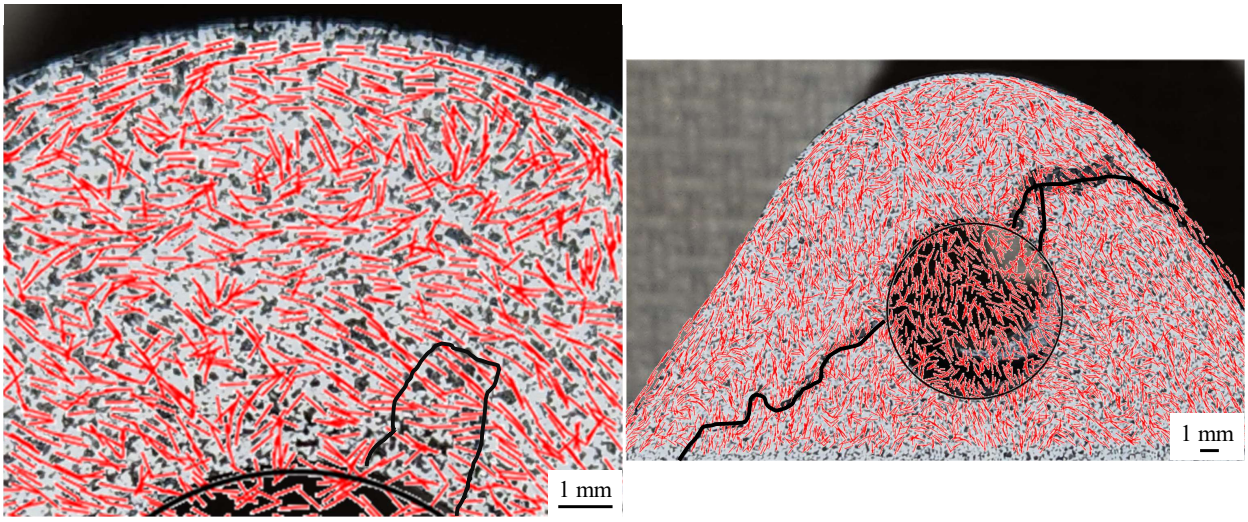

d) Narrow Platelet 4 Sekisui Failure

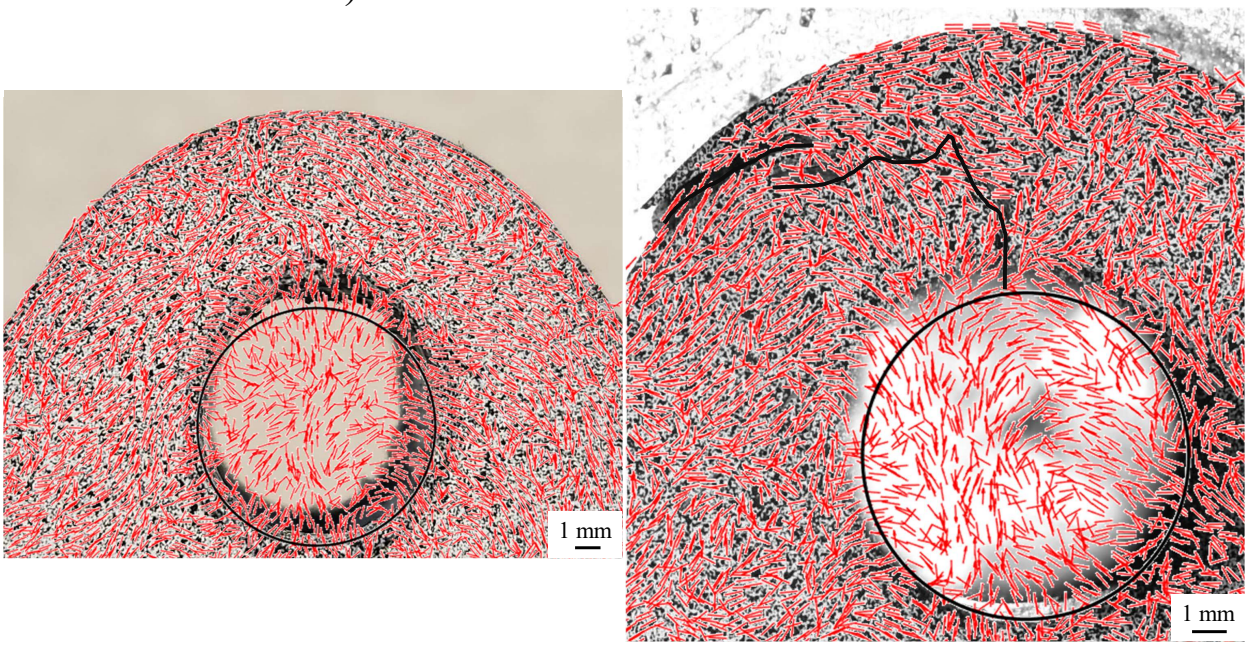

Figure A.4: Vector plots of narrow platelet Sekisui brackets of the orientation with the fracture path in tension.

a) Square Platelet Bending Failure 1a

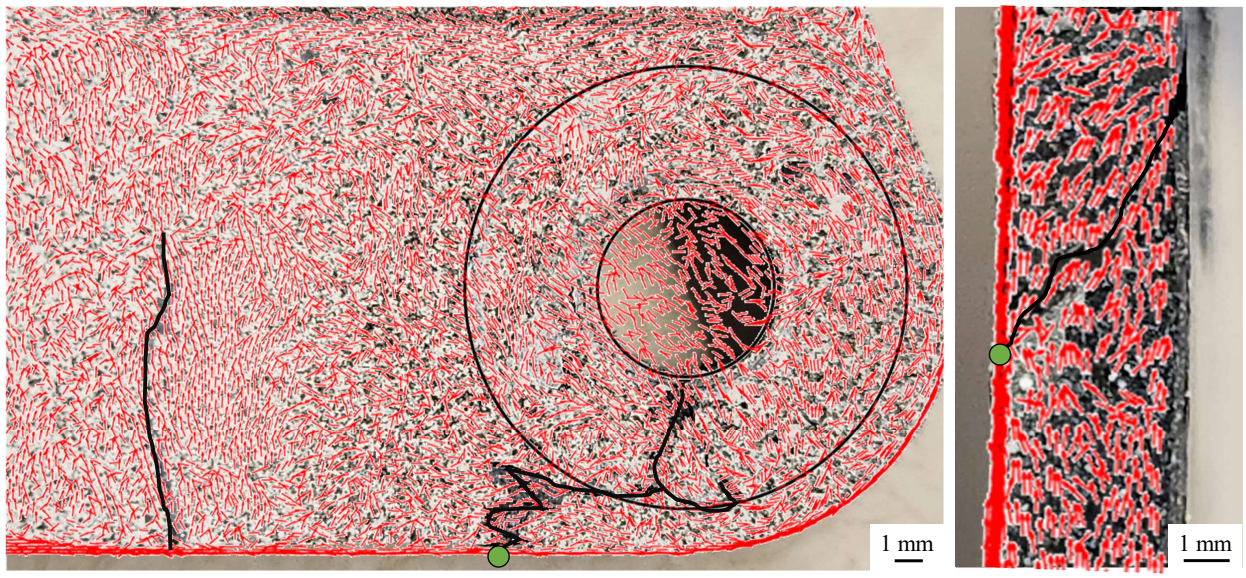

b) Square Platelet Sekisui Failure 1b

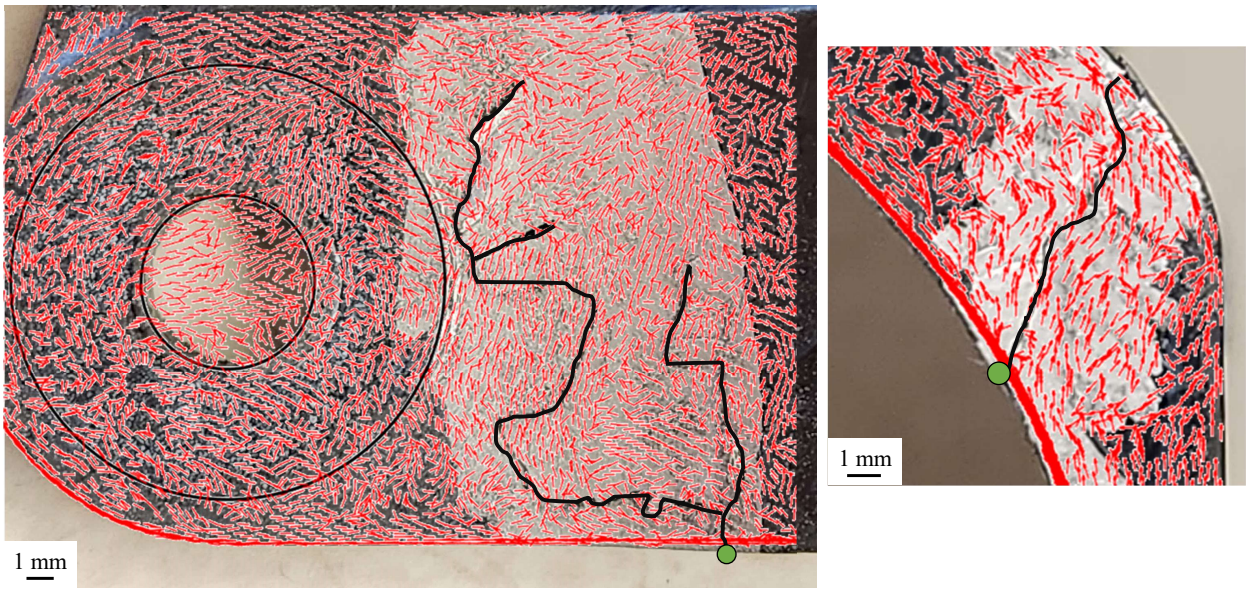

c) Square Platelet Sekisui Failure 2a

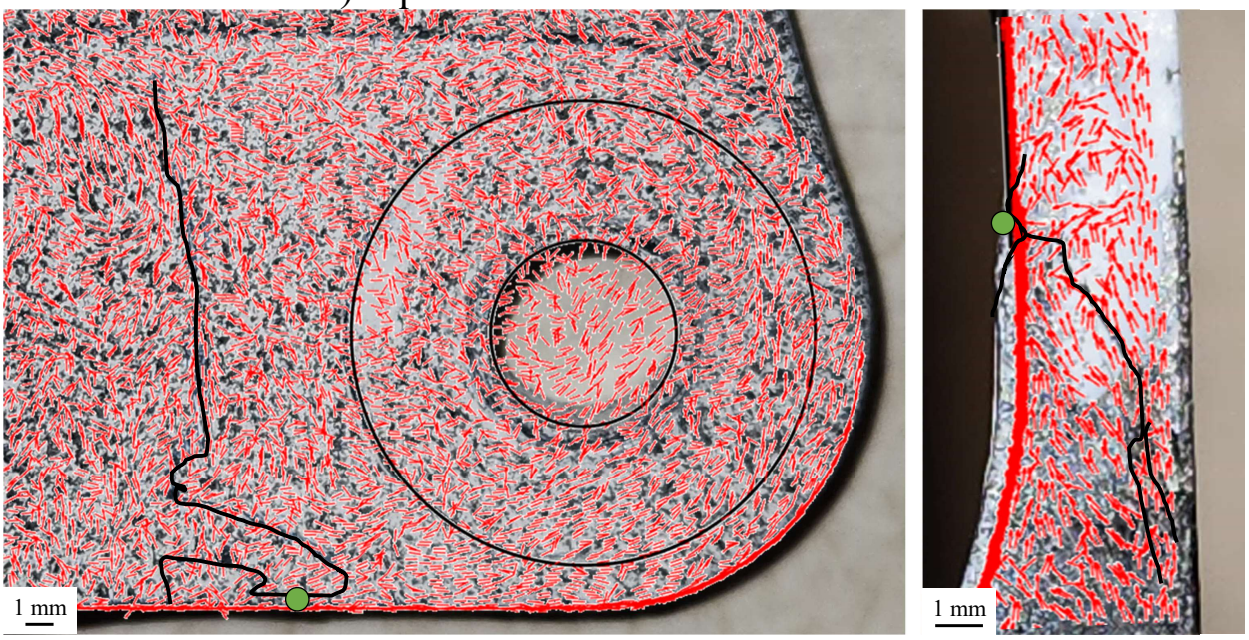

d) Square Platelet Sekisui Failure 2b

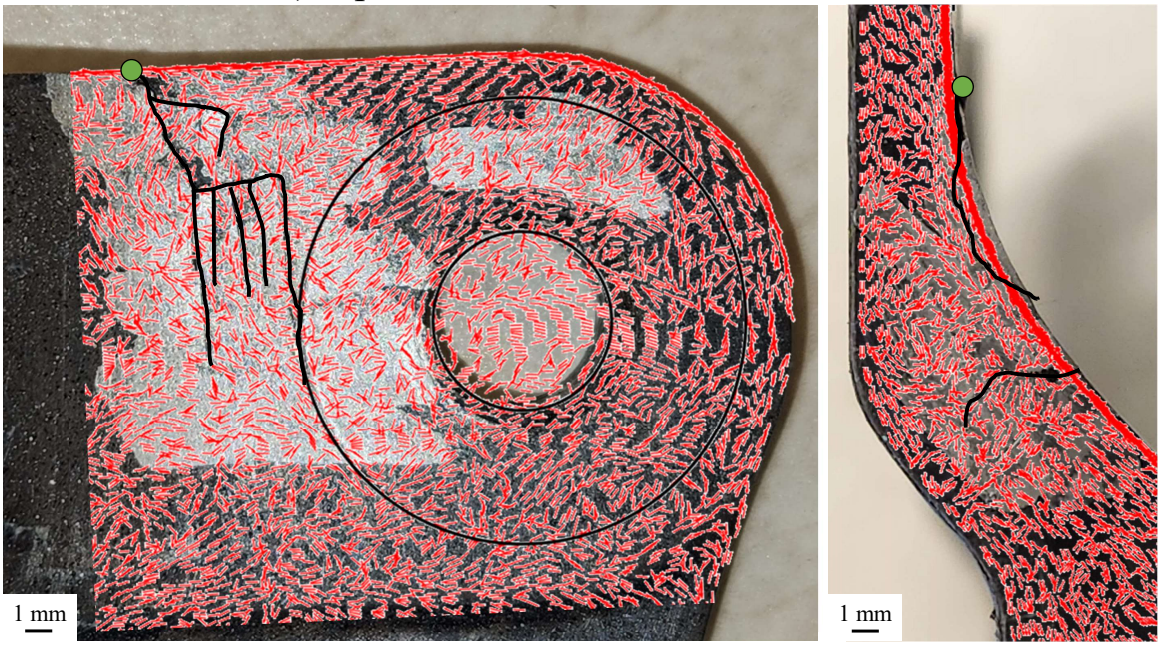

e) Square Platelet Sekisui Failure 3a

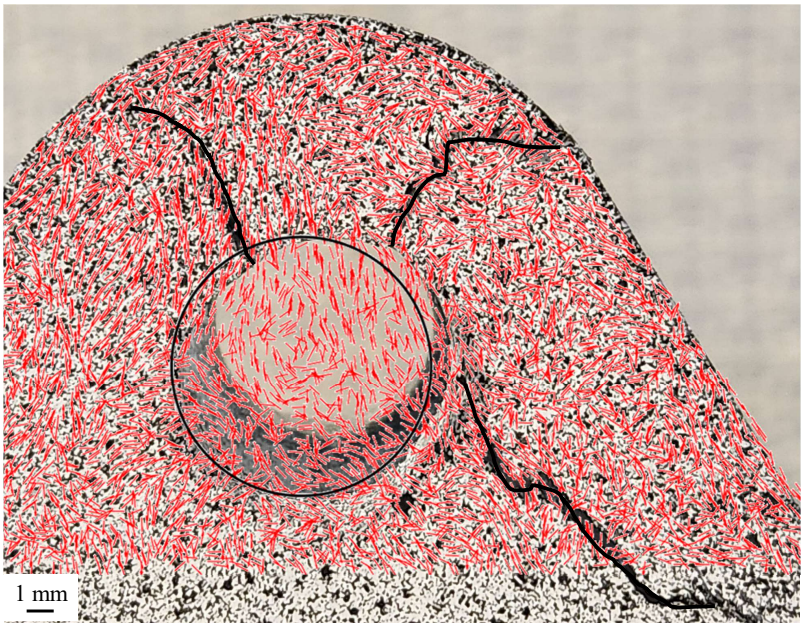

f) Square Platelet Sekisui Failure 3b

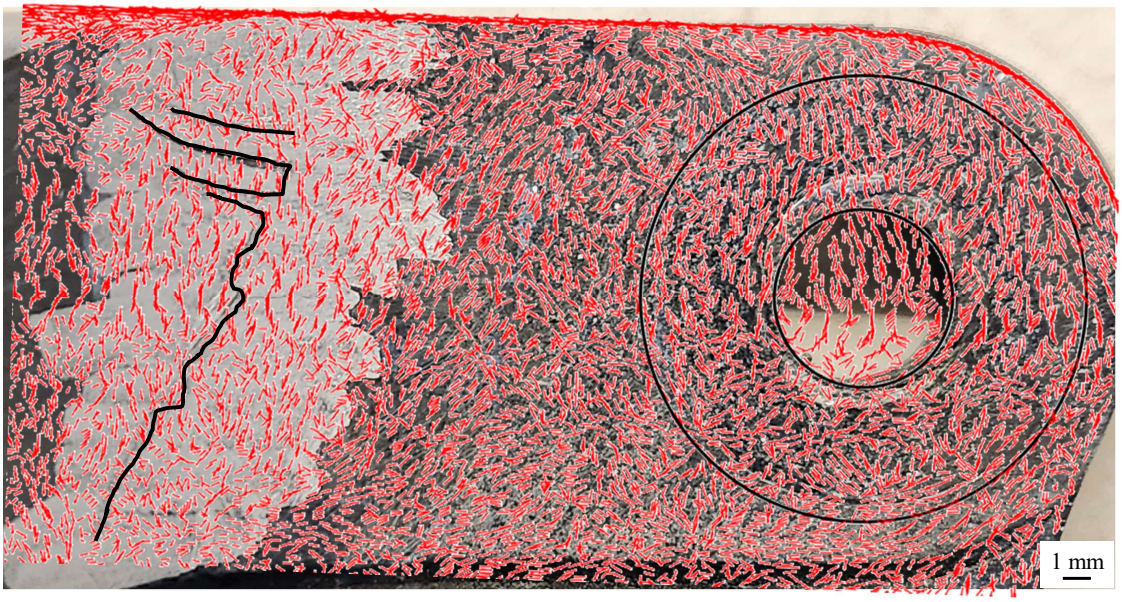

g) Square Platelet Sekisui Failure 4a

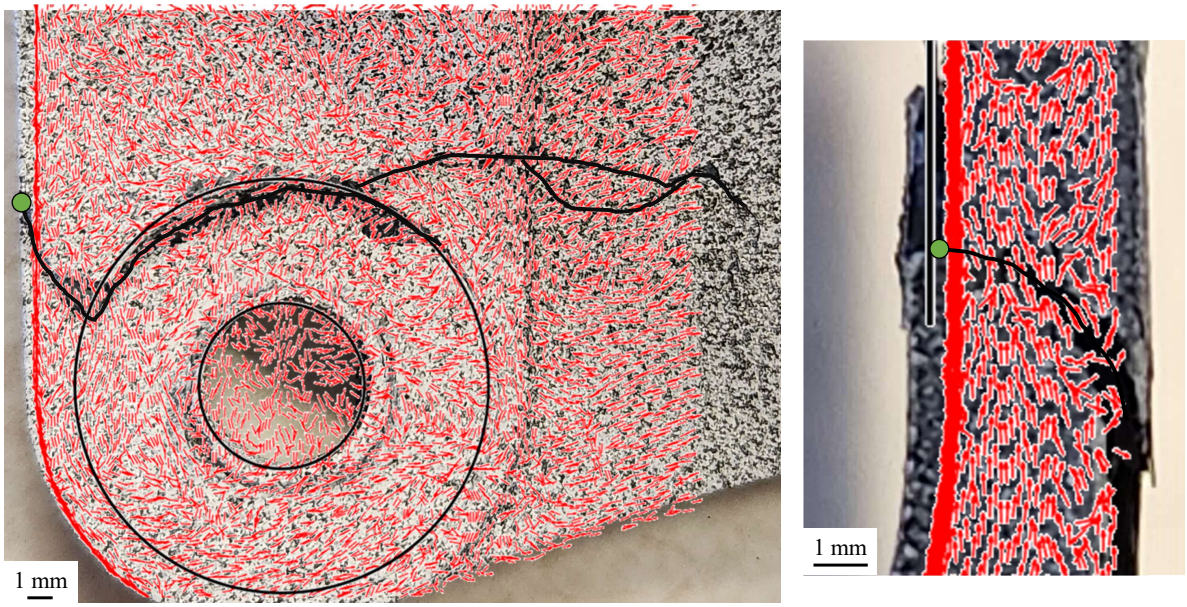

h) Square Platelet Sekisui Failure 4b

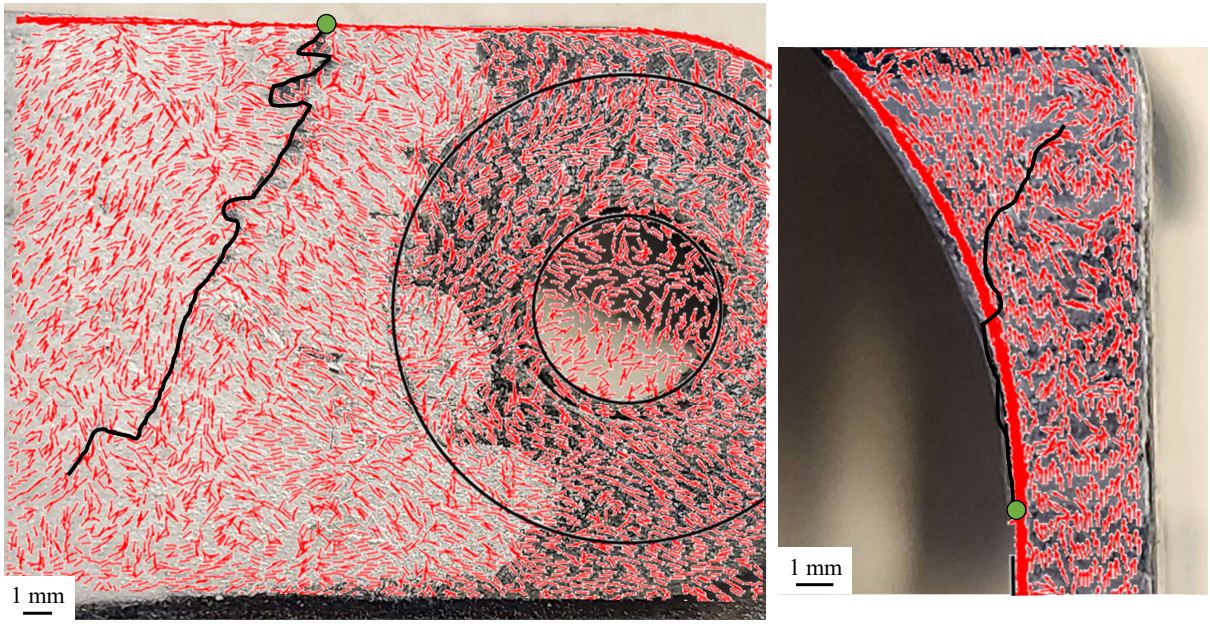

Figure A.5: Vector plots of square platelet Sekisui brackets of the orientation with the fracture path in bending.

a) Narrow Platelet Bending Failure 1a

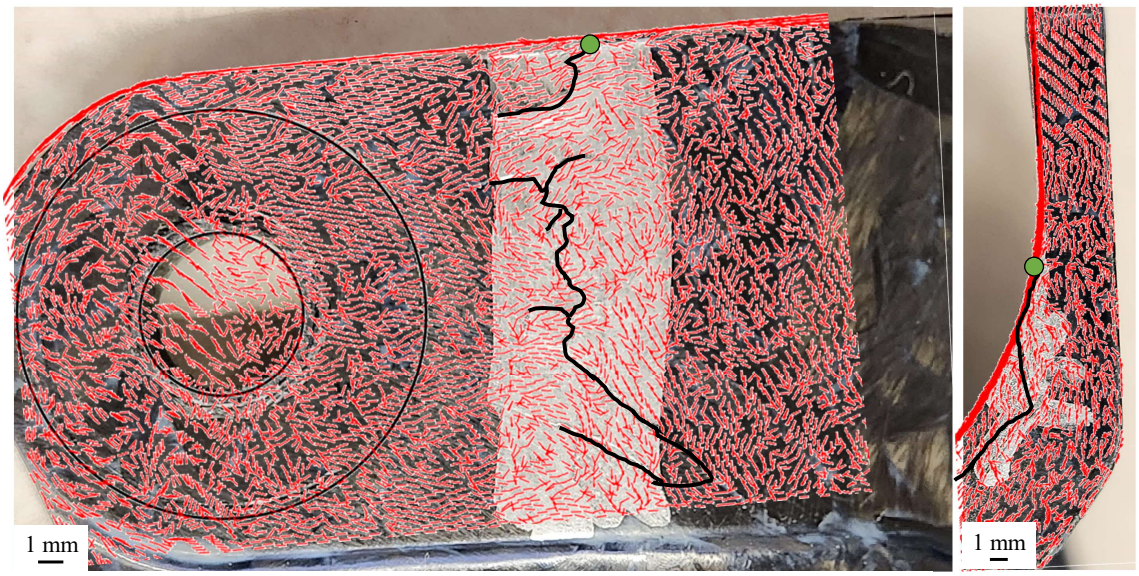

b) Narrow Platelet Bending Failure 1b

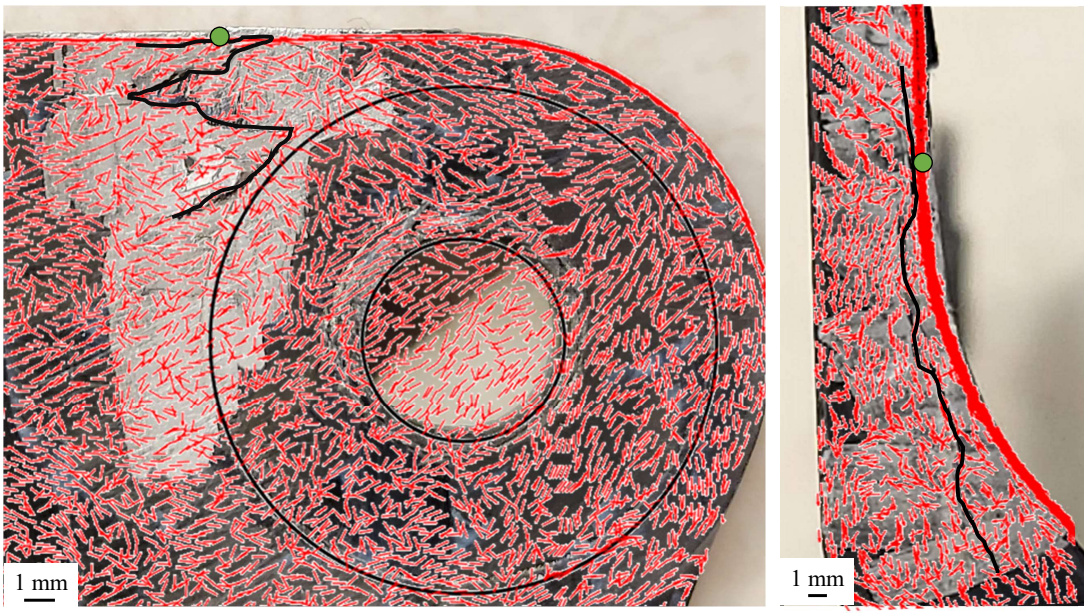

c) Narrow Platelet Bending Failure 2a

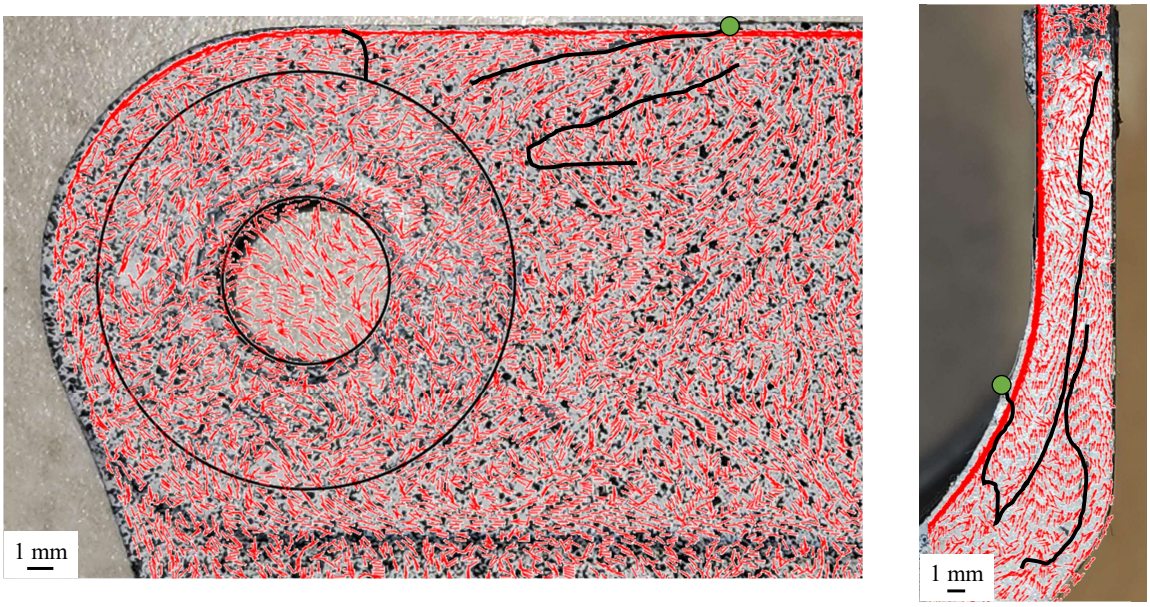

d) Narrow Platelet Bending Failure 2b

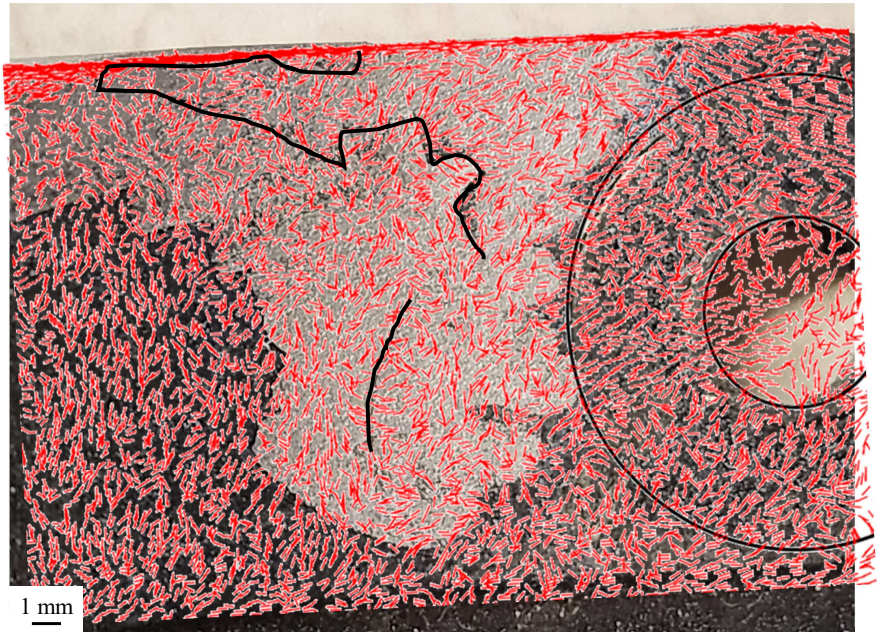

e) Narrow Platelet Bending Failure 3a

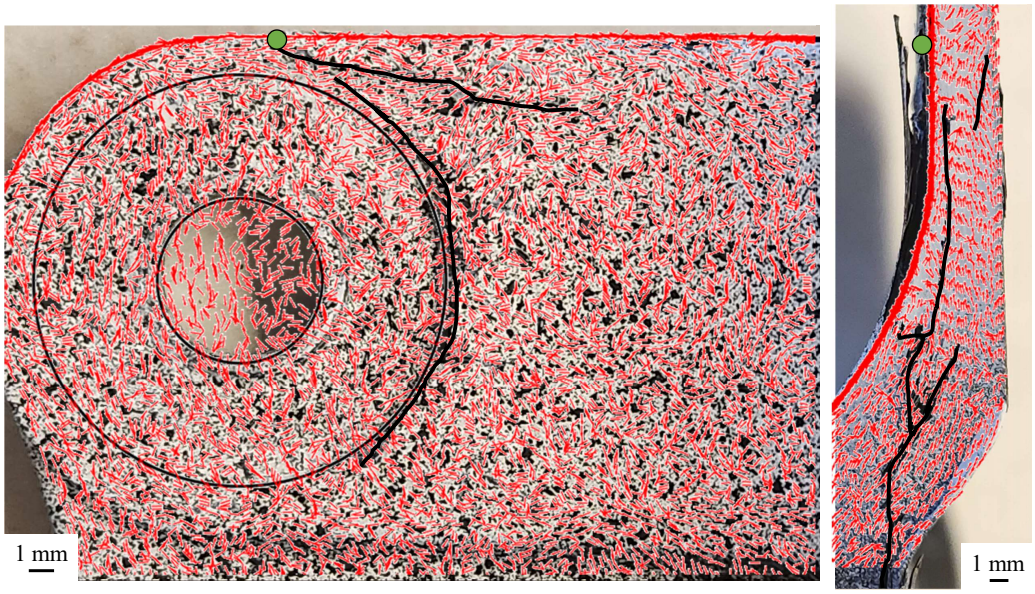

f) Narrow Platelet Bending Failure 3b

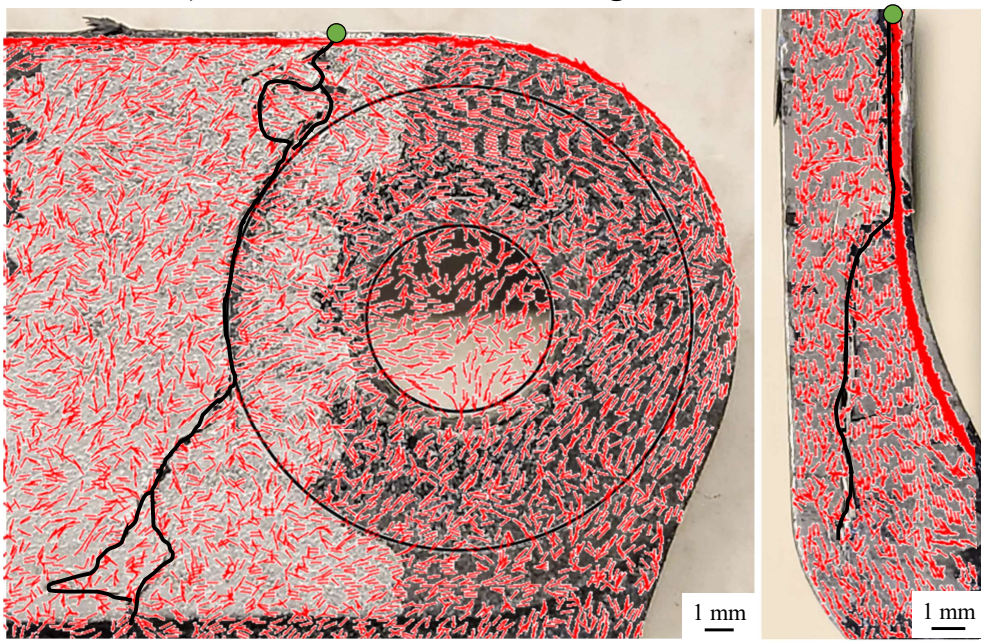

g) Narrow Platelet Bending Failure 4a

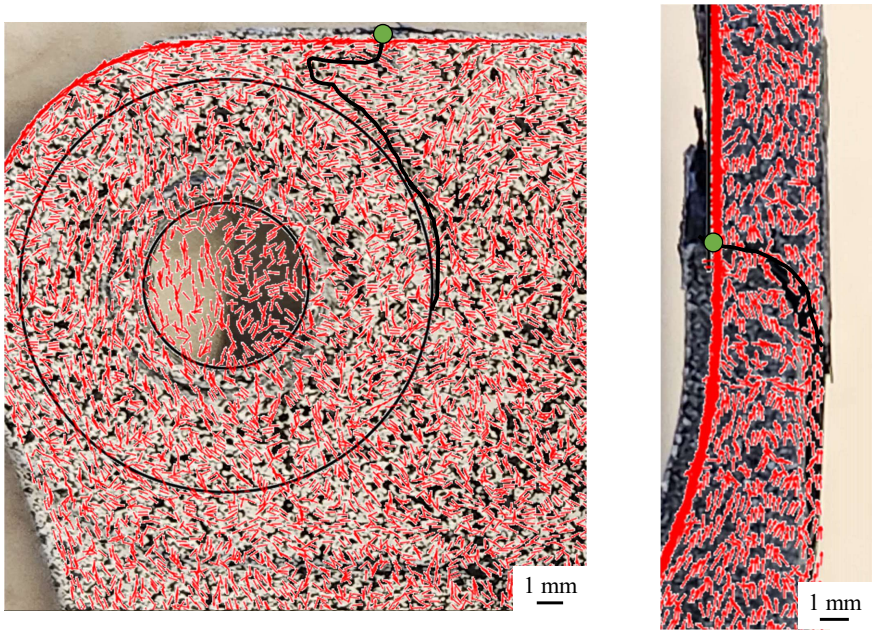

h) Narrow Platelet Bending Failure 4b

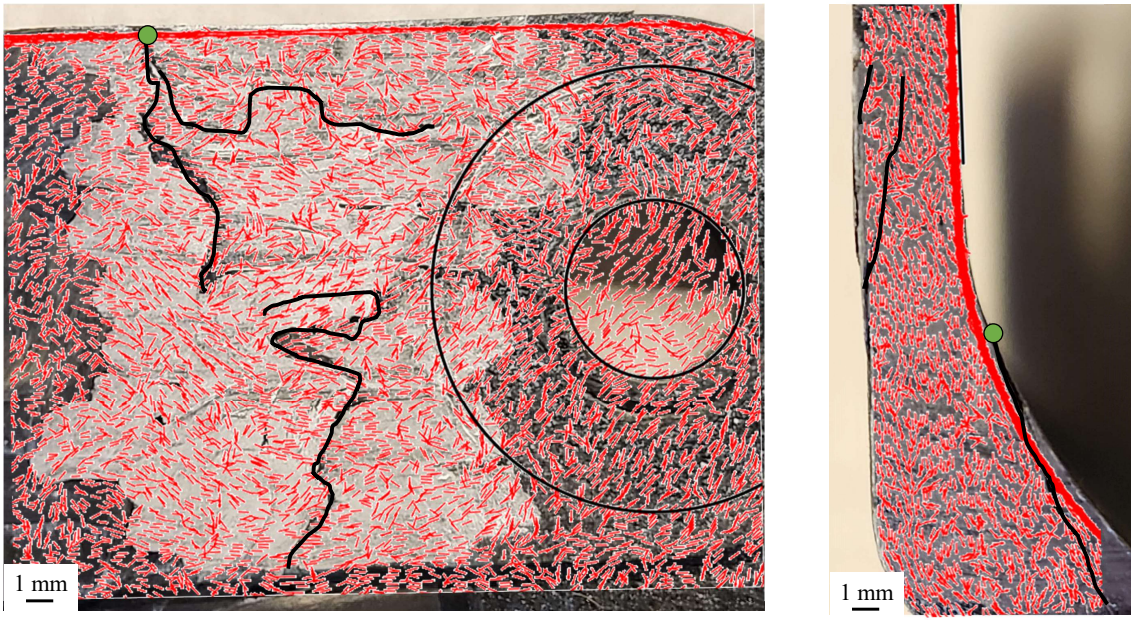

Figure A.6: Vector plots of narrow platelet Sekisui brackets of the orientation with the fracture path in bending.

VITA

Troy Nakagawa was born in Honolulu, Hawaii, USA. He earned his B.S. in Mechanical and Energy Engineering from the University of North Texas in 2018. Then he started his graduate studies in the Department of Aeronautics & Astronautics at the University of Washington. He joined the Laboratory for Multi-scale Analysis of Materials & Structures (MAMS) led by Professor Marco Salviato (chair) in the autumn of 2018. In spring 2020, he eared his M.S. degree in Aeronautics & Astronautics from the University of Washington. In summer 2023, he earned his Ph.D. degree in Aeronautics & Astronautics from the University of Washington.